DLR-IB-AT-KP-2018-145

Analysis of Spectral Non-Reflecting Boundary Conditions for Unsteady Simulations of Turbomachinery Flows in Terms of Prediction Quality and Computational Effort

Master Thesis

Pierre Sivel

Deutsches Zentrum
DLR für Luft- und Raumfahrt

Deutsches Zentrum für Luft- und Raumfahrt
German Aerospace Center
DLR
Institut für Strahlantriebe und Turbomaschinen
IST
RWTH AACHEN UNIVERSITY

Master Thesis

Analysis of Spectral Non-Reflecting Boundary Conditions for Unsteady Simulations of Turbomachinery Flows in Terms of Prediction Quality and Computational Effort

by Sivel, Pierre
Matr.-NR.: 323957

The present work was submitted to the
Institute of Jet Propulsion and Turbomachinery

Faculty of Mechanical Engineering of the
Rheinisch-Westfälischen Technische Hochschule Aachen

In collaboration with the
German Aerospace Center - Institute of Propulsion Technology

1st examiner:	Univ.-Prof. Dr.-Ing. Peter Jeschke
2nd examiner:	Dr.-Ing. Herwart Hönen
supervisor:	Dipl.-Ing. Stefan Henninger
external supervisor:	Daniel Schlüß, M.Sc.

Aachen, October 22, 2018

Abstract

The correct numerical representation of unsteady flow phenomena is becoming ever more important, for the design of increasingly performant turbomachines.
Mathematical representations of fluid dynamics require an appropriate definition of boundary conditions to resolve the governing differential equations. In the optimal case, the boundaries of the computational domain are positioned far away from the area of interest. Due to the compact architecture of turbomachines, the boundaries need to be positioned close to the blades. This leads to unsteady fluctuation being reflected from the boundaries. These reflections can severely deteriorate the solution.
In the flow solver TRACE, spectral boundary conditions have been implemented to prevent reflections. These non-reflecting boundary conditions take advantage of the fact that turbomachinery flows are dominated by periodic phenomena. At the boundaries, the flow field is decomposed into the spectral domain and incoming perturbations are suppressed. However, spectral boundary conditions are non-local in time and space. This results in high computational costs. One possibility to increase efficiency is to include only the relevant portion of the spectrum in the spectral boundary conditions with regards to the simulated configuration.
In this work, a concept for a reduced set of harmonics for the spectral non-reflecting boundary conditions is developed. Using Q3D simulations of 1.5 compressor stages, the analysis of unsteady fluctuations at each harmonic reveals that only harmonics of the blade passing frequencies of rows rotating with different rotational speeds than the boundaries produce relevant reflections. A setup including only these harmonics in the boundary conditions is simulated. The results show that spectral boundary conditions using a reduced set of harmonics yields very good results, at significantly lower computational costs.
The concept is applied to a steam turbine stage. The results validate that a correct reduction of the set of harmonics does not affect the prediction quality of the solution, but significantly reduces the computational costs of the spectral boundary conditions. Finally, a method is presented that allows for an a posteriori analysis of the quality of the set of harmonics.

Kurzfassung

Um das vorhandene Potential zur Verbesserung von Turbomaschinen zu erschließen, gewinnen instationäre numerische Simulationen zunehmend an Bedeutung.
Die mathematische Beschreibung von Strömungen verlangt eine geeignete Vorgabe von Randbedingungen für die zugrundeliegenden Differentialgleichungen. Im optimalen Fall befinden sich die Ränder des Rechengebiets in großem Abstand vom relevanten Bereich der Strömung. Bedingt durch möglichst kompakte Bauweisen von Turbomaschinen ergeben sich dagegen kleine Rechengebiete. Dadurch können sich Störungen bis zu den Rändern des Rechengebiets ausbreiten und an den künstlichen Rändern numerisch reflektiert werden. Infolgedessen kann das Simulationsergebnis stark beeinträchtigt werden.
Für den Strömungslöser TRACE wurden spektrale Randbedingungen entwickelt, die eben diese Reflektionen verhindern. Diese Randbedingungen nutzen die Eigenschaft aus, dass die Strömung in Turbomaschinen durch periodische Phänomene dominiert ist. Die Schwankungen des Strömungsfeldes werden am Rand des Rechengebiets spektral zerlegt und die einlaufenden Störungen werden unterdrückt.
Allerdings können spektrale Randbedingungen nicht lokal in Ort und Zeit formuliert werden. Dadurch ergeben sich besondere Herausforderungen bezüglich Rechenaufwand, Effizienz und Speicherbedarf. Um dem zu begegnen, wird angestrebt lediglich den für die jeweilige Simulation relevanten Teil des Spektrums in die spektralen Randbedingungen einzubeziehen.
In dieser Arbeit wird ein Konzept zur Definition eines reduzierten Sets von Harmonischen, für die spektralen nichtreflektierenden Randbedingungen, hergeleitet. Anhand von Q3D Simulationen von 1.5 Kompressorstufen, wird der instationäre Druck bei verschiedenen Harmonischen untersucht. Dies ergibt, dass lediglich Harmonische der Schaufeldurchgangsfrequenz von Reihen, deren Rotationsgeschwindigkeiten verschieden sind von der Rotationsgeschwindigkeit am Rand des Rechengebiets, relevante Reflektionen hervorrufen. Anschliessend, wird eine Simulation durchgefürht, bei der nur diese Harmonischen in den Randbedingungen einbezogen werden. Diese Simulation zeigt, dass ein reduziertes Set sehr gute Ergebnisse erzeugt, bei deutlich kleinerem Rechenaufwand.
Diese Ergebnisse werden auf eine Dampfturbinenstufe angewandt. Hier bestätigt sich, dass das reduzierte Set keine Beeinträchtigung der Ergebnisse hervorruft, aber den Rechenaufwand deutlich senkt. Abschließend, wird eine Methode vorgestellt, die eine a posteriori Analyse der Qualität des sets von Harmonischen ermöglicht.

Contents

List of Figures

List of Tables

Variables

Variable	Meaning	Unit
α	Weight of the right eigenvector	[-]
α_r	Flow angle in radial direction	°
α_θ	Flow angle in circumferential direction	°
γ	Ratio of specific heats	[-]
δ_{ij}	Kronecker delta	[-]
η	Dynamic viscosity	sPa
ϱ	Density	kg/m^3
τ_{ij}	Viscous stress tensor	Pa
ω	Angular frequency	1/s
Ω	Rotation speed	1/s
a	Speed of sound	m/s
c	Characteristic variables	[-]
δc	Characteristic update	[-]
c_p	Specific heat capacity at constant pressure	J/kgK
c_v	Specific heat capacity at constant volume	J/kgK
e	Inner specific energy	J/kg
E	Specific energy	J/kg
h	Specific enthalpy	J/kg
h_t	Total specific enthalpy	J/kg
I	Identity matrix	[-]
k	Axial wave number	1/m
k_T	Heat conductivity	W/mK
l	Left eigenvector	[-]
l	Circumferential wave number	1/m
L	Left eigenvector matrix	[-]
L_T	Eddy length scale	[-]
m	Non-dimensional circumferential wave number	[-]
Ma	Mach number	[-]
N_B	Number of simulated blade passages	[-]
N_p	Number of timesteps per period	[-]
p	Pressure	Pa
p_t	Total pressure	Pa
P_{in}	Projection matrix onto incoming characteristics	[-]
P_{out}	Projection matrix onto outgoing characteristics	[-]
q	Vector of primitive variables	[-]
q_j	Specific heat flux in j-direction	J/kg
δq	Primitive update	[-]
r	Right eigenvector	[-]
r	Radius	m
R	Right eigenvector matrix	[-]
R	Ideal gas constant	J/kgK
R_{rel}	Relative span	[-]
s_{ij}	Deformation tensor	1/s

s	Specific entropy	J/kgK
S	Sutherland constant	K
S_R	Volume forces source term in rotating systems	N/m^3
t	Time	s
T	Temperature	K
T_t	Total temperature	K
T_u	Turbulent intensity	[-]
u	Velocity in axial dierection	m/s
v	Velocity in pitchwise direction	m/s
w	Velocity in spanwise direction	m/s
x	Position in axial dierection	m
y	Position in pitchwise direction	m
z	Position in spanwise direction	m
$\Re$	Residual	[-]

Indices

Subscripts

bd	User defined boundary value
$target$	Target value
$\bar{x}$	Mean value of x
$\bar{x}$	Reynolds-average of x
x'	Fluctuations of x based on Reynolds-averaging
$\hat{x}$	Modal amplitude of x
$\tilde{x}$	Favre-average of x
x''	Fluctuations of x based on Favre-averaging

Superscripts

ϑ	Circumferential average
ω	Fourier decomposed in time
f	Face cell value
i	Inner cell value
in	Projection of incoming characteristics
l	Fourier decomposed circumferentially
out	Projection of outgoing characteristics
t	temporal average
0	Reference value
$1d$	One dimensional

Abbreviations

BPF_2	R_2 blade passing frequency
CFD	Computational Fluid Dynamics
DLR	German Aerospace Center (Deutsches Zentrum für Luft- und Raumfahrt)
GMC	General Mesh Connector
GPTL	General Purpose Timing Library
NRBC	Non-Reflecting Boundary Conditions
Q3D	Quasi-Three-Dimensional
R_2	Rotor 2
RANS	Reynolds-Averaged Navier-Stokes equations
S_1	Stator 1
S_2	Stator 2
TRACE	Turbomachinery Research Aerodynamics Computational Environment
URANS	Unsteady Reynolds-Averaged Navier-Stokes equations
VPF_1	S_1 vane passing frequency
VPF_2	S_2 vane passing frequency
1D	One-dimensional
2D	Two-dimensional

1 Introduction

1.1 Motivation

In the last decades, the strong increase in performance of computer hardware has led to computational fluid dynamics (CFD) becoming a firmly established instrument of the industrial research and design process. Flow simulations are used in a wide variety of fields, such as aerospace engineering, automotive engineering and energy. CFD represents a cost-efficient complement to experimental analysis and allows to analyze operating points which are difficult to reach experimentally [31].
Because of the major role of steady simulations in the geometrical optimization processes of turbomachines, they represent an important and widely used tool. Due to increasing demand for higher performance, turbomachines with increasingly loaded blades are needed. For the design of such turbomachines, a proper knowledge of unsteady phenomena is necessary. Therefore, the analysis of unsteady effects, like aeroelastics, aeroacoustics and unsteady blade row interactions, necessitates highly accurate unsteady flow simulations.
Internal flow simulations are performed on truncated computational domains. Here, the boundary conditions represent the effect of the flow outside of the domain and define the operating point. Therefore, the choice of correct boundary conditions has a strong impact on the quality of the solution. Due to the compact architecture of turbomachines, boundaries are often positioned very close to the blades. In unsteady simulations, the use of straightforward "far-field" boundary conditions leads to reflections of outgoing unsteady perturbations which impairs the quality of the solution.
An efficient method to simulate flows dominated by periodic unsteady effects is to use a frequency domain solver, like the Harmonic Balance method [13]. Here, the Fourier decomposed RANS equations are solved for specific sets of frequencies. The flow at the boundaries is decomposed into waves with distinct directions of propagation. This allows for a relatively simple non-reflecting treatment at the boundaries.
When performing unsteady time domain simulations, the implementation of non-reflecting boundary conditions (NRBC) becomes more challenging [19]. Still, frequency domain simulations have disadvantages, which cause time domain simulations to still be essential. Firstly, for the application of a frequency domain solver, perturbations in the flow must be entirely periodic and their frequencies must be known. So, it is challenging for frequency domain solvers to correctly represent phenomena like shock boundary layer interactions, vortex shedding and unsteady wakes. Further, robust implementations of advanced turbulence models and transition models are still a matter of research [1]. Therefore, non-linear time domain methods still represent the most accurate method for simulations of unsteady phenomena and can be used to generate references to verify frequency domain solutions. Most time domain solvers utilize different boundary conditions than the frequency domain solvers. This complicates the comparison of results. It is, therefore, of great interest to include efficient spectral non-reflecting boundary conditions for time domain solvers.

1.2 Previous Work

Giles [10] presented a unified theory for the construction of NRBC for two-dimensional steady and unsteady flow simulations, based on the Fourier decomposition of the flow field at the boundary and an eigenvalue problem based on the linearized Euler equations. The mathematical theories behind the construction of NRBC were based on the publications of Kreiss [20], who analyzed the well-posedness of initial boundary value problems for hyperbolic systems, and the work of Higdon [15] who gave Kreiss' theories a physical interpretation in terms of wave propagation. For unsteady flow simulations, Giles described NRBC based on one-dimensional characteristics, but these boundary conditions showed insufficient non-reflecting behavior for fluctuations not impinging perpendicularly on the boundary.
To circumvent the fact that spectral NRBC were not local in time and space, Giles proposed two-dimensional approximated NRBC. These boundary conditions were based on the work of Engquist and Majda [7]. Giles used a second order Taylor expansion for the eigenvalue problem which yielded a set of partial differential equations. These equations could then be solved in the time domain. This method was shown not to be well-posed. Therefore, the optimal non-reflecting behavior in the context of the approximation was given up to achieve well-posedness. Later, Hagstrom [12] introduced higher order formulations of these NRBC which where local in time and non-local in space. Therefore, they could not be used for single passage simulations. Henninger et al. [14] showed that these higher order formulations yielded less spurious reflection than Giles' original approximate NRBC for waves with high incidence to the boundary.
Saxer and Giles [26] expanded the NRBC presented by Giles to three-dimensional flows, by neglecting fluctuations in radial direction.
An implementation of exact spectral NRBC was proposed by Chassaing and Gerolymos [5] for time domain solvers. The good reflection properties of these boundary conditions were shown on a basic test case, but it was also shown that the convergence was slow.
Schlüß et al. [28] implemented a time domain adaptation of the spectral NRBC used in frequency domain solvers, which was suitable for steady as well as unsteady simulations and did not suffer from accuracy losses due to the Taylor expansion of the eigenvalue problem used in approximate NRBC. Here again, the NRBC proved to have good reflection properties. The spectral NRBC were reimplemented in the solver TRACE by Schlüß and Frey [27], with regard to time domain specific aspects. This yielded better robustness and convergence.
Although this time domain adaptation of the frequency domain NRBC showed less reflections compared to other NRBC and allowed for consistent and comparable results in both domains, the necessity for the Fourier decompositions in space and time caused these NRBC to have a significantly higher computational cost than previously presented NRBC. This can limit the range of practical applications of this method. To achieve the highest accuracy possible, in the spectral domain, all modes of the Fourier decomposed flow solution must be considered in the application of these boundary conditions. It is assumed that modes with high frequencies may have negligible effects on the reflection behavior of the boundary. That is the reason why, the current work focuses on improving the efficiency of spectral NRBC by reducing the number of harmonics included in the NRBC, while maintaining a good solution quality.

1.3 Description of the Work

In chapter 2, the governing equations of fluid dynamics are presented, with particular focus on the equations solved in the test cases presented in the current work.
Chapter 3 focuses on the NRBC utilized in the current work. First, in section 3.1, the general approach of spectral NRBC presented by Schlüß et al. [28] is described. Then, in section 3.2, their implementation in TRACE is illustrated. In section 3.3, the concepts of 1D unsteady NRBC, approximate NRBC and 2D steady NRBC are described briefly.
A research compressor of the German Aerospace Center, Rig250, is simulated as a 1.5 stage Q3D-case in chapter 4. In this chapter, the main analysis of the boundary conditions is performed and a concept for the definition of sets of harmonics that need to be included in the NRBC is developed. In section 4.1, the computational setup is explained, including the generation of a Q3D-mesh and the numerical methods used for the simulation. The problem of slow convergence when using spectral NRBC is addressed briefly in section 4.3. In section 4.4, the main analysis of the set of harmonics for the NRBC is performed. In a first step, fundamental frequencies are defined and the set of harmonics in the boundaries is reduced in discrete steps. The quality of the solution is assessed for each step. Then, the behavior of unsteady fluctuations at individual harmonics is examined. Lastly, a final set of harmonics is defined, applied and compared with setups utilizing other NRBC.
To conclude this work, the results of the analysis of Rig250 are validated in chapter 5, by simulating the Durham Steam Turbine [22, 6] as a large three dimensional test case. In section 5.2, sets of harmonics are defined for the boundaries following the concept derived from chapter 4. The resulting solution is again compared with other NRBC. In section 5.3, a cost efficient method is introduced to verify if a sufficient number of harmonics has been considered in the NRBC.

2 Governing Equations

The fundamental equations of fluid dynamics are the Navier-Stokes equations. They are based on the principles of mass conservation (2.1), momentum conservation (2.2) and energy conservation (2.3). They describe the motion of compressible viscous fluids in a continuum flow. Using the Einstein summation convention, the conservative form of the Navier-Stokes equations reads

$$\frac{\partial \varrho}{\partial t} + \frac{\partial}{\partial x_i}\left(\varrho u_i\right) = 0 \tag{2.1}$$

$$\frac{\partial}{\partial t}\left(\varrho u_i\right) + \frac{\partial}{\partial x_j}\left(\varrho u_i u_j\right) = -\frac{\partial p}{\partial x_i} + \frac{\partial \tau_{ij}}{\partial x_j} \tag{2.2}$$

$$\frac{\partial}{\partial t}\left(\varrho E\right) + \frac{\partial}{\partial x_j}\left(\varrho u_j E\right) = -\frac{\partial u_j p}{\partial x_j} + \frac{\partial}{\partial x_j}\left(u_i \tau_{ij}\right) - \frac{\partial q_j}{\partial x_j}. \tag{2.3}$$

Here, t is the time, x is the position vector, u is the velocity vector and $(\varrho, \varrho u, \varrho v, \varrho w, \varrho E)^T$ is the vector of conservative variables, with ϱ being the density and E being the total energy per mass unit.
The heat flux in x_j-direction is represented by

$$q_j = -k_T \frac{\partial T}{\partial x_j}, \tag{2.4}$$

where T is the temperature and k_T is the heat conductivity. The viscous stresses are described by

$$\tau_{ij} = 2\eta\left(s_{ij} - \frac{1}{3} s_{kk}\delta_{ij}\right), \tag{2.5}$$

with δ_{ij} being the Kronecker delta and

$$s_{ij} = \frac{1}{2}\left(\frac{\partial u_i}{\partial x_j} + \frac{\partial u_j}{\partial x_i}\right) \tag{2.6}$$

being the deformation tensor.
To calculate the dynamic viscosity η, Sutherland's law for calorically perfect gases [30] is used.

$$\eta = \eta_0 \frac{T_0 + S}{T + S}\left(\frac{T}{T_0}\right)^{3/2}. \tag{2.7}$$

Here, T_0 is the reference temperature, η_0 is the reference dynamic viscosity at T_0 and S is the Sutherland constant of the fluid.
For a three-dimensional problem, the Navier-Stokes equations yield a set of five equations with seven independent variables. So, two further equations are needed, to close the problem. For a perfect gas the first equation is

$$e = c_v T, \tag{2.8}$$

where c_v is the specific heat capacity at constant volume and e is the inner energy per mass unit. The inner energy per mass unit e is related to the total energy per mass unit by the definition

$$E = e + \frac{1}{2} u_i u_i. \tag{2.9}$$

as second equation the equation of state for an ideal gas is used

$$p = \varrho R T, \tag{2.10}$$

with R as the ideal gas constant.
If the Navier-Stokes equations are solved in a system, rotating with the rotational speed Ω and where x is the axis of rotation, the source term

$$S_R = \begin{pmatrix} 0 \\ 0 \\ \varrho\Omega\left(y\Omega + 2w\right) \\ \varrho\Omega\left(z\Omega + 2v\right) \\ 0 \end{pmatrix} \tag{2.11}$$

is added to the right hand side of the equations, to take into account the centrifugal force and the Coriolis force.

In most turbomachinery applications, the flow is partially or fully turbulent. Resolving all length scales in a turbulent flow simulation requires a very fine spatial and temporal resolution. This leads to very high computational costs which are not suitable for industrial applications. One approach to this problem is to use the Reynolds Averaged Navier-Stokes equations (RANS). In this context, turbulence is not resolved. Instead, its influence on the temporally averaged flow is modeled statistically. The unsteady RANS equations (URANS) are derived by Reynolds-averaging the density and the pressure, and Favre-averaging the velocity, the energy and the temperature. This leads to the equations

$$\frac{\partial \bar{\varrho}}{\partial t} + \frac{\partial}{\partial x_i}\left(\bar{\varrho}\tilde{u}_i\right) = 0 \tag{2.12}$$

$$\frac{\partial}{\partial t}\left(\overline{\varrho}\tilde{u}_i\right) + \frac{\partial}{\partial x_j}\left(\overline{\varrho}\tilde{u}_i\tilde{u}_j\right) = -\frac{\partial \overline{p}}{\partial x_i} + \frac{\partial}{\partial x_j}(\overline{\tau}_{ij} - \overline{\varrho u_i'' u_j''}) \tag{2.13}$$

$$\begin{aligned} &\frac{\partial}{\partial t}\left[\overline{\varrho}\left(\tilde{e} + \frac{\tilde{u}_i\tilde{u}_i}{2}\right) + \frac{\overline{\varrho u_i'' u_i''}}{2}\right] + \frac{\partial}{\partial x_j}\left[\overline{\varrho}\tilde{u}_j\left(\tilde{h} + \frac{\tilde{u}_i\tilde{u}_i}{2}\right) + \tilde{u}_j\frac{\overline{\varrho u_i'' u_j''}}{2}\right] = \\ &\frac{\partial}{\partial x_j}\left[-\tilde{q}_j - \overline{\varrho u_j'' h''} + \overline{\tau_{ij}'' u_i''} - \frac{1}{2}\overline{\varrho u_j'' u_i'' u_i''}\right] + \frac{\partial}{\partial x_j}\left[\tilde{u}_i\left(\overline{\tau_{ij}} - \overline{\varrho u_j'' u_i''}\right)\right] \end{aligned} \tag{2.14}$$

with

$$h = e + \frac{p}{\varrho} = c_p T. \tag{2.15}$$

Here, c_p is the specific heat capacity at constant pressure. Variables denoted by a tilde are Favre-averaged, variables denoted by a bar are Reynolds-averaged and variables denoted by a double apostrophe are fluctuations around the Favre average.

Due to non-linearities in the Navier-Stokes equations, the URANS equations contain several additional components. The term $-\overline{\varrho u_i'' u_j''}$ is the Reynolds stress tensor, $\overline{\varrho u_j'' h''}$ is the turbulent heat flow, $\overline{\tau_{ij}'' u_i''}$ represents the molecular diffusion and $\frac{1}{2}\overline{\varrho u_j'' u_i'' u_i''}$ describes the transport of turbulent kinetic energy. These new elements introduce new independent variables into the equations. Therefore, the URANS equations need to be closed using an additional turbulence model.

In the simulations performed in this work, the flow inside the domain is computed, by numerically solving the URANS equations, but the approach for the non-reflecting boundary conditions presented in section 3.1 is based on the Euler equations. These are obtained by neglecting all viscous stresses and heat fluxes in the Navier-stokes equations, which leads to the unsteady, compressible and conservative form of the Euler equations

$$\frac{\partial \varrho}{\partial t} + \frac{\partial}{\partial x_i}\left(\varrho u_i\right) = 0 \tag{2.16}$$

$$\frac{\partial}{\partial t}\left(\varrho u_i\right) + \frac{\partial}{\partial x_j}\left(\varrho u_i u_j\right) + \frac{\partial p}{\partial x_i} = 0 \tag{2.17}$$

$$\frac{\partial}{\partial t}\left(\varrho E\right) + \frac{\partial}{\partial x_j}\left(\varrho u_j E\right) + \frac{\partial p u_i}{\partial x_j} = 0. \tag{2.18}$$

3 Non-Reflecting Boundary Conditions

In CFD, the correct choice of boundary conditions has a major impact on the quality of the solution [10]. The compact architecture of turbomachines means that, in numerical representations of the machines, boundaries and interfaces must be positioned very close to the domain of interest. If straightforward far-field boundary conditions are used, it leads to artificial reflections of outgoing waves which can strongly deteriorate the quality of the solution [26].
One answer to this problem is to use non-reflecting boundary conditions (NRBC). The concept behind these boundary conditions is to take advantage of the periodic character of perturbations in turbomachines, to transform the flow at the boundaries into the spectral domain. Perturbations are split into incoming and outgoing waves and incoming perturbations are suppressed, thereby preventing spurious reflections.
In section 3.1, the general approach to NRBC is presented. The content in this section is strongly based on the work of Giles [9, 10] and Saxer et al. [26]. Section 3.2 describes the implementation of spectral NRBC in TRACE which is based on the implementation presented by Schlüß et al. [28, 27]. The results produced using spectral NRBC are compared with results computed using other commonly employed NRBC. In section section 3.3, the concepts behind these NRBC are presented shortly.

3.1 General Approach

Starting point for the construction of NRBC are the Euler equations (2.16), (2.17) and (2.18). In typical axial flow turbomachines, radial variations in the flow are significantly smaller than circumferential variations [26]. Therefore, Saxer and Giles [26] proposed quasi-three-dimensional NRBC that only consider radial variations in the turbomachine in the average mode, by neglecting all radial perturbations in the flow. Further, it is assumed that only sufficiently small perturbations around the mean flow are considered, thus the Euler equations can be linearized. The three-dimensional linearized Euler equations, neglecting radial changes in the flow, are given by

$$\frac{\partial q}{\partial t} + A\frac{\partial q}{\partial x} + B\frac{\partial q}{\partial y} = 0. \tag{3.1}$$

Here, $q = (\varrho, u, v, w, p)$ is the primitive vector of perturbations around the mean flow, x is the direction normal to the boundary, y is the direction aligned to the boundary in

circumferential direction and A and B are constant matrices

$$A = \begin{pmatrix} \bar{u} & \bar{\varrho} & 0 & 0 & 0 \\ 0 & \bar{u} & 0 & 0 & \frac{1}{\bar{\varrho}} \\ 0 & 0 & \bar{u} & 0 & 0 \\ 0 & 0 & 0 & \bar{u} & 0 \\ 0 & \gamma\bar{p} & 0 & 0 & \bar{u} \end{pmatrix} \quad \text{and} \quad B = \begin{pmatrix} \bar{v} & 0 & \bar{\varrho} & 0 & 0 \\ 0 & \bar{v} & 0 & 0 & 0 \\ 0 & 0 & \bar{v} & 0 & \frac{1}{\bar{\varrho}} \\ 0 & 0 & 0 & \bar{v} & 0 \\ 0 & 0 & \gamma\bar{p} & 0 & \bar{v} \end{pmatrix}. \tag{3.2}$$

Variables denoted with a bar represent averaged values [28].
For the following analysis, wave like perturbations of the form

$$q = Re\left(\hat{q}e^{i(kx+ly-\omega t)}\right) \tag{3.3}$$

are considered. Here, ω is the frequency and k and l are the wave numbers along x and y, respectively. In terms of the linear theory, any flow solution can be reconstructed as a superposition of these fundamental waves.
The perturbations represented by equation (3.3) are substituted in the linearized Euler equations (3.1), which leads to

$$\left(-\omega I + kA + lB\right)\hat{q} = 0. \tag{3.4}$$

Equation (3.4) has non-trivial solutions, if

$$\det\left(-\omega I + kA + lB\right) = 0. \tag{3.5}$$

Equation (3.5) is called dispersion relation [10] and is a polynomial equation of degree five in ω, k and l [11].
In a next step, an eigenvector analysis is performed. Universally, the left eigenvector and right eigenvector of an arbitrary $N \times N$ matrix C are defined as

$$Cr_i = \lambda_i r_i \quad \text{and} \quad l_i C = \lambda_i l_i. \tag{3.6}$$

Here, r_i and l_i are the right and left eigenvectors of C. The right eigenvectors are column vectors and the left eigenvectors are row vectors, both of dimension N. λ_i represent the eigenvalues which corresponds to the eigenvectors [10].
By premultiplying the dispersion relation (3.4) by A^{-1}, it changes to the form

$$\det\left(-\omega A^{-1} + kI + lA^{-1}B\right) = 0. \tag{3.7}$$

This equation can be interpreted as a characteristic polynomial to an eigenvalue problem with eigenvalue $-k$

$$\left(-\omega A^{-1} + lA^{-1}B\right)r_i = -k_i r_i \quad , \quad l_i\left(-\omega A^{-1} + lA^{-1}B\right) = -k_i l_i. \tag{3.8}$$

With fixed values for ω and l, the eigenvalues k_i can be determined by solving the dispersion relation (3.5). The first three eigenvalues are identical

$$k_{1,2,3} = \frac{\omega - l\bar{v}}{\bar{u}}. \tag{3.9}$$

Using $k_{1,2,3}$, the polynomial equation of order five can be reduced to a polynomial equation of order two, which simplifies the calculation of $k_{4,5}$

$$(-\omega + k_{4,5}\bar{u} + l\bar{v})^2 = \bar{a}^2 \left(k_{4,5}^2 + l^2\right). \tag{3.10}$$

Solving equation (3.10) yields the last two eigenvalues of the dispersion relation

$$k_4 = \frac{(\omega - l\bar{v})\,(\bar{a}\Psi - \bar{u})}{\bar{a}^2 - \bar{u}^2}, \tag{3.11}$$

$$k_5 = -\frac{(\omega - l\bar{v})\,(\bar{a}\Psi + \bar{u})}{\bar{a}^2 - \bar{u}^2}, \tag{3.12}$$

with

$$\Psi = \begin{cases} \sqrt{\Delta} & \text{if} \Delta > 0, \\ i\text{sign}\,(\omega - l\bar{v})\,\sqrt{-\Delta} & \text{if} \Delta < 0 \end{cases} \tag{3.13}$$

and

$$\Delta = 1 - \frac{(\bar{a}^2 - \bar{u}^2)\,l^2}{(\omega - l\bar{v})^2}. \tag{3.14}$$

The eigenvectors can be determined from their corresponding eigenvalue. Since the first three eigenvalues are identical, the solutions for r_1, r_2 and r_3 are not unique. The only constraint while building these eigenvectors is that, for $i \neq j$, the eigenvectors r_i and l_j must be orthogonal to each other ($r_i l_j = 0$) [10]. One common way to choose the right eigenvectors is to define the first eigenvector as an entropy wave, the second eigenvector as an in-plane vorticity waves and the third eigenvector as an out-of-plane vorticity waves:

$$r_1 = \begin{pmatrix} -\bar{\varrho} \\ 0 \\ 0 \\ 0 \\ 0 \end{pmatrix}, \quad r_2 = \begin{pmatrix} 0 \\ \bar{a}m \\ \frac{\bar{a}}{\bar{u}}\,(\omega r + m\bar{v}) \\ 0 \\ 0 \end{pmatrix}, \quad r_3 = \begin{pmatrix} 0 \\ 0 \\ 0 \\ \bar{a} \\ 0 \end{pmatrix}. \tag{3.15}$$

Here, $m = lr$ is the dimensionless circumferential wave number and r is the radius. The fourth and fifth eigenvectors represent downstream and upstream running isentropic, irrotational pressure waves, i.e. acoustic perturbations [27]

$$r_{4,5} = \begin{pmatrix} \bar{\varrho} \\ \bar{a}\frac{k_{4,5}}{||\xi||} \\ \bar{a}\frac{l}{||\xi||} \\ 0 \\ \gamma\bar{p} \end{pmatrix}, \tag{3.16}$$

with

$$\xi = \begin{pmatrix} k \\ l \end{pmatrix}. \tag{3.17}$$

The right eigenvector matrix is defined as

$$R = \begin{pmatrix} r_1 & r_2 & r_3 & r_4 & r_5 \end{pmatrix} \tag{3.18}$$

and the left eigenvector matrix is obtained by inverting the right eigenvector matrix (3.18)

$$L = R^{-1} = \begin{pmatrix} l_1 \\ l_2 \\ l_3 \\ l_4 \\ l_5 \end{pmatrix} \tag{3.19}$$

At this point, a general physical interpretation of the left and right eigenvector can help to understand their role in the construction of NRBC. The right eigenvector represents the variation in the primitive variable induced by its corresponding fundamental wave [10].
As mentioned earlier the left eigenvector and right eigenvector of two different eigenvalues, k_i and k_j, are orthogonal. Thanks to this property, the left eigenvectors allow to measure the share of their corresponding right eigenvector in $\hat{q}$.
Fluctuations around the mean state can now be expressed by a weighted linear combination of right eigenvectors. Considering that the left eigenvector represents the share of its corresponding right eigenvector, the weight of the right eigenvector is $\alpha_i = l_i\hat{q}$ [28].

$$q\left(x,y,z,t\right) = Re\left(\left[\sum_{i=1}^{5} \alpha_i r_i e^{ik_i x}\right] e^{i(ly-\omega t)}\right). \tag{3.20}$$

In order to achieve perfectly non-reflecting behavior at the boundaries, for every combination of ω and l, the weight of the right eigenvector has to be zero, for all incoming waves. This results in the final non-reflecting boundary condition

$$l_i\hat{q} = 0, \tag{3.21}$$

for all i corresponding to incoming waves. Since only incoming waves must be suppressed, distinguishing between incoming perturbations and outgoing perturbations is a crucial step. If the flow is Fourier decomposed into wave-like perturbations (3.3), for fixed values for ω and l, each mode becomes a set of five fundamental waves, with distinct eigenvalues k_i. These eigenvalues are the negative wave numbers normal to the boundary. Therefore, they allow to determine the direction of propagation of their respective perturbations r_i, by analyzing the component of the group velocity normal to the boundary $\frac{\partial\omega}{\partial k}$.
Starting with the multiple root $k_{1,2,3}$, it is easy to see that the group velocity component normal to the boundary is $\frac{\partial\omega}{\partial k} = \bar{u}$. The perturbations propagate downstream. For the fourth and fifth roots, a case differentiation is necessary. In the first case, Δ is positive. This means that Ψ is real. When applied to the eigenvalues $k_{4,5}$, it results in one perturbation propagating in flow direction and the other propagating in the opposite direction. By choosing the positive real branch of the root $\sqrt{\Delta}$ it is assured that r_4 is always the downstream propagating perturbation. In the second case, Δ is negative. Therefore, Ψ is complex. By choosing the sign of Ψ as it is described in equation (3.13), $Im(k_4) > 0$ and r_4 propagates downstream. This is consistent with the decision taken for the case of Δ being positive. In the case of $\Delta = 0$, acoustic resonance occurs which complicates the construction of boundary conditions. Frey et. al [8] solved this issue by adding a small imaginary part to ω.

3.2 Implementation of Spectral NRBC

There are only very few applications for supersonic turbomachines and no supersonic boundary conditions are needed for the test cases presented in the current work. Further, since at supersonic boundaries no upstream running waves are present in the flow, the boundary conditions become trivial. Hence, supersonic boundary conditions are not described in the current work. Information about the implementation of supersonic NRBC in two-dimensional flows are presented by Giles [9].

At subsonic inflow boundaries, four waves are incoming and one is outgoing, and vice versa at the outflow boundaries. When the boundary conditions are applied, the outgoing perturbations have already been updated by the flow solver inside of the computational domain and need to be extrapolated to the boundary faces [23]. For this purpose, one-dimensional characteristic variables are introduced. Per definition, these variables coincide with the weight of the right eigenvectors α_i for plane waves normal to the boundary ($l = 0$). The transformations from primitive variables to characteristic variables and back are given by

$$c = L_{1d} q \quad \text{and} \quad q = R_{1d} c, \tag{3.22}$$

with

$$L_{1d} = L(l=0) = \begin{pmatrix} -\frac{1}{\bar{\varrho}} & 0 & 0 & 0 & \frac{1}{\bar{\varrho}\bar{a}^2} \\ 0 & 0 & \frac{1}{\bar{a}} & 0 & 0 \\ 0 & 0 & 0 & \frac{1}{\bar{a}} & 0 \\ 0 & \frac{1}{\bar{a}} & 0 & 0 & \frac{1}{\bar{\varrho}\bar{a}^2} \\ 0 & -\frac{1}{\bar{a}} & 0 & 0 & \frac{1}{\bar{\varrho}\bar{a}^2} \end{pmatrix} \tag{3.23}$$

$$R_{1d} = R(l=0) = \begin{pmatrix} -\bar{\varrho} & 0 & 0 & \frac{\bar{\varrho}}{2} & \frac{\bar{\varrho}}{2} \\ 0 & 0 & 0 & \frac{\bar{a}}{2} & -\frac{\bar{a}}{2} \\ 0 & \bar{a} & 0 & 0 & 0 \\ 0 & 0 & \bar{a} & 0 & 0 \\ 0 & 0 & 0 & \frac{\bar{\varrho}\bar{a}^2}{2} & \frac{\bar{\varrho}\bar{a}^2}{2} \end{pmatrix}. \tag{3.24}$$

To simplify the equations in the following section, compact forms of the eigenvector matrices and of the characteristic variable vector are introduced in which the outgoing and incoming characteristics are separated. To that end, the matrices are multiplied with P_{in} and P_{out}, which are the projection matrices onto the incoming and outgoing modes at the considered boundary [23]. So,

$$P_{in} = \mathrm{diag}(1,1,1,1,0) \quad \text{and} \quad P_{out} = \mathrm{diag}(0,0,0,0,1) \tag{3.25}$$

for an inflow boundary and vice versa for an outflow boundary. This yields the compact

forms

$$\left(\begin{array}{c} L^{in} \\ \hline L^{out} \end{array}\right) = \left(\begin{array}{c} l_1 \\ l_2 \\ l_3 \\ l_4 \\ \hline l_5 \end{array}\right) \quad , \quad \left(\begin{array}{c} c^{in} \\ \hline c^{out} \end{array}\right) = \left(\begin{array}{c} c_1 \\ c_2 \\ c_3 \\ c_4 \\ \hline c_5 \end{array}\right) \quad , \quad \left(R^{in} \;\middle|\; R^{out}\right) = \left(r_1 \quad r_2 \quad r_3 \quad r_4 \middle| \quad r_5\right) \tag{3.26}$$

at an inflow boundary and

$$\left(\begin{array}{c} L^{out} \\ \hline L^{in} \end{array}\right) = \left(\begin{array}{c} l_1 \\ l_2 \\ l_3 \\ l_4 \\ \hline l_5 \end{array}\right) \quad , \quad \left(\begin{array}{c} c^{out} \\ \hline c^{in} \end{array}\right) = \left(\begin{array}{c} c_1 \\ c_2 \\ c_3 \\ c_4 \\ \hline c_5 \end{array}\right) \quad , \quad \left(R^{out} \;\middle|\; R^{in}\right) = \left(r_1 \quad r_2 \quad r_3 \quad r_4 \middle| \quad r_5\right) \tag{3.27}$$

at an outflow boundary [28].

The implementation of spectral NRBC consists of two main steps: The treatment of the mean flow and the treatment of the circumferential and temporal perturbations.

3.2.1 Treatment of Mean Flow

First, a residual vector is defined as

$$\Re_{bd} = \begin{pmatrix} \bar{p}\left(\bar{s} - s_{bd}\right)/\bar{c_v} \\ \bar{a}\,\bar{\varrho}\left(\bar{v} - \bar{u}\tan\left(\alpha_{\theta,bd}\right)\right) \\ \bar{a}\,\bar{\varrho}\left(\bar{w} - \bar{u}\tan\left(\alpha_{r,bd}\right)\right) \\ \bar{\varrho}\left(\bar{h_t} - h_{t,bd}\right) \\ \bar{p} - p_{bd} \end{pmatrix}, \tag{3.28}$$

which is driven to zero in order to guarantee that the mean values at the boundaries correspond to the user defined boundary values. Here, the subscript *bd* denotes users defined boundary values. Further, s is the specific entropy, h_t is the specific stagnation enthalpy, α_θ is the angle between the velocity vector and the boundary normal in circumferential direction and α_r is the angle between the velocity vector and the boundary normal in radial direction [28, 9]. When using unsteady NRBC, mean quantities are spatially averaged in circumferential direction and temporally averaged over one period.
In TRACE, the boundary conditions are applied between two pseudo-timesteps. Since it is a cell-centered solver, the inner values are updated by the pseudo-time solver, while the face values are about to be updated by the boundaries. Therefore, it is necessary to update the mean characteristics at the faces, because of the pseudo-time updates of the outgoing characteristics in the interior of the domain. For that, an additional residual is defined, which drives the final solution on the boundary faces to match the averaged outgoing characteristics in the interior.

$$\Re_i = L_{1d}\left(\bar{q}_f - \bar{q}_i\right) \tag{3.29}$$

The subscripts i and f indicate the inner cell values and the face values, respectively [23]. Putting (3.28) and (3.29) together, the final residual reads

$$\Re = P_{in}\Re_{bd} + P_{out}\Re_i. \tag{3.30}$$

The required changes in characteristic variables are calculated using a Newton-Raphson step [28]

$$\Re + \frac{\partial \Re}{\partial c}\delta\bar{c} = 0. \tag{3.31}$$

The term $\frac{\partial \Re}{\partial c}$ can be written as

$$\frac{\partial \Re}{\partial c} = \frac{\partial \Re}{\partial q}\frac{\partial q}{\partial c}. \tag{3.32}$$

The solution for the derivation of the residual $\frac{\partial \Re}{\partial c}$ for two-dimensional flows have been presented by Giles [9] for the first residual (3.28) and by Robens et al. [23] for the complete residual (3.30).
In the end, by solving equations (3.31) for $\delta\bar{c}$, the update of the mean characteristics is obtained:

$$\delta\bar{c} = -\sigma L_{1d}\left(\frac{\partial \Re}{\partial q}R_{1d}\right)^{-1}\left[P_{in}\Re_{bd} + P_{out}\Re_i\right]. \tag{3.33}$$

The update of mean characteristics is multiplied with a relaxation factor σ in order to avoid numerical instability. The values used for σ are discussed in section 4.3.

3.2.2 Treatment of Perturbations

The flow field is temporally Fourier decomposed

$$\hat{q}_\omega = \frac{1}{T}\int_0^T q e^{i\omega t}dt, \quad \text{with} \quad T = N_p\Delta t. \tag{3.34}$$

Here, N_p is the number of timesteps per period. The highest frequency represented in the decomposition is defined by the Nyquist criterion. At this point a set of harmonics can be defined. In this case, the following steps are only performed for the frequencies corresponding to the harmonics defined by the set. For each frequency, the complex temporal Fourier coefficients of the primitive solution $\hat{q}_\omega$ are transformed into characteristic variables $\hat{c}_\omega$, using the transformation (3.22), and are Fourier decomposed circumferentially using:

$$\hat{c}_{\omega,l} = \frac{1}{P}\int_0^P \hat{c}_\omega e^{-ily}dy. \tag{3.35}$$

Here, $l = \frac{2\pi i+\theta}{P}$ is the wave number, P is the pitch and θ is the inter-blade phase angle. Temporally Fourier decomposed variables are from now on denoted by the subscript ω and circumferentially Fourier decomposed variables are denoted by the subscript l.
In order to achieve non reflecting properties, the boundary condition (3.21) has to be fulfilled for every combination of l and ω. This leads to

$$L^{in}\hat{q}_{(\omega,l),f} = 0 = L^{in}\left(R^{in}_{1d}\hat{c}^{in}_{(\omega,l),target} + R^{out}_{1d}\hat{c}^{out}_{(\omega,l),i}\right). \tag{3.36}$$

The Fourier coefficients of the mode corresponding to $\omega = 0$ and $l = 0$, represent the temporally averaged flow and are already treated in section 3.2.1. Therefore, this mode is not included in the application of equation (3.36). Modes corresponding to $l = 0$ and $\omega \neq 0$ are also excluded from the application of equation (3.36). These modes represent plain waves running orthogonally to the boundary, which also correspond to the instantaneous circumferential averaged perturbation about the temporal mean at the boundary. These modes are treated separately by extrapolating the instantaneous circumferential averaged outgoing characteristics. This step is performed without Fourier decomposing the solution. Instead, the characteristic update resulting from these waves reads

$$\delta\bar{c}_{\vartheta}^{out} = L_{1d}^{out}\left(\bar{q}_{\vartheta} - \bar{q}_{\vartheta,t}\right) \quad \text{and} \quad \delta\bar{c}_{\vartheta}^{in} = 0. \tag{3.37}$$

To be able to differentiate circumferentially averaged values from time averaged values, they are now denoted by the subscripts ϑ and t, respectively.
The matrices L and R are calculated from equation (3.19) and equation (3.18) for each combination of ω and l. Equation (3.36) is then solved for the target incoming characteristics

$$\hat{c}_{(\omega,l),target,f}^{in} = \left(L^{in}R_{1d}^{in}\right)^{-1} L^{in}R_{1d}^{out}\hat{c}_{(\omega,l),i}^{out}, \tag{3.38}$$

which represents the optimal value for incoming characteristics to prevent spurious reflections, as a function of the outgoing characteristics.
The outgoing characteristics on the faces are reconstructed by an upwinding from the interior [23]

$$\hat{c}_{(\omega,l),f,target}^{out} = \hat{c}_{(\omega,l),i}^{out}. \tag{3.39}$$

Using the backwards Fourier transformation

$$\hat{c}_{\omega,f,target} = \sum_{l} \hat{c}_{(\omega,l),f,target}e^{ily}, \tag{3.40}$$

the characteristics are transformed back into the temporal Fourier domain.
Since the treatment of the mean flow has already been performed in 3.2.1, the changes in incoming characteristics would lead to a shift of the mean values and the mean state would not meet the prescribed boundary values. To avoid this, the circumferential average of the previously calculated characteristic perturbations is subtracted from the target characteristic for each harmonic. This step is only performed if $\theta = 0$.
The target instantaneous characteristic perturbations are reconstructed from the temporally Fourier decomposed target characteristics using a backwards Fourier transformation

$$\delta\tilde{c}_{f,target} = \sum_{\omega} \hat{c}_{\omega,f,target}e^{-i\omega t}. \tag{3.41}$$

Since only modes with $l \neq 0$ are transformed back into the physical space, the result of the backwards Fourier transform is the target characteristic perturbation about the instantaneous circumferential average at each face $\delta\tilde{c}_{f,target}$.
This backwards Fourier transform, only includes frequencies defined in the set of harmonics. Therefore, for all other frequencies, $\hat{c}_{\omega,f,target}$ is treated as zero. This correspond to a one-dimensional non-reflecting treatment of the boundary solution (see subsection 3.3.1).
The target characteristic fluctuations are relaxed using the characteristic perturbation about the instantaneous circumferential average of the previous timestep $\delta\tilde{c}_{f,old}$

$$\delta\tilde{c}_{f} = (1-\sigma)\,\delta\tilde{c}_{f,old} + \sigma\delta\tilde{c}_{f,target}. \tag{3.42}$$

The complete characteristic update for each face is calculated by

$$\delta c_f = \delta \tilde{c}_f + \delta \bar{c}_\vartheta + \delta \bar{c}. \tag{3.43}$$

δc_f is transformed back into a primitive update by means of the transform (3.22) and is added to the temporal and circumferential averaged flow $\bar{q}_{\vartheta,t}$, to obtain the new primitive boundary face values. In a final step the boundary face values are extrapolated to the ghost cells.

3.3 Other NRBC

The goal of the present work is to find a good agreement between the prediction accuracy and the computational cost of spectral NRBC. For this purpose, references are needed to assess the quality of the solution. Therefore, in addition to simulating the test cases using spectral NRBC, they are also simulated using 1D unsteady NRBC, 2D steady NRBC and approximate NRBC. In this section, the concepts behind these boundary conditions are described briefly.

3.3.1 1D Unsteady NRBC

For these NRBC, the auxiliary variable

$$\lambda = \frac{l}{m} \tag{3.44}$$

is introduced. In this variation of unsteady NRBC, additionally to neglecting perturbations in radial direction, perturbations are also neglected in circumferential direction [19]. This means that

$$\lambda = 0. \tag{3.45}$$

Substituting equation (3.45) in the eigenvector matrices (3.19) and (3.18), results in the one-dimensional formulations of the eigenvector matrices (3.23) and (3.24). The non-reflecting boundary condition now reads

$$Lq = L_{1d}q = 0 \tag{3.46}$$

which coincides with the characteristic transform (3.22). This leads to the one-dimensional NRBC

$$c_i = 0, \tag{3.47}$$

for all i corresponding to incoming waves. Therefore, at the inlet of the domain the first four characteristics are set to zero and at the outlet the fifth characteristic is set to zero. Additionally, outgoing characteristics are extrapolated from the interior. The primitive boundary values are reconstructed using the backwards transformation of (3.22).
Since now the left eigenvector matrix L is independent of l and ω, these are local boundary conditions. So, no Fourier decomposition of the flow is necessary.

3.3.2 2D Steady NRBC

These NRBC have been introduced by Giles [10] for steady simulations. In steady flows there are no temporal fluctuations. Thus, only circumferential fluctuations are considered, which corresponds to perturbations with the frequency $\omega = 0$. Therefore, no temporal Fourier decomposition is necessary.
To apply the NRBC, the treatment of the averaged flow and the treatment of the perturbations about the circumferential average are separated. The treatment of the averaged flow corresponds to the previously presented method for the mean flow in the spectral NRBC, but all averaged quantities are now only averaged circumferentially [9].
The perturbations about the circumferential average are calculated as

$$\tilde{q} = q - \bar{q}_\vartheta. \tag{3.48}$$

The perturbations are circumferentially Fourier decomposed. The characteristic updates at each face are calculated for every mode except $l = 0$ and $\omega = 0$, in the same manner as in the implementation of the spectral unsteady NRBC.
Due to the lack of prescribed incoming perturbations, the entropy and enthalpy are uniform along the inlet within the linearized theory. Still, second order perturbations may be present in the flow. Therefore, in the physical domain, the condition for the second and fourth characteristics updates are replaced. Instead, uniform enthalpy and entropy are imposed, by driving the residual

$$\begin{pmatrix} \tilde{\Re}_1 \\ \tilde{\Re}_2 \end{pmatrix} = \begin{pmatrix} \bar{p}\tilde{s} \\ \bar{\varrho}\tilde{h_t} \end{pmatrix} \tag{3.49}$$

to zero, with the help of a Newton-Raphson step [28].
A more detailed implementation of the steady two-dimensional NRBC can be found in [28] and [9].
When steady NRBC are applied to unsteady flows, temporal perturbations are present in the flow. Still, the boundary conditions are only applied to the instantaneous perturbations with the frequency $\omega = 0$, following the procedure described in this section. This can lead to spurious reflections.

3.3.3 Approximate NRBC

The goal of approximate NRBC is to circumvent the fact that unsteady two-dimensional NRBC are non-local in time and space [11]. This method was presented by Engquist and Madja [7] for the wave equation. Giles [10] applied it to the two-dimensional linearized Euler equation, with focus on turbomachinery applications.
The treatment of the mean flow does not differ from that of the spectral NRBC [28]. To avoid having to Fourier decompose the flow solution at the boundaries, the left eigenvector matrix is expanded as a Taylor series about the 1D unsteady NRBC. Here, a second order approach is chosen

$$L_a = L|_{\lambda=0} + \lambda \frac{\partial L}{\partial \lambda}\bigg|_{\lambda=0}. \tag{3.50}$$

Multiplying the boundary condition (3.21) with ω and substituting $\omega = i\frac{\partial}{\partial t}$ and $l = -i\frac{\partial}{\partial y}$ in equation (3.50), yields one possible approximate formulation of the NRBC

$$L_a^{in}\frac{\partial \tilde{q}}{\partial t} - \frac{\partial L^{in}}{\partial \lambda}\Big|_{\lambda=0}\frac{\partial \tilde{q}}{\partial y} = 0. \tag{3.51}$$

By transforming the primitive perturbations into characteristic variables and extrapolating the outgoing characteristics from the interior of the domain, one obtains differential equations for the inlet and outlet characteristic boundary values. The complete formulation of the differential equations for a three-dimensional subsonic boundary have been presented by Schlüß et al. [28]. The solution algorithm for these equations is presented by Ashcroft et al. [2].
Using a Taylor series which is of second order in λ causes the boundary conditions to only be perfectly non-reflecting for plane waves impinging normally on the boundary. The reflections become stronger for increasing λ. So, the error increases for large circumferential wave numbers at low frequencies [28]. Giles also shows that this formulation is not well-posed. To solve this issue, the perfect orthogonality between l_4 and r_5 is given up. Thanks to this, the problem is well-posed, but the boundary loses its optimal non-reflecting behavior with regard to the approximation.
An improvement of the approximate NRBC has been shown by Henninger et al. [14], by implementing higher order formulations proposed by Hagstrom [12]. In the current work, only the second order approach is used.

4 Rig250

Goal of the current work is to improve the efficiency of spectral NRBC, by reducing the number of harmonics, to which the modal approach is applied. To maintain a comparable prediction quality, it is imperative to understand at which harmonics significant unsteady fluctuations are reflected. Therefore, it is important to define a realistic test case, which correctly represents unsteady perturbations in turbomachines. In this chapter, the research compressor Rig250 of the German Aerospace Center [29], is considered and analyzed.
This axial compressor comprises four stages and an inlet guide vane in front of the first stage. In the current work, the compressor is reduced to a three-row configuration, consisting of stator 1 (S_1), rotor 2 (R_2) and stator 2 (S_2). By considering more than two rows, interactions between non-adjacent rows, such as indexing effects, can be identified. Their influence on the non-reflecting behavior at the boundaries can then be evaluated. Choosing a configuration close to the front of the compressor yields a transonic flow field containing shocks. The blade counts in this configuration are 36:28:48. This convenient blade count ratio allows to reduce the computational domain to a quarter wheel. Furthermore, this test case is computed as a quasi-three-dimensional (Q3D) case. The spectral NRBC do not take three-dimensional perturbations into account. Therefore, a Q3D domain is sufficient to correctly represent the non-reflecting behavior of the spectral NRBC. Using a Q3D quarter wheel instead of a three-dimensional full wheel configuration, reduces the computational effort significantly. Thus, many variations of the set of harmonics included in the NRBC can be simulated in a reasonable time.
In section 4.1, the numerical setup for the simulations of the compressor is presented. First, the generation of a Q3D computational domain is described. Then, the numerical models and methods used in TRACE and the simulation's settings are presented.
Before focusing on the results of the simulation, in section 4.2, the computational costs of the spectral NRBC are examined and compared with the costs of other NRBC. Thereby, the necessity for an improvement in efficiency is highlighted. First, the distribution of the computational costs between the tasks in the boundary conditions is analyzed. Then, special attention is given to the changes in computational effort when varying the size of the domain, the number of harmonics included in the spectral NRBC and the number of processes used to simulate the test case.
Section 4.3 addresses the issue of slow convergence at the boundaries, when using spectral NRBC.
Finally, in section 4.4, the results of the simulations of Rig250 are analyzed. A concept for the choice of a reduced set of harmonics is derived from these results. In a first step, fundamental frequencies are defined. The number of harmonics of these frequencies included in the spectral NRBC is lowered step by step. The impact of the reduction of the set of harmonics on the the solution is analyzed. In a second step, the behavior of unsteady fluctuations at individual harmonics is examined inside of the computational domain. This yields information about the relevance of each harmonic in regard to the reflections at the boundaries. Irrelevant harmonics are strategically excluded and a new set of harmonics is defined. With this set, another simulation of Rig250 is performed. In

a final step, the solution of this setup is compared with setups using different NRBC.

4.1 Computational Setup

4.1.1 Generation of a Q3D Computational Domain

Starting point for the generation of the Q3D mesh is an already existing three-dimensional solution of the entire compressor. This solution was used in earlier works at the DLR's Institute for Propulsion Technology [17]. Figure 4.1 displays the original mesh. Since only S_1, R_2 and S_2 are considered in the current work, the first step is to delete the mesh and the solution of all other rows. This is done using the General Mesh Connector (GMC) which is developed by the MTU and is the preprocessing tool used for the flow solver TRACE at the DLR's Institute of Propulsion Technology. This leads to a three-dimensional mesh of the desired stator-rotor-stator configuration. This reduced configuration is framed red in Figure 4.1.
The second step consists of creating a S2M mesh of the reduced three-dimensional domain. This step is performed using POST, which is a postprocessing tool integrated in TRACE. The resulting S2M mesh is shown in Figure 4.2. It consists of 176 cells in i-direction and 70 cells in j-direction. The steady solution is mass-averaged on the S2M mesh. To achieve realistic flow conditions, the Q3D mesh is embedded between two streamsurfaces. The locations of these streamsurfaces are defined by evaluating the mass averaged S2M flow solution with regards to the relative mass flow. Two lines of constant relative mass flow at 94.5% and at 95.5% are defined. The area between the two lines is isolated and remeshed. The position of the new mesh is represented by the red area in Figure 4.2. The resulting Q3D S2M grid has now a resolution of 176 cells in i-direction and 3 cells in j-direction. Multiple cells in j-direction are necessary for the representation of radial pressure gradients.
The next step is to generate the S1-topology for the Q3D mesh. With the Q3D S2M mesh and the information about the blade geometry, PyMesh [34] can generate a Q3D mesh

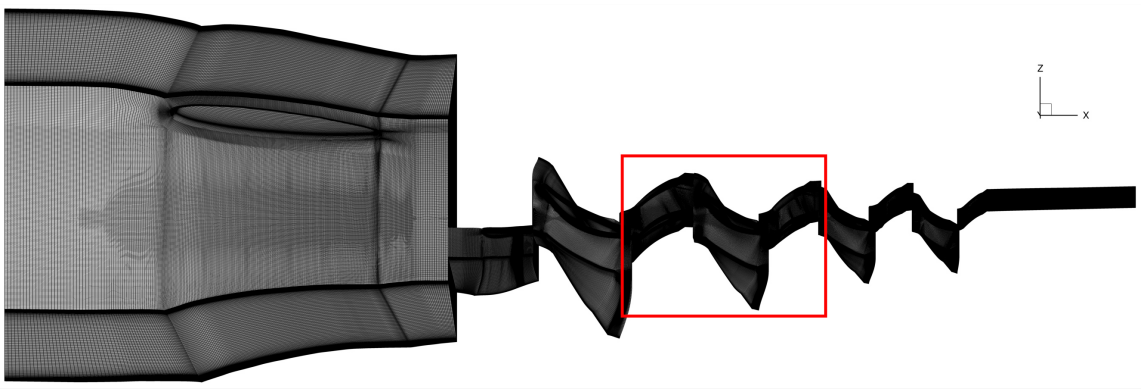

Figure 4.1: Original three-dimensional computational domain of the entire compressor. The S_1-R_2-S_2 configuration is framed in red.

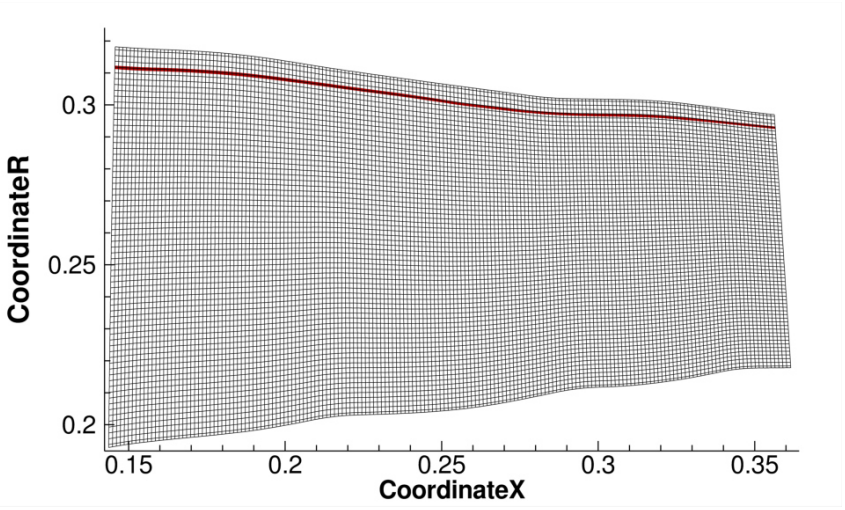

Figure 4.2: S2M grid of the S1-R2-S2 configuration. The red line represents the area between 94.5% and 95.5% relative mass flow.

of a one blade passage for each row. PyMesh is a structured multiblock grid generator developed at the Institute of Propulsion Technology. The S1-topology is generated using a basic O-C-H topology. The blades are wrapped in O-type blocks which are surrounded by C-type blocks. For the inlet areas and outlet areas of each row as well as the blade channels, H-type blocks are used. The hub and tip regions of the Q3D mesh are located close to the tip of the original three-dimensional mesh. So, the S1 meshing parameters of the tip wall of the original mesh are used as hub and tip parameters for the Q3D mesh. The fillet and the blade clearance are removed. The individual meshes are assembled to one single passage mesh of the complete configuration in GMC.

Figure 4.3: Final computational mesh of the S1-R2-S2 configuration of the Rig250 as quarter wheel configuration.

In a final step, the single passage mesh is duplicated to a quarter wheel. This corresponds to nine vanes in S_1, seven blades in R_2 and twelve vanes in S_2. Figure 4.3 shows the final computational mesh used for all simulations of Rig250 in the current work. The final mesh consists of 2,426,592 cells.
In the current work, simulations are performed using 72 processes. With the inhouse block splitting tool the mesh is split in 252 blocks. This yields a theoretical load balance efficiency of 94.4%.

4.1.2 Numerical Methods and Settings

In the current work, the flow solver TRACE, developed at the DLR's Institute of Propulsion Technology, is used for all simulations. It is a fully implicit three-dimensional steady and unsteady multiblock finite-volume solver. It solves the Favre-averaged and Reynolds-averaged compressible Navier-Stokes equations [3]. TRACE is a hybrid solver for structured and unstructured grids. A second order accurate Roe upwind scheme is used to discretize the convective fluxes [24]. The second order accuracy is achieved through a Van Leer MUSCL extrapolation [33], with the Van Albada slope limiter [32] to suppress unphysical numerical oscillations. Viscous terms are discretized using a second-order accurate central difference scheme. More detailed information on the implementation of TRACE can be found in [3].
In the current work, all simulations are non-linear time marching simulations. The temporal discretization is performed using an implicit second order backwards scheme and a pseudo time method for the subiterations of single timesteps [28]. A predictor-corrector method is used as time marching method [16]. The temporal resolution is 768 timesteps per period. This corresponds to 64 timestep per S_2 vane passage. At each timestep, 30 subiterations are performed. A constant CFL number of 200 is preset. The spatial discretization is performed on the grid described in subsection 4.1.1. The fluid is modeled as an ideal gas. A constant specific heat ratio of $\gamma = 1.4$ and a constant Prandtl number of 0.9 are assumed. The Wilcox k-ω model [35] is used for the representation of the turbulence. The test case is assumed to be fully turbulent, therefore no transition model is used.
At the inlet and outlet boundaries, NRBC are applied. The boundary values at the inlet

Table 4.1: Boundary values at the inlet and at the outlet of the domain.

Boundary	Variable	Boundary value
Inlet	Total pressure p_t	116025 Pa
	Total temperature T_t	331.735 K
	Radial flow angle α_r	-4.0765°
	Circumferential flow angle α_θ	49.879°
	Turbulent intensity Tu	0.061
	Eddy length scale L_T	0.000726 m
Outlet	Static pressure p	148206 Pa

and at the outlet of the domain are extracted from the three-dimensional solution. At the inlet, values for the total pressure, the total temperature and the flow direction are imposed. In addition, the turbulent intensity and the turbulent length scale are prescribed. At the outlet the static pressure is specified. The boundary values are shown in Table 4.1. The blades are computed as viscid walls, with a low Reynolds modeling approach for the turbulent boundary layer. The hub and casing areas are computed as inviscid walls. At the circumferential limits of the domain, periodic boundaries are prescribed. For the interface between two rows, sliding grids are applied, using the zonal algorithm of Yang et al. [36]. In this configuration the base frequency is 848 Hz. This corresponds to the quarter wheel passing frequency at a rotational speed of 12720 RPM.
The initialization of the flow in the domain, is done with a steady solution which is calculated beforehand. A base setup is defined. In this setup, spectral NRBC are imposed at the inlet and outlet boundaries. The set of harmonics for the spectral NRBC includes all harmonics up to the Nyquist frequency. Once this setup reaches a converged solution, it becomes the starting point for all further simulations of Rig250, using different sets of harmonics or different NRBC. Each variation is simulated for 15 periods.

4.2 Performance Analysis

In this section, a performance analysis is conducted, to point out the necessity for a decrease in computational costs of spectral NRBC and to identify potential efficiency improvements. The computational costs presented in this section are only valid for the current Q3D configuration and vary in three-dimensional configurations.

This analysis is performed using the General Purpose Timing Library (GPTL). This tool was written by Jim Rosinski and can be acquired from [25]. GPTL is a library for C, C++ and Fortran which allows to measure the computation time of serial and parallel programs. The timer starts and stops when a process passes manually implemented

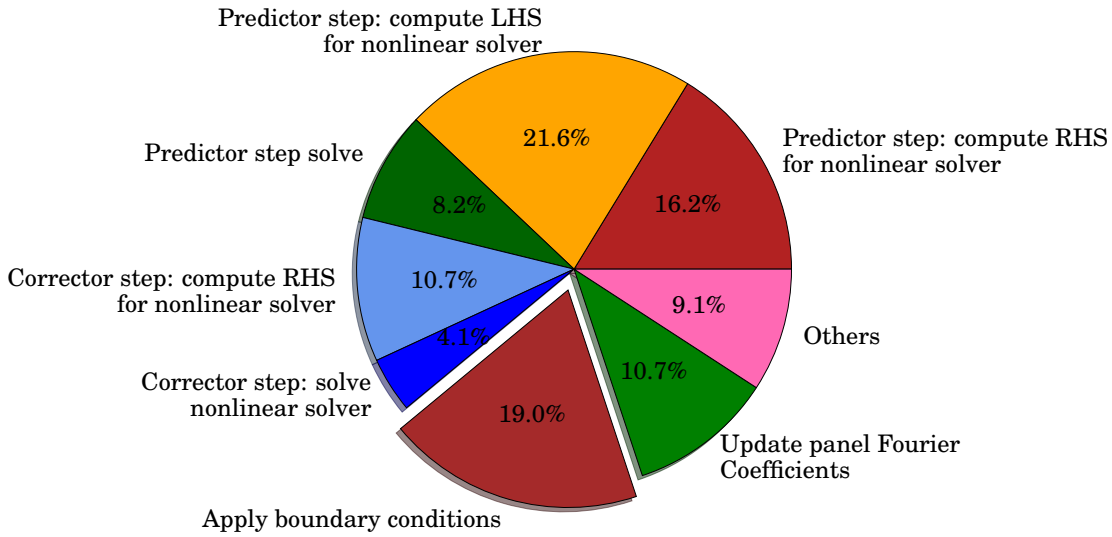

Figure 4.4: Average distribution of the computational cost in an iteration loop.

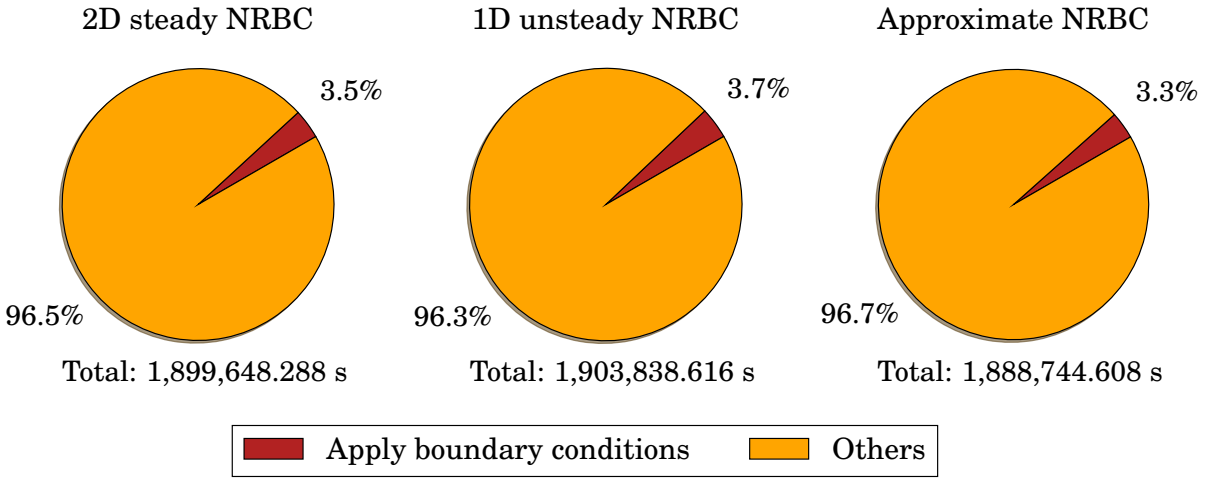

Figure 4.5: Comparison of the average percentage of the iteration loop represented by "Apply boundary conditions" using various NRBC

flags. Each flag counts the number of times each process starts the timer. The manual implementation allows for an in-depth analysis on several layers.
The first part of this analysis focuses only on the base setup. The objective is to obtain an overview of the distribution of the computational costs between the different tasks. Simulations can be split in two main parts: The setup and the iteration loop. Compared to the iteration loop, the share of the computational costs of the setup will decrease with an increasing number of simulated timesteps. Therefore, the setup of the simulation is not considered in this analysis.
In a first step, the iteration loop is decomposed into smaller tasks. Figure 4.4 shows the average distribution of the computational costs in one iteration loop. Here, "Others" combines all tasks with percentages smaller than 2%. In sum, the predictor-corrector steps equal 60.8% of the iteration loops and the update of the Fourier coefficients for the two-dimensional Fourier output equals 10.7% of the iteration loop. With 19%, the application of the NRBC represents nearly one fifth of a timestep.

In Figure 4.5 the average share of "Apply boundary conditions" in one iteration loop is displayed for all NRBC presented in section 3.3. The total computation time spent in the iteration loop over two periods is written under the respective pie charts. The radius of the pie chart is proportional to the computational costs of the iteration loop. The application of the NRBC shows the lowest costs for approximate NRBC, followed by the 2D steady NRBC and finally the 1D unsteady NRBC. However, these three NRBC show only small difference in computational costs. In comparison, the application of the spectral NRBC is 510% more expensive then the application of the 1D unsteady NRBC. This leads to 18.9% higher computational costs for the average iteration loop.
To be able to accelerate the application of the spectral NRBC, it is important to identify which task consumes most resources. Therefore, "Apply boundary conditions" is further decomposed. It consists mainly of the routine "nrbcUnsteady". Here, the NRBC are applied to each inlet and outlet boundary face. "nrbcUnsteady" represents 85.6% of "Apply boundary conditions". In the base setup, only 21 Processes out of 72 enter the routine "nrbcUnsteady". The remaining 14.4% stem from the other 51 processes, which apply other boundary conditions, such as wall boundary conditions.

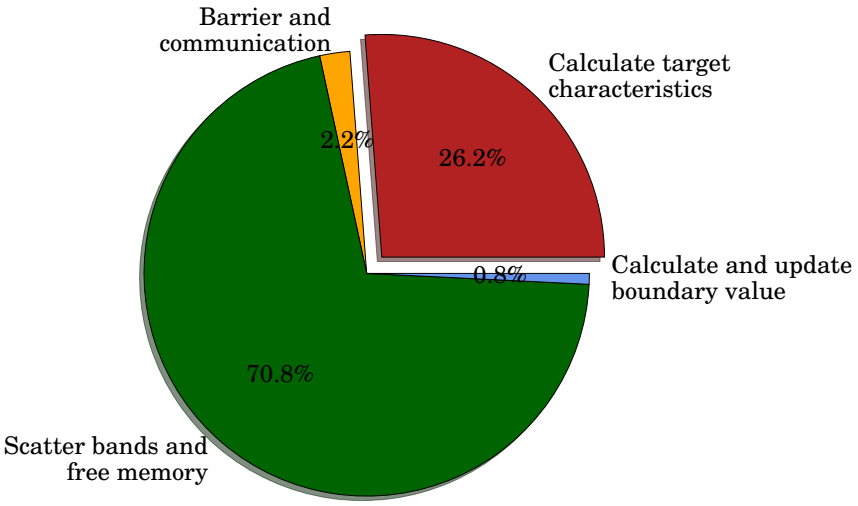

Figure 4.6: Average distribution of the computational costs in the routine "nrbcUnsteady".

Figure 4.6 shows the decomposition of "nrbcUnsteady" into smaller tasks. In "Barrier and Communication", the simulation waits for all 21 involved processes to reach a barrier, before starting the actual application of the NRBC. Then, the data from the different boundary panels are gathered and transmitted to the bandmasters. A bandmaster is a process to which at least one band is assigned during the simulation's setup. Bands regroup all cells at a boundary with corresponding radial positions. Each bandmaster applies the NRBC to its assigned bands. This procedure is necessary because of the spatially nonlocal nature of the spectral NRBC. In "Calculate target characteristics" the bandmaster calculates the optimal update of characteristic variable to suppress incoming perturbations. In "Calculate and update boundary values" the new primitive boundary values at each face are determined from the previously calculated ideal incoming characteristics. Finally, in "Scatter bands and free memory" the new boundary values are redistributed from the bandmasters to their original processes and the memory is freed. All other tasks that are part of the application of the boundary conditions, such as calculating the update due to the mean flow or the initialization of variables, are not represented in Figure 4.6, because their share is less than 0.05% of "nrbcUnsteady".

"Scatter bands and free memory" represents the largest portion of "nrbcUnsteady". To scatter the new boundary values back to their original processes, a blocking communication is employed. This ensures that every boundary value has been communicated before any process can go on to the next task. In the base setup, the boundary consists of three bands at the inlet and three bands at the outlet. So, six out of 21 processes are bandmasters and process one band each. This means that 15 processes must wait for the six bandmasters to apply the NRBC. These long idle times raise the computational time of "Scatter bands and free memory", even though no actual calculations are being performed. This implies that reducing the computational costs of other tasks will also reduce the computational costs of "Scatter bands and free memory".

Since the computational costs for "Barrier and Communication" and "Calculate and update boundary values" depend on the number of faces per band, the largest potential for an efficiency increase lies in "Calculate target characteristics". This is exactly the aim

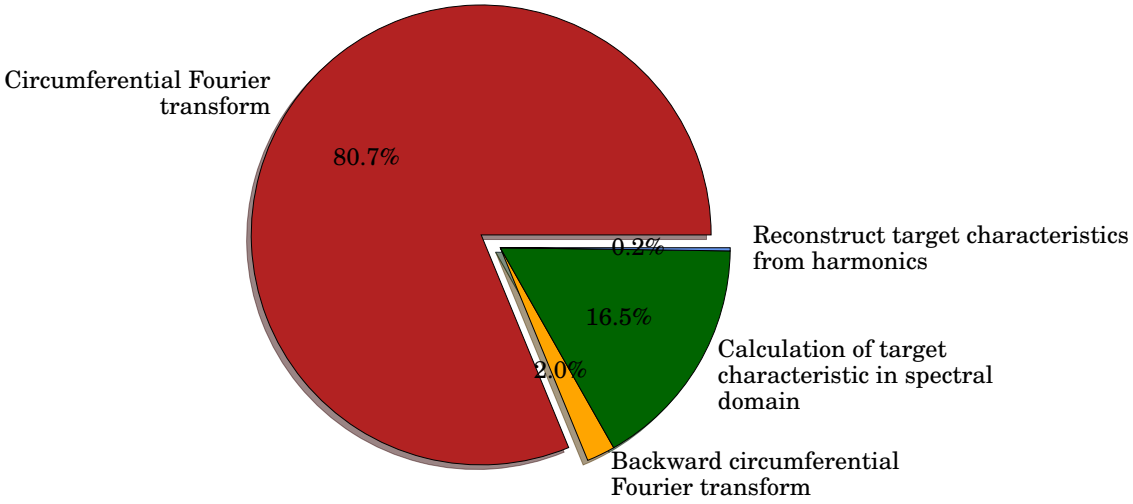

Figure 4.7: Average distribution of the computational costs in the task "Calculate target characteristics".

of the current work. The target characteristics must be calculated for every mode independently. This means that by reducing the number of harmonics for which the modal analysis is performed, the costs of "Calculate target characteristics", as well as the costs for "Scatter bands and free memory", will decrease linearly.

Another possibility to reduce the computational costs of spectral NRBC is to lower the number of circumferential wave numbers for which the modal analysis is performed. In "Calculate target characteristics", the solution at each temporal harmonic is Fourier

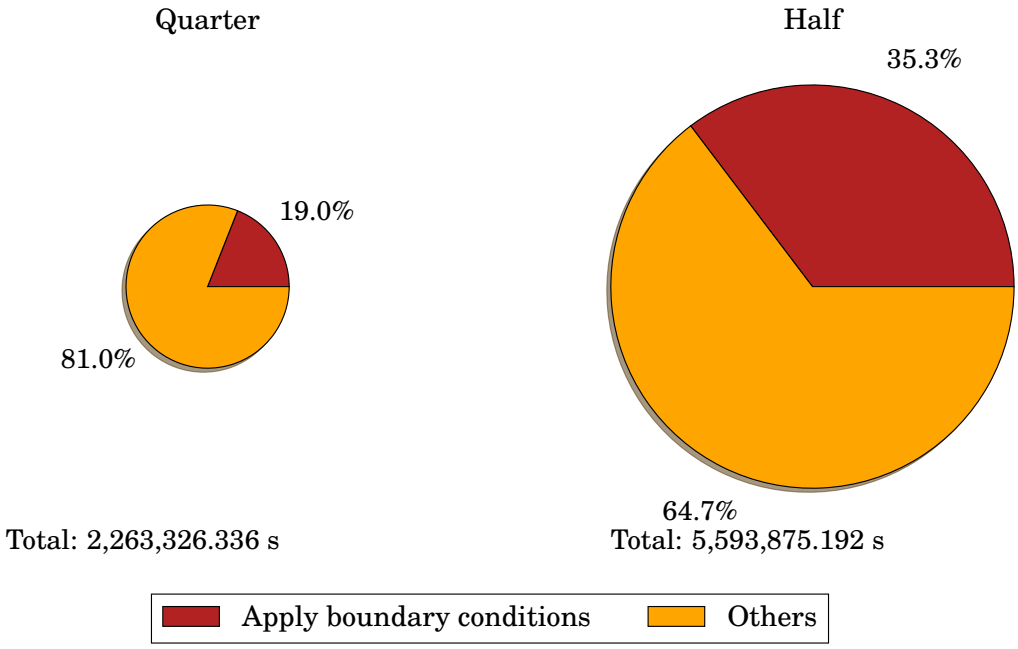

Figure 4.8: Comparison of the average percentage of the iteration loop represented by "Apply boundary conditions" using a quarter wheel and a half wheel as computational domains.

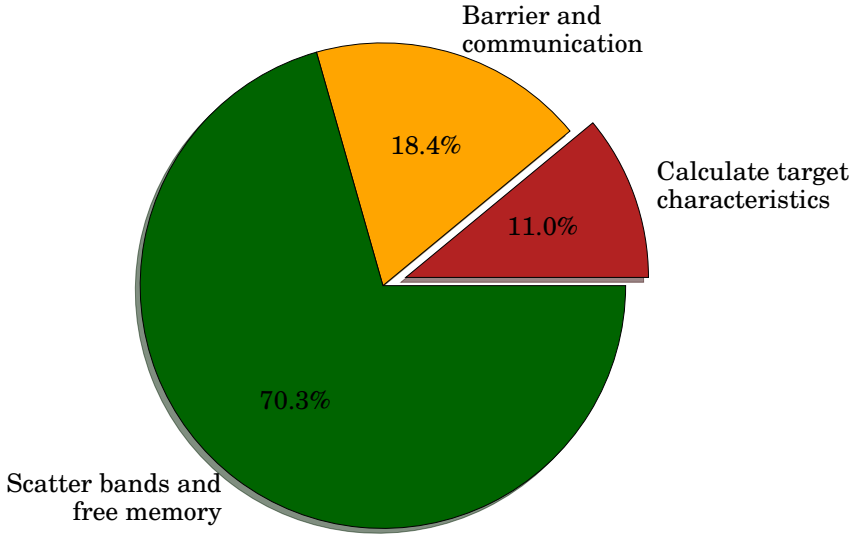

Figure 4.9: Average distribution of the computational costs in the routine "nrbcUnsteady" for the half wheel configuration.

decomposed circumferentially. Then, a boundary update is defined in term of incoming characteristics for each possible mode. So, lowering the amount of wave numbers, will lower the amount of combinations for the frequency and the wave number. The instantaneous characteristic boundary updates are reconstructed via an inverse Fourier transform. In Figure 4.7, the task "Calculate target characteristics" is broken down into its four main tasks. The circumferential Fourier transform represents about 80% of the task, while the actual calculation of the target characteristic only represents 16.5%. In TRACE, a Fourier transform library is used. Therefore, the computational costs of the Fourier decomposition are defined by the amount of data points defined as input. So, ignoring certain wave numbers will not lower its computational cost. This means that the potential for an efficiency increase with this method is limited to the remaining 19.3% of "Calculate target characteristics" per considered harmonic. Ignoring a harmonic entirely skips the task "Calculate target characteristics", for said harmonic.

To analyze the scaling properties of spectral NRBC in large configurations, the computational domain is enlarged from a quarter wheel to a half wheel. The number of cells per blade passage remains unchanged and the number of timesteps per period is doubled. Figure Figure 4.8, shows the comparison of the share of the application of the boundary conditions for both domains. For the half wheel, the share of "Apply boundary conditions" increases drastically from 19% to 35.3%. This corresponds to a total increase in computational costs of the NRBC of 359%. The rest of the iteration loop increases nearly linearly with the number of cells. The overall increase in computational costs of the iteration loop is 147.2%
In Figure 4.9, the routine "nrbcUnsteady" is split into smaller tasks. Compared to the base setup, the computational costs of "Barrier and Communication" are subject to an increase of 2840.4%. This increase results mainly from the barriers and not from the communication. The computational costs of "Calculate target characteristics" increase by 108.8%. The Fourier transform at the boundaries are performed using the Fourier transform library [18]. Therefore, the order of the costs for a Fourier transform of a band

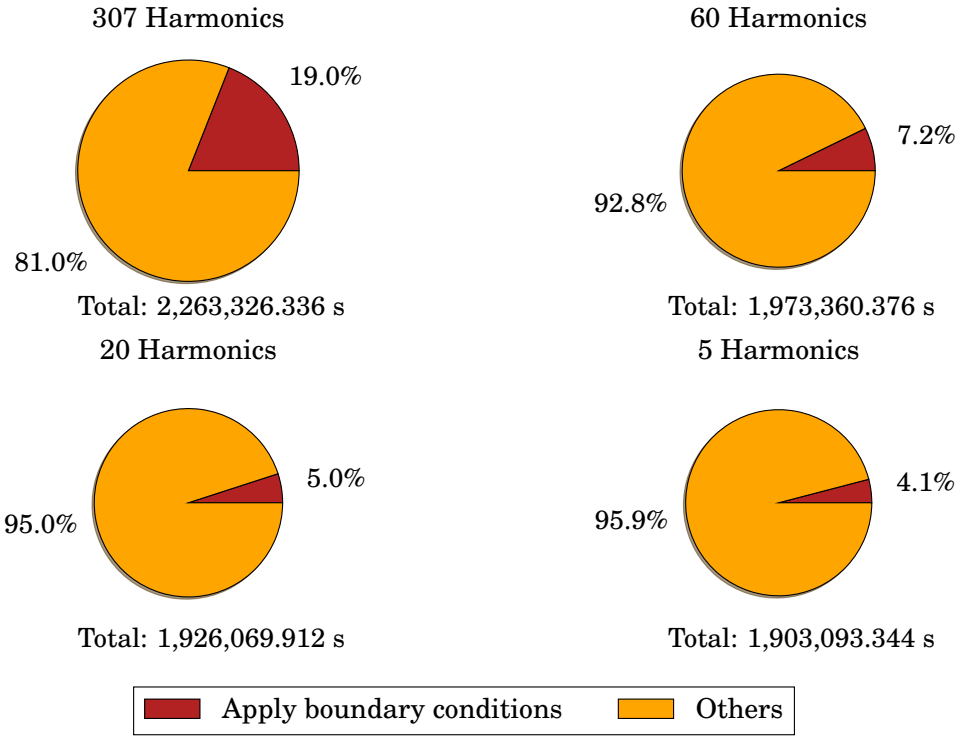

Figure 4.10: Comparison of the average percentage of the iteration loop represented by "Apply boundary conditions" using various amount of harmonics in the NRBC.

with n faces is reduced from $\mathcal{O}(n^2)$ to $\mathcal{O}(n\log(n))$. Here, the analysis shows that the circumferential Fourier transform increases in costs by 110.3%. The computational costs of the task "Scatter bands and free memory" see an increase of 300% compared to the base setup. This strong increase is due to the fact that one bandmaster applies the NRBC to two bands. It causes higher waiting times for the remaining processes. Unfortunately, it is not possible to control the definition of the bandmasters.
Next, the number of processes used to simulate the setup is varied to observe if costs through idle times increase. This variation does not show any strong variations in the computational costs. The average costs of the iteration loop increase slightly with increasing number of processes. This is due to the fact that blocks are not split to achieve a better load balance efficiency. The costs to apply the NRBC decrease slightly when using more processes.
Finally, the sets of harmonics used at the inlet and outlet NRBC are varied. Three simulations are performed using 5, 20 and 60 harmonics at each boundary. Figure 4.10 shows a comparison of the costs of the spectral NRBC considering the different sets of harmonics. The results show that, as expected, the computational costs of the application of the NRBC decrease in a linear manner. Reducing the set of harmonics to 60 harmonics at each boundary, already yields computational costs that are only double the costs of other NRBC. The percentage of the iteration loop represented by the spectral NRBC is only double the share resulting from using the 1D unsteady NRBC. In comparison to the base setup, the computational costs of the iteration loop decrease by 12.8% when using 60 harmonics, by 14.9% when using 20 harmonics and by 15.9% when using 5 harmonics.

4.3 Convergence

During the simulation of the base setup, the time averaged values at the boundaries converge slowly towards the user defined boundary values. This has already been observed by Chassaing and Gerolymos [5]. They related the weak convergence to the temporal Fourier coefficients evolving slowly. In the current work, it is found that the small relaxation factor σ for updates of the mean flow in equation (3.33) is also a reason for the slow convergence. For a stable setup the relaxation number is defined as a function of the number of timesteps per period N_p,

$$\sigma(N_p) = \frac{4}{N_p}. \tag{4.1}$$

This leads to approximately constant changes of boundary values in one period independently of the temporal resolution. When simulating large configurations, like quarter wheels, half wheels or full wheels, the period increases. So, N_p has to be increased with every added blade passage to achieve an equal temporal resolution of the blade passing period. This leads to very small relaxation factors. For the base setup the relaxation factor is $\sigma = 4/768 = 0.0052$. Figure 4.11 shows the convergence of the time averaged pressure at the outlet of S_2 for the base setup. Here, the red curve represents the original relaxation factor and the black line represents the user defined boundary value for the outlet pressure
In a first attempt to accelerate the convergence, the relaxation factor is multiplied by five. This already yields a faster convergence without showing any signs of instability. This is represented for the base setup by the blue curve in Figure 4.11. The factor five is chosen

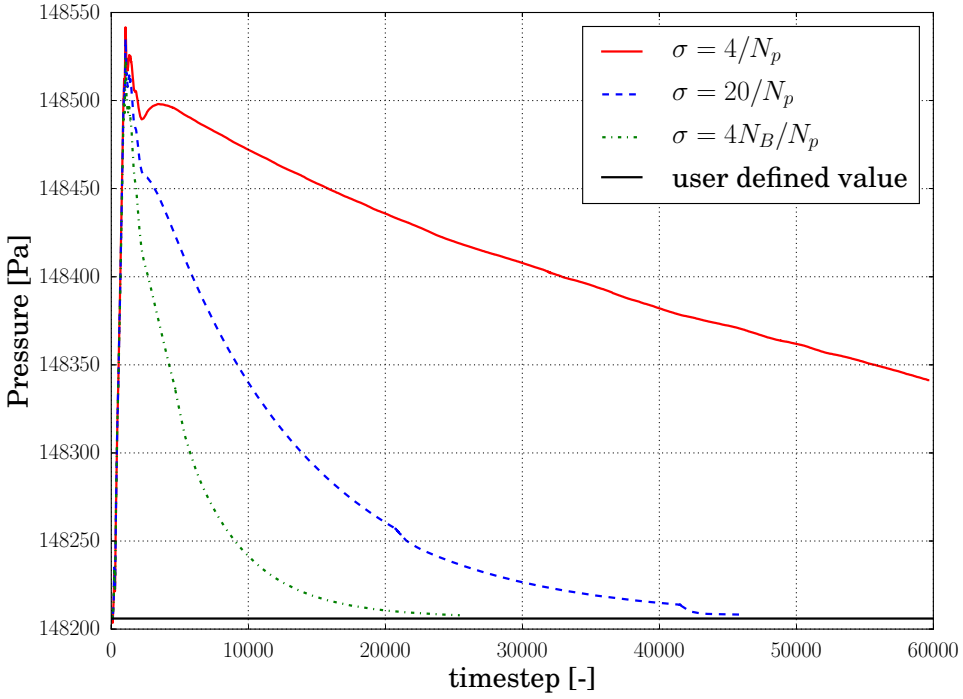

Figure 4.11: Temporal and spatial average of the pressure over the simulated timesteps for different relaxation factors at the outlet of S2.

arbitrarily. This test shows that the relaxation factor used at the moment is far from the limit of stability for this setup.
In a second attempt, the relaxation factor has been connected to the number of simulated blade passages in each row. For that purpose, the relaxation factor is multiplied by the number of simulated blade passages in the row adjacent to the boundary N_B. This leads to a relaxation factor of

$$\sigma = \frac{4N_B}{N_p}. \tag{4.2}$$

This relaxation factor differs at the inlet and at the outlet. The corresponding convergence is represented by the green curve in figure 4.11. Here, the aim is to scale the relaxation factor such that changes in boundary values over one blade passing period remains approximately constant. Therefore, increasing the size of the considered wheel segment or the temporal resolution, does not lead to weaker convergence.
This method has the potential to significantly improve the convergence rate of the boundary values. But it is entirely empirical and needs testing regarding overall stability.
Another method which has not been pursued in the current work, is to connect the relaxation factor to the dominant frequency of unsteady fluctuations in the row adjacent to the boundary. In the base configuration of Rig250, it corresponds to the blade passing frequency of R_2.

4.4 Results and Discussion

The current section focuses on how the prediction quality of the spectral unsteady NRBC and the number of harmonics to which the modal approach is applied are related. A concept for the reduction of the set of harmonics is developed. The objective is to find a set which is small enough to significantly reduce the computational costs of spectral NRBC, but large enough to not impair the solution.
This objective is achieved in four main steps. In a first step, fundamental frequencies of the configuration are defined. In a second step, sets of harmonics are defined containing a certain number of harmonics of all fundamental harmonics. Simulations using these sets are performed. The variation of the solution stemming from the different sets is investigated. In a third step, the unsteady fluctuations are analyzed individually at each harmonic. This yields information about the relevance of each harmonic for the suppression of spurious reflections. In a last step, with the information from the previous steps, a final set of harmonics is defined and applied. Results generated using spectral NRBC with a reduced set of harmonics are compared with results generated using other NRBC.

4.4.1 Definition of Fundamental Frequencies

The frequencies included in the spectral NRBC are defined as harmonics of the base frequency. For the current test case, the base frequency is specified as the quarter wheel

Table 4.2: Fundamental frequencies and their harmonics.

Fundamental frequency	Harmonics of the base frequency
Mean flow	0
Quarter wheel passing frequency	1, 2, 3, 4, 5, 6, 7, 8, 9, 10, ...
S_1 vane passing frequency (VPF_1)	9, 18, 27, 36, 45, 54, 63, 72, 81, 90, ...
R_2 blade passing frequency (BPF_2)	7, 14, 21, 28, 35, 42, 49, 56, 63, 70, ...
S_2 vane passing frequency (VPF_2)	12, 24, 36, 48, 60, 72, 84, 96, 108, 120, ...

passing frequency, which is 848 Hz.
The zeroth harmonic represents the mean flow and must be included in every setup. Another fundamental frequency is the quarter wheel passing frequency. The harmonics of this frequency are not expected to contain any strong unsteady fluctuations. However, including them in the setup may take into account hard to predict unsteady effects, e.g. perturbations caused by scatter modes.
The main unsteady effects in the flow field are caused by blade and vane interactions. Therefore, the blade passing frequencies are important for the representation of unsteady fluctuations. The seventh, ninth and twelfth harmonics of the base frequency correspond to the blade passing frequencies of each row. These are defined as fundamental frequencies. A summary of the fundamental frequencies and their harmonics is presented in Table 4.2.

4.4.2 Reduction of the Set of Harmonics

In this section, in addition to the base setup described in section 4.2, four setups are defined. Each of them uses spectral NRBC with different sets of harmonics. These sets consist of a fixed number of harmonics of the fundamental frequencies. The resulting sets

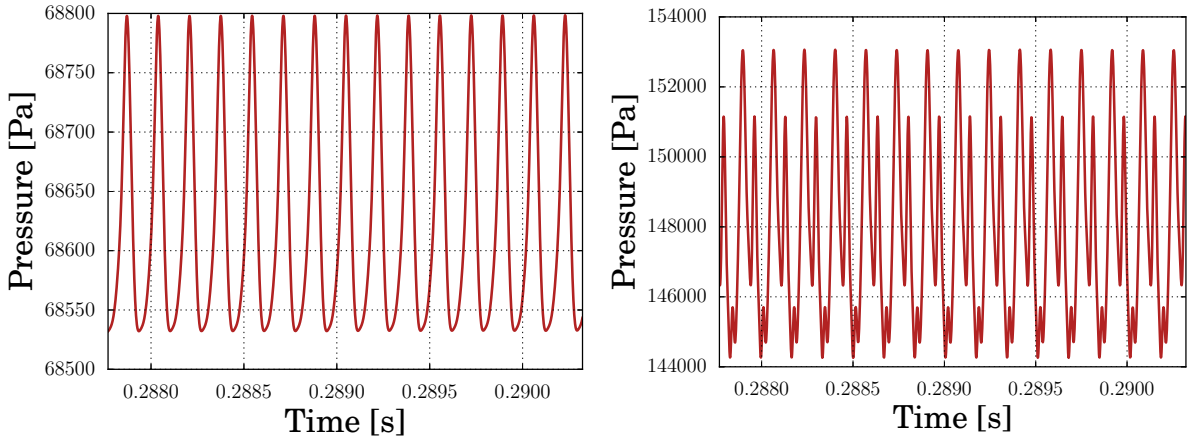

(a) Inlet boundary

(b) Outlet boundary

Figure 4.12: Probe of the instantaneous pressure.

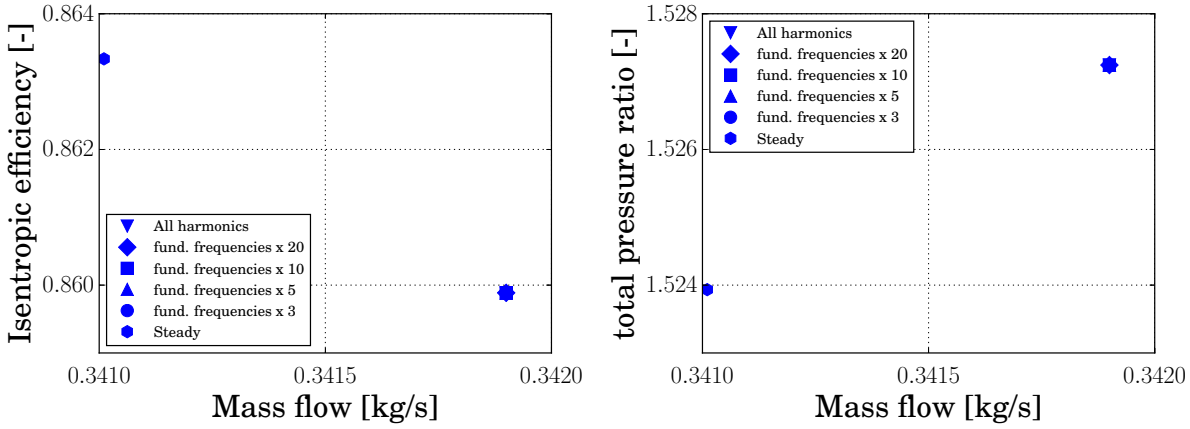

Figure 4.13: Total pressure ratio over the mass flow and isentropic efficiency over the mass flow for all sets of harmonics presented in Table 4.3.

are displayed in Table 4.3. Here, the names of the setups describe how many harmonics of the fundamental frequencies are included in the NRBC. For example, the set "fund. frequencies x 10" contains the first ten harmonics of the fundamental frequencies. The setup "All harmonics" corresponds to the base setup from section 4.2. It is the reference setup for this analysis.

As first step, the convergence of the simulations is checked. For that purpose, one probe is positioned at the outlet boundary and one is positioned at the inlet boundary. Figure 4.12 displays the instantaneous pressure over time at the probes. The plots show the last two simulated periods of the setup "All harmonics". The pressure shows no variations in its periodicity. Therefore, the solution is assumed to be fully converged. The runtime is identical for all setups simulated in the current chapter.

Figure 4.13 displays the isentropic efficiency and the total pressure ratio plotted over the mass flow at the inlet boundary. The reduction of the sets of harmonics yields no changes in isentropic efficiency, in total pressure ratio and in mass flow compared to "All

Table 4.3: Sets of harmonics included in the spectral NRBC for each setup.

Setup	Set of harmonics
All harmonics	{0 - 307}
fund. frequencies x 20	{0, 1, 2, 3, 4, 5, 6, 7, 8, 9, 10, 11, 12, 13, 14, 15, 16, 17, 18, 19, 20, 21, 24, 27, 28, 35, 36, 42 ,45, 48, 49, 54, 56, 60, 63, 70, 72, 77, 81, 84, 90, 91, 96, 98, 99, 105, 108, 112, 117, 119, 120, 126, 132, 133, 135, 140, 144, 153, 156, 162, 168, 171, 180, 192, 204, 216, 228, 240}
fund. frequencies x 10	{0, 1, 2, 3, 4, 5, 6, 7, 8, 9, 10, 12, 14, 18, 21, 24, 27, 28, 35, 36, 42 ,45, 48, 49, 54, 56, 60, 63, 70, 72, 81, 84, 90, 96, 108, 120}
fund. frequencies x 5	{0, 1, 2, 3, 4, 5, 7, 9, 12, 14, 18, 21, 24, 27, 28, 35, 36, 45, 48, 60}
fund. frequencies x 3	{0, 1, 2, 3, 7, 9, 12, 14, 18, 21, 24, 27, 36}

harmonics". Therefore, it does not change the operating point of the simulation. As reference for the operating point, a steady computation of the configuration is performed. Compared to the steady setup, the unsteady setup result in a 0.26% larger mass flow. The total pressure ratio decreases by 0.22% and the isentropic efficiency increases by 0.4%.
The variable used to assess the reflections in the solution is the instantaneous unsteady pressure at the start of a period. To efficiently capture the unsteady solution, TRACE stores Fourier coefficients of the latest period in each cell. With these coefficients, the flow solution at every time step can be reconstructed. As it was described in section 3.2, the zeroth temporal Fourier coefficient of the flow field represents the temporal average of the solution. The unsteady pressure is calculated by subtracting the zeroth Fourier coefficient of the pressure from the instantaneous pressure for each cell in the domain,

$$\tilde{p} = p - \bar{p} \quad with \quad \bar{p} \approx \hat{p}_{\omega=0}. \tag{4.3}$$

Figure 4.14 shows the distribution of the instantaneous relative Mach number and of the instantaneous unsteady pressure at the start of a period. Here, S_1 shows a supersonic area in the front section of the suction side, delimited by a shock. Further, the first half of R_2 is supersonic and contains two shocks, a detached shock at the leading edge of the blade and a shock in the blade passage. S_2 has only very small supersonic areas in the front section of the suction side of its vanes.
In S_1, the main source for unsteady pressure fluctuations is the leading edge shock of R_2. The unsteady waves resulting from the shock decay fast in S_1. Therefore, the unsteady pressure at the inlet boundary is small. The leading edge shock of R_2 is reflected at the vane of S_1. The reflected shock partly propagates downstream. This is the major source for unsteady pressure in R_2. Further, unsteady waves propagate upstream from the leading edge of S_2 into R_2. In S_2, the interaction between the R_2 wakes and the S_2 vanes, yield strong unsteady perturbations in the vane passage. Here, the maximum

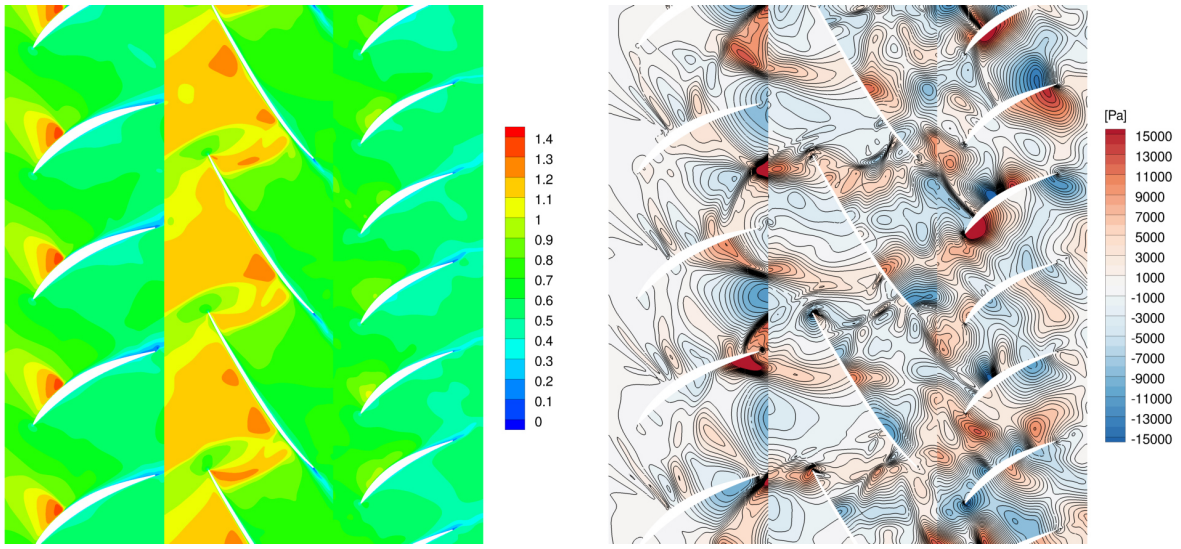

(a) Relative Mach number **(b)** Unsteady pressure

Figure 4.14: Distribution of the instantaneous relative Mach number and the instantaneous unsteady pressure in "All harmonics", at the start of a period.

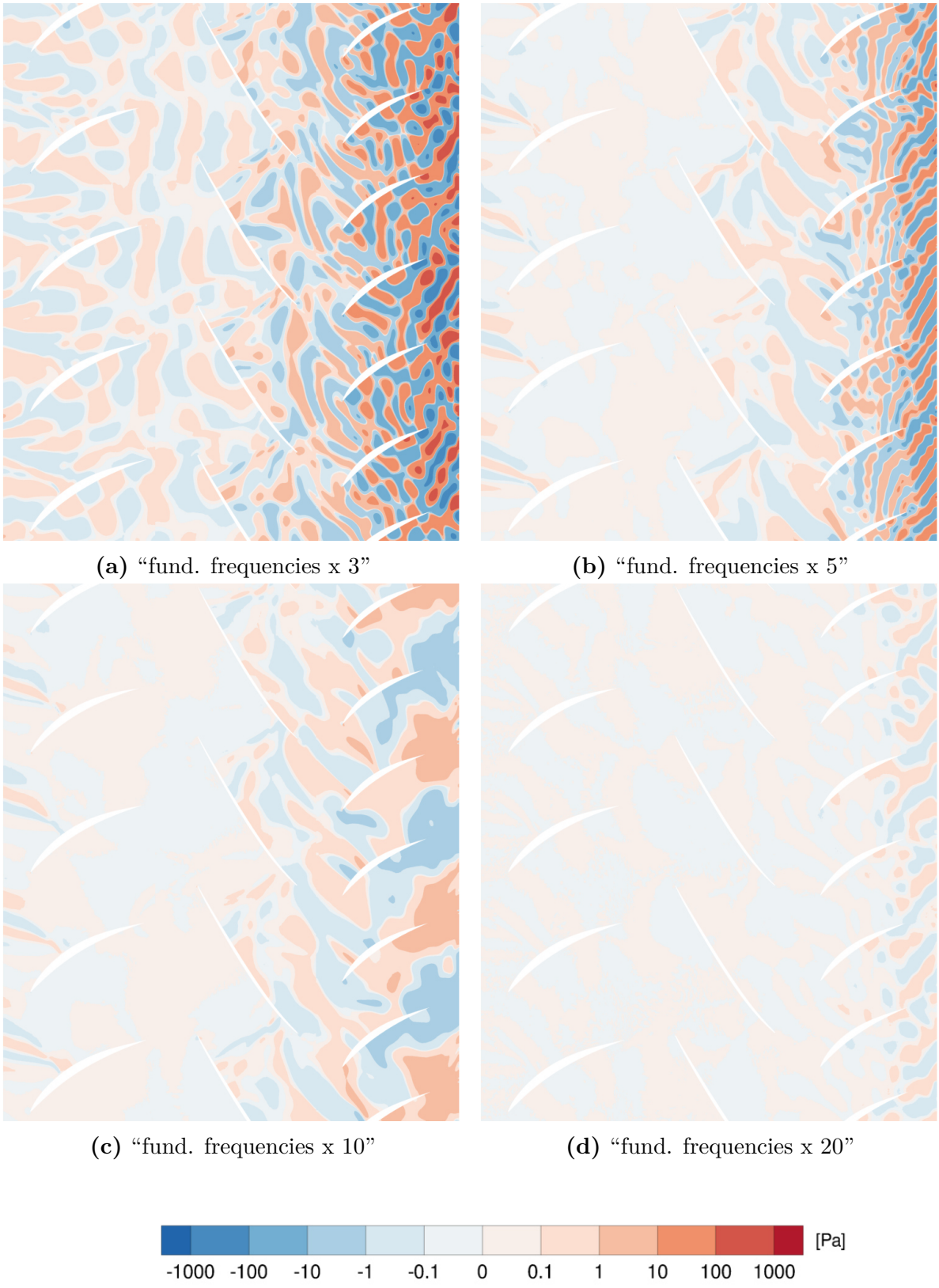

(a) "fund. frequencies x 3"

(b) "fund. frequencies x 5"

(c) "fund. frequencies x 10"

(d) "fund. frequencies x 20"

Figure 4.15: Differences in unsteady pressure between the solution of "All harmonics" and the solution of the other setups presented in Table 4.3, at the start of a period.

unsteady pressure of 39600 Pa is reached. These unsteady fluctuations weaken before reaching the outlet boundary.

Figure 4.15 displays, the differences in unsteady pressure between "All harmonics" and the other four setups presented in Table 4.3. The difference is calculated by subtracting the instantaneous unsteady pressure of each solution from the instantaneous unsteady pressure of the solution of "All harmonics".

As expected, reducing of the set of harmonics increases the amount of differences in the domain. At the inlet boundary, the differences in unsteady pressure stay below 1 Pa in all four setups. Even though these differences are very small, Figure 4.15 (a) shows that they can propagate into the entire domain. This implies that an insufficient non-reflecting behavior at the inlet boundary impacts the entire solution. If the number of harmonics is increased to five, the differences originating from the inlet do not propagate into the domain anymore. If the number of harmonics is increased to 20 harmonics of the fundamental frequencies, the differences at the inlet vanish completely.

At the outlet boundary the reflection induced unsteady fluctuations are significantly stronger than at the inlet boundary. For "fund. frequencies x 3", the maximum difference is 811 Pa, in "fund. frequencies x 5" it decreases to 360 Pa, in "fund. frequencies x 10" it drops to 29 Pa and in "fund. frequencies x 20" it the differences stay below 2 Pa. These maximum values are all located directly on the outlet boundary. These upstream running fluctuations decay fast and lose most of their energy before reaching the S_2 vane.

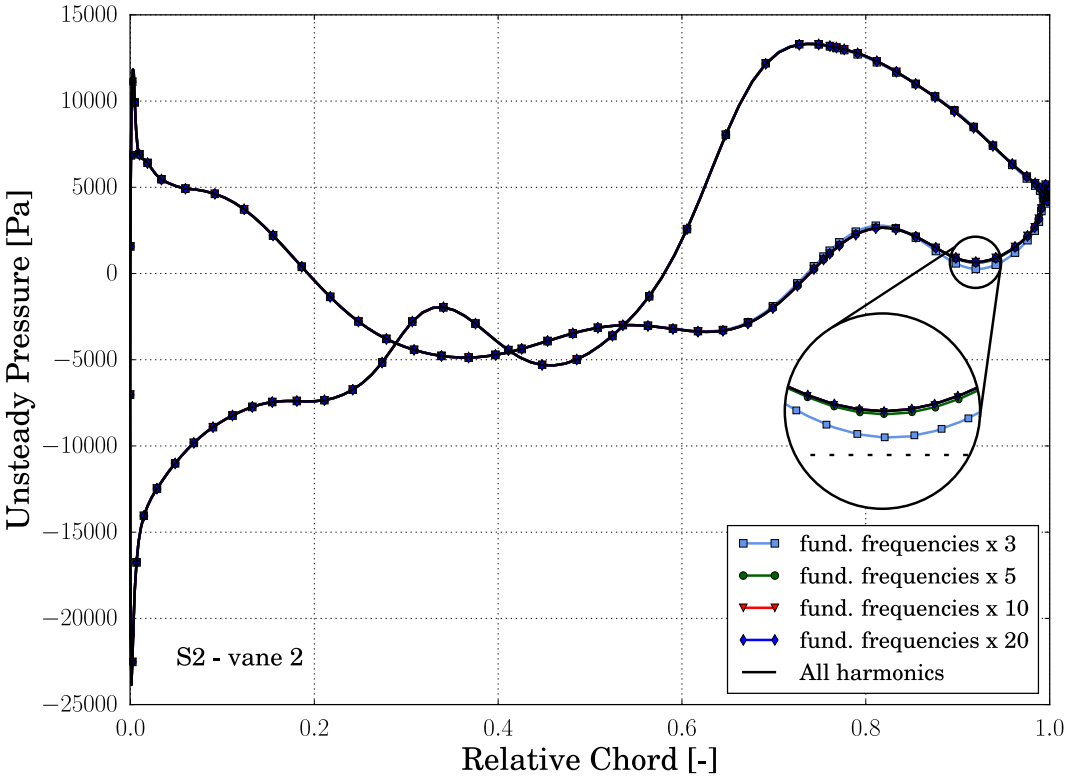

Figure 4.16: Distribution of the unsteady pressure on the second vane of S_2, at the start of a period.

Figure 4.15 (b) and (c) display that the upstream running waves are not able to pass R_2. The inlet in "fund. frequencies x 3" shows similar differences in unsteady pressure as the outlet in "fund. frequencies x 20". However, the upstream running waves originating from the outlet in "fund. frequencies x 20" vanish in the passage of S_2. This shows that, while in the current test case the reflections at the outlet show higher amplitudes, their impact on the domain seems more restricted by their upstream running character.

In the following, the unsteady pressure distribution on the blades and vanes of the different rows are analyzed. Since the unsteady pressure distribution varies in time, different blades show different temporal states of the unsteady pressure. Therefore, all blades must be considered during this analysis. However, in order to keep this section compact, plots in the current work focus on the blade with the highest local difference between the setups of Table 4.3.
In accordance to the previous results, in R_2 and in S_1, the impact of the reduced set of harmonics on the blades unsteady pressure distribution is very small. When using only three harmonics of the fundamental frequencies, in S_1, the highest local difference to "All harmonics" is 3 Pa. In R_2, the maximum difference increases to 6 Pa, because of the reflections originating from the outlet boundary. The maximum difference in S_1 does not decrease, when using 20 harmonics of the fundamental frequencies. In R_2, it decreases to 4 Pa.
Figure 4.16 displays the unsteady pressure distribution on the second vane of S_2. In contrast to S_1 and R_2, the reduction of the set of harmonics yields differences in the unsteady pressure distribution of the S_2 vanes. The differences are located in the rear section of the pressure side of the vane. The largest local difference in unsteady pressure between "All harmonics" and "fund. frequencies x 3" is 413 Pa. In "fund. frequencies x 5", it decreases to 49 Pa. For the other two setups, the maximum reflection induced differences are 8.4 Pa in "fund. frequencies x 10" and 4 Pa in "fund. frequencies x 20".
All simulations performed in this section show small differences in the unsteady pressure compared to the overall unsteady pressure distribution on the blades surface. It is shown in section 4.2, that reducing the number of harmonics in the spectral NRBC to 60 already leads to good computational costs compared with other NRBC. Therefore, the setup "fund. frequencies x 10", with 41 harmonics at each boundary, provides a good efficiency. Additionally, its impact on the solution on the blade surface is negligible. So, this is the main setup for the further procedure of the current analysis.

4.4.3 Single Frequency Analysis

In this section, the Fourier coefficients of the pressure are analyzed individually for each harmonic. This allows to recognize irrelevant harmonics that are still included in the sets of harmonics of "fund. frequencies x 10". Further, gaining a better understanding of the behavior of unsteady fluctuations at each harmonic, helps to predict relevant harmonics in other test cases.
In the following analysis, the relevance of each harmonic is evaluated using the amplitude of the complex Fourier coefficients of the pressure.

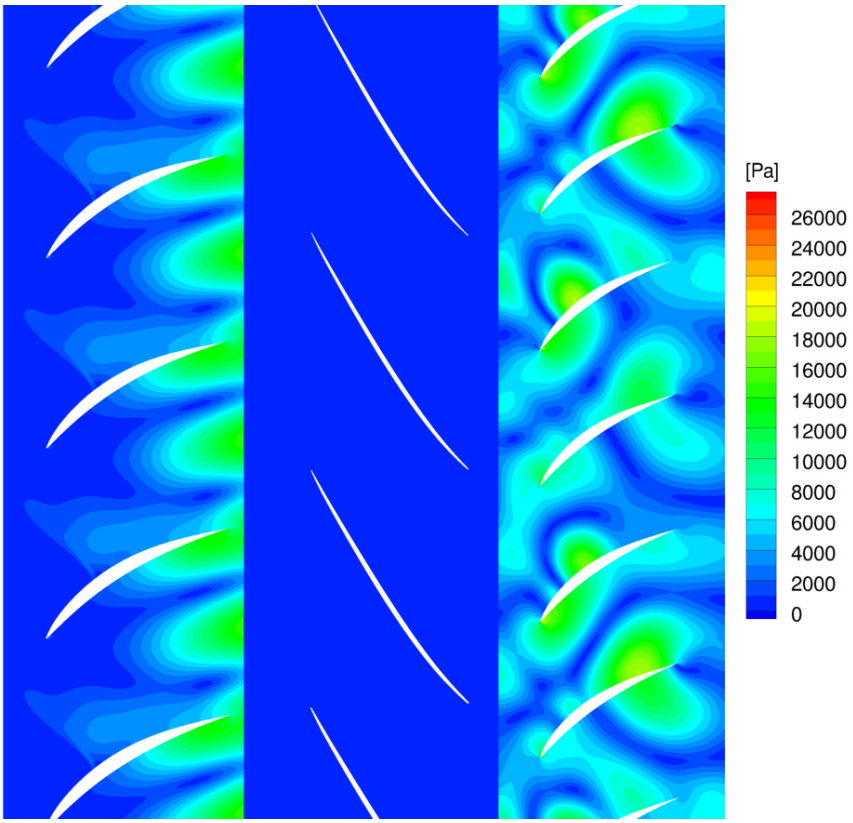

Figure 4.17: Amplitudes of the Fourier coefficients of the pressure at BPF_2 in the domain.

The first frequency to be analyzed is BPF_2, which corresponds to the seventh harmonic of the base frequency. Figure 4.17 shows the distribution of the amplitude of the seventh harmonic of pressure. The rotor creates strong unsteady waves in both stators. In R_2 itself, there are no unsteady pressure waves at BPF_2. In S_1 the strongest unsteady fluctu-

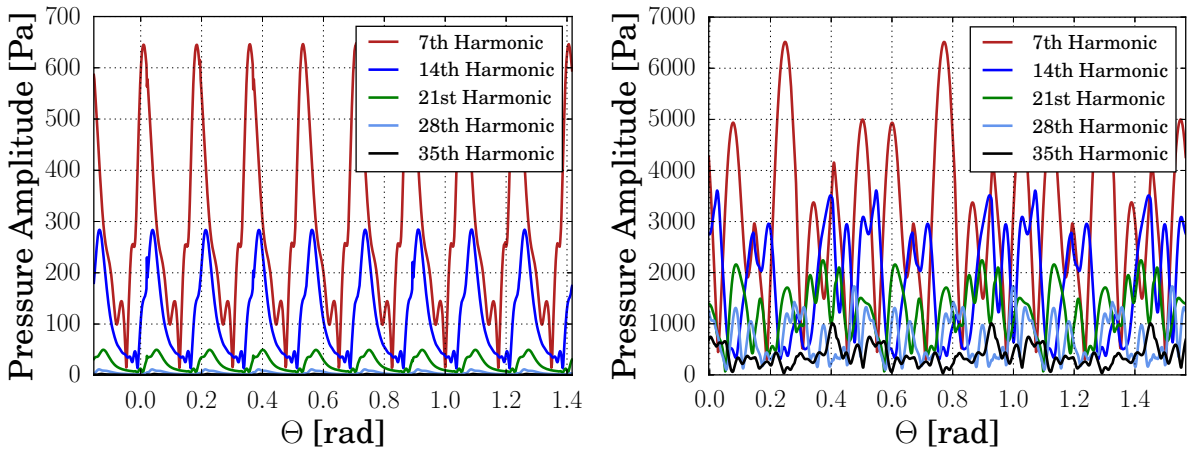

(a) Inlet boundary **(b)** Outlet boundary

Figure 4.18: Amplitudes of the Fourier coefficients of the pressure at the harmonics of BPF_2 at the boundaries.

ations are found at its interface to R_2, reaching amplitudes up to 14900 Pa. The unsteady waves propagating upstream decay fast. On the suction side of the vanes, the fluctuations are limited by the supersonic shock. Even though the rest of the channel remains subsonic, unsteady perturbations reaching the inlet boundary show very small amplitudes. The waves entering S_2 show smaller amplitudes than those entering S_1. When interacting with the vanes, the amplitudes of the unsteady waves increase up to 26700 Pa. This leads to overall stronger unsteady effects in S_2 than in S_1. The amplitudes of the unsteady waves decrease after the vanes and reach the outlet boundary with amplitudes smaller than 6600 Pa.

The behavior of unsteady fluctuations at frequencies corresponding to the higher harmonics of BPF_2 is very similar to that of the unsteady perturbations shown in Figure 4.17. At increasing frequencies, the amplitudes of the fluctuations entering the stators decrease. Further, the unsteady waves vanish after a shorter distance. Figure 4.18 shows the amplitude of the pressure along the inlet boundary and along the outlet boundary associated with the first five harmonics of BPF_2. In accordance to Figure 4.17, it shows that unsteady fluctuations are at least one order of magnitude larger at the outlet than at the inlet. Furthermore, the decrease in amplitude with increasing frequencies is stronger at the inlet boundary. The reason for that is that at higher harmonics the distance of propagation of the upstream running waves decreases more than for downstream running waves.

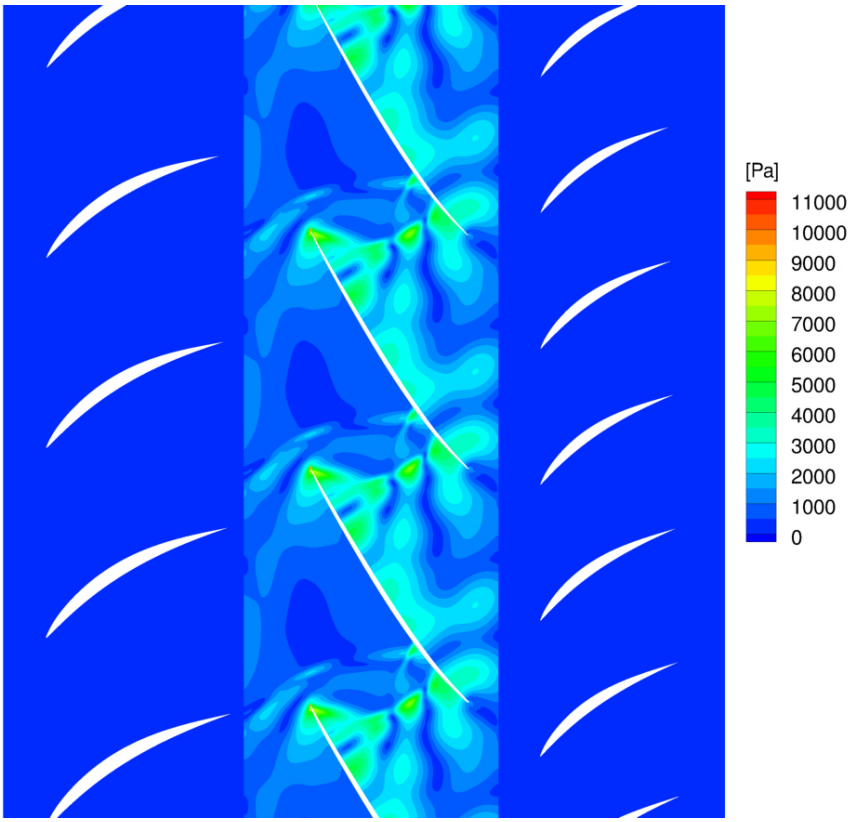

Figure 4.19: Amplitudes of the Fourier coefficients of the pressure at VPF_1 in the domain.

Figure 4.19 and Figure 4.20 display the amplitudes of the Fourier coefficient of the pressure at the frequencies VPF_1 and VPF_2, which correspond to the ninth and twelfth harmonics of the base frequency, respectively. At both harmonics, unsteady fluctuations occur only in R_2.
Perturbations at VPF_1 originate from S_1 and propagate downstream through R_2. When entering R_2, unsteady waves show amplitudes up to 1550 Pa. Around the leading edge of R_2 and around the passage shock they reach their maximum of 10475 Pa. Due to the wake induced unsteady lift, the fluctuations in VPF_1 are stronger in the rear section of R_2, leaving the rotor with amplitudes up to 2000 Pa.
Pressure fluctuations in the twelfth harmonic of the base frequency propagate upstream from S_2 to R_2. The highest amplitudes of up to 4250 Pa are located at the interface between R_2 and S_2. The unsteady waves vanish entirely before reaching the passage shock in R_2. Therefore, they are only present in the rear section of R_2. Overall the stator induced unsteady fluctuations are weaker than the rotor induced fluctuations.
Fluctuations associated with the higher harmonics of VPF_1 and VPF_2 show the same behavior as those at their respective fundamental frequency, but with decreasing amplitudes and propagation distance.

For harmonics which are not harmonics of VPF_1, BPF_2 or VPF_2 the amplitudes in the entire flow field are negligibly small. Solely, at the third harmonic of the base frequency

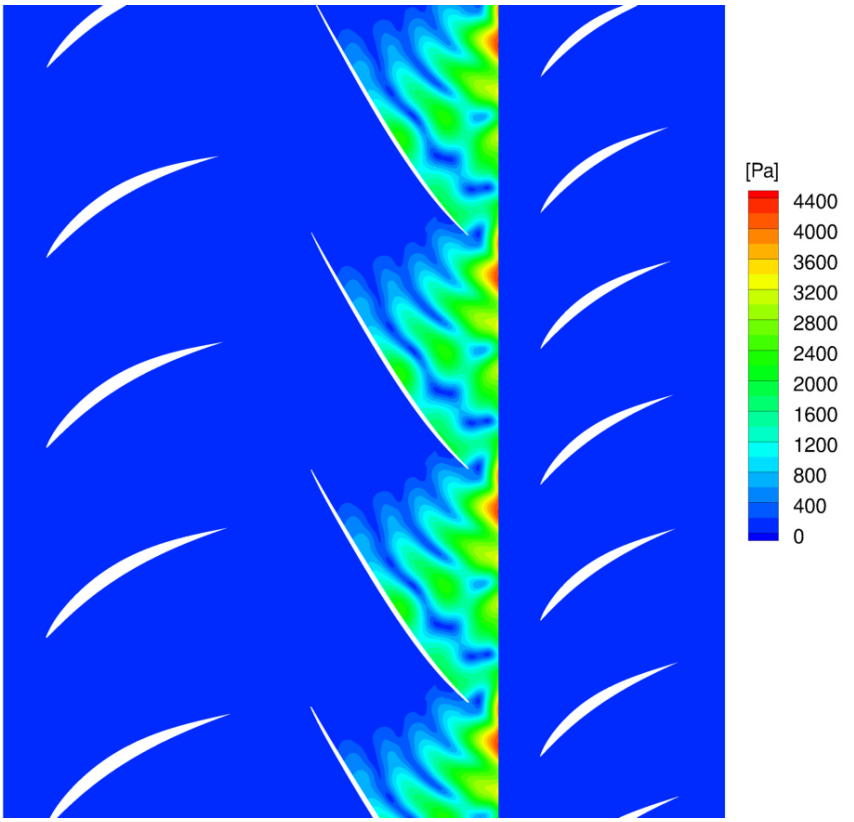

Figure 4.20: Amplitudes of the Fourier coefficients of the pressure at VPF_2 in the domain.

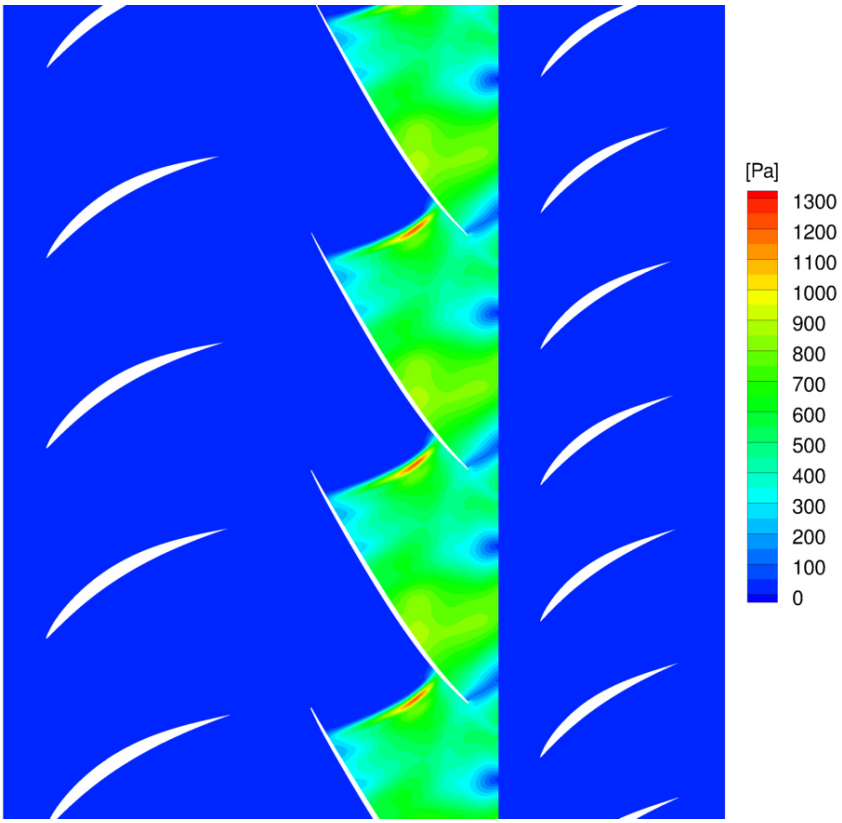

Figure 4.21: Amplitudes of the Fourier coefficients of the pressure at the third harmonic of the base frequency in the domain.

and at its higher harmonics unsteady fluctuations occur. Figure 4.21 shows the distribution of the pressure amplitude at the third harmonic of the base frequency. At this harmonic, the behavior of pressure fluctuations is very similar to that at VPF_2. The fluctuations are negligible in both stators and are present only in the rear section of R_2. This implies that these perturbations also originate from S_2. Here, the perturbations are unable to pass the channel shock in R_2. In contrast to VPF_2, the maximum amplitude of 1250 Pa is located around the channel shock and not at the interface to S_2. When increasing the frequency to the sixth harmonic of the base frequency, the maximum amplitude increases to 5660 Pa and shifts towards the interface between R_2 and S_2. The amplitude at this harmonic are of the same order of magnitude as at VPF_2. The development of the behavior of the unsteady perturbations associated with the harmonics of the third harmonic is not entirely clear because they often correspond to the harmonics of VPF_1 and VPF_2.

There are two possible sources for pressure fluctuations in the third harmonic. The first possibility is the non-linear interaction of waves fluctuating with VPF_1 and VPF_2. This results in a beat frequency corresponding to the third harmonic. The second and more probable possibility is that these unsteady waves result from an indexing effect. The wakes of S_1 are shredded in R_2 and continue to the vanes of S_2. Since S_1 and S_2 are in the same frame of reference, the shredded wakes always impinge on S_2 at the same location. Due to the blade count ratio of S_1 and S_2, this leads to a periodicity of the steady flow in S_2 every fourth vane. This periodicity is represented in Figure 4.22. Because of the interaction of the vanes of S_2 with this periodic flow, R_2 is subject to unsteady

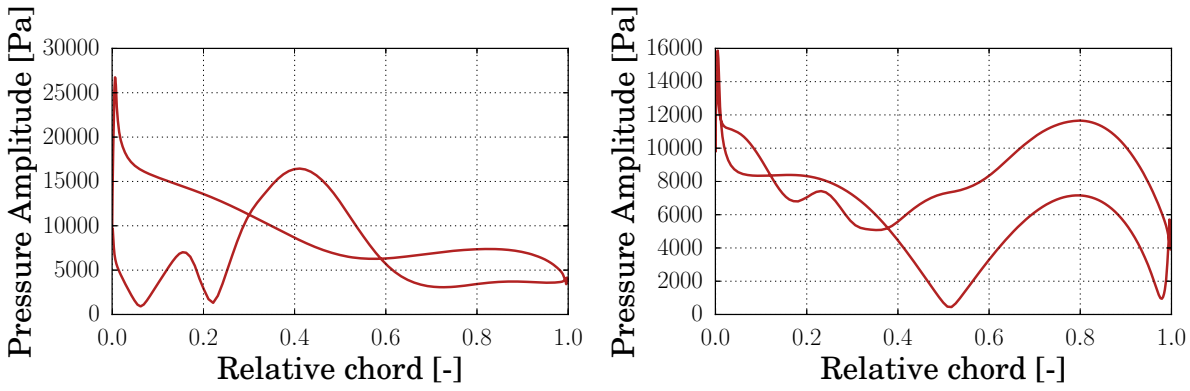

(a) Vane 1

(b) Vane 2

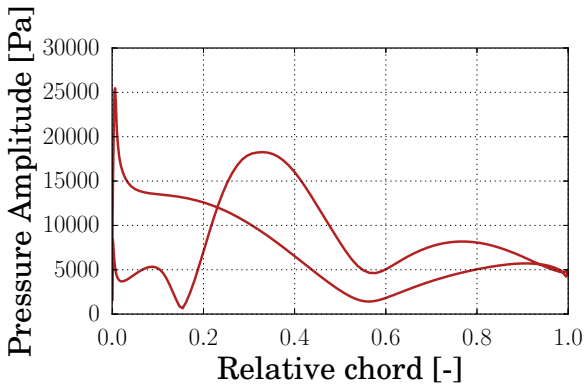

(c) Vane 3

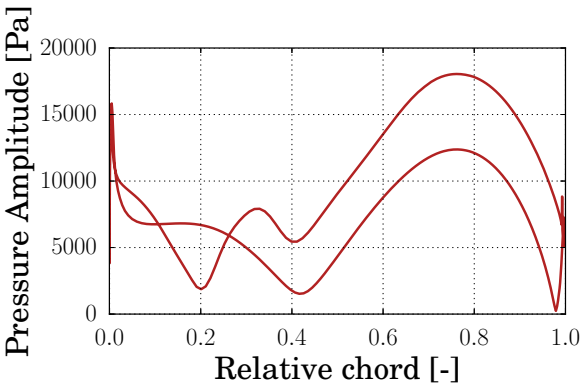

(d) Vane 4

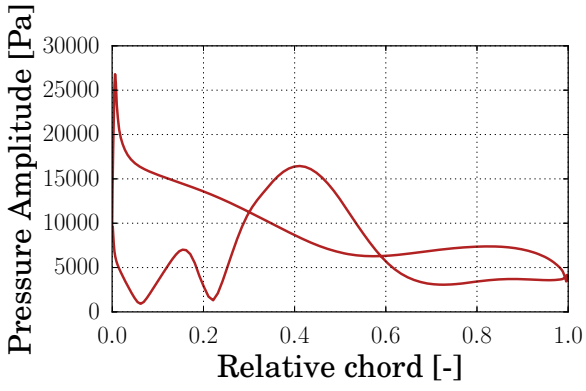

(e) Vane 5

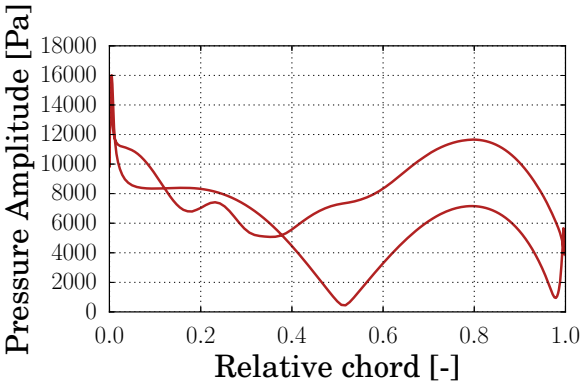

(f) Vane 6

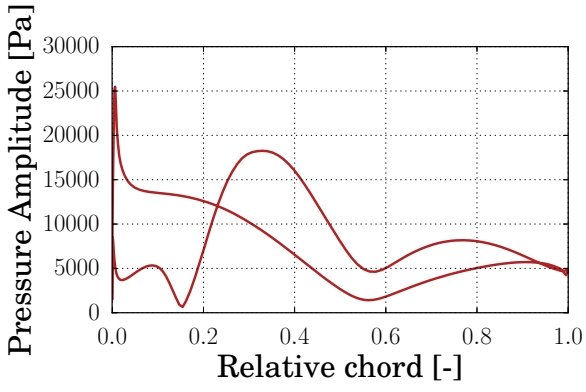

(g) Vane 7

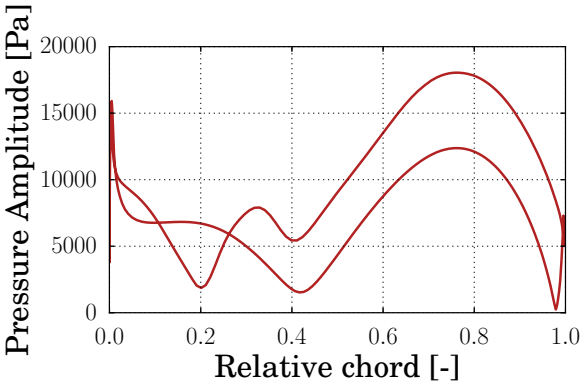

(h) Vane 8

Figure 4.22: Amplitude of the Fourier coefficients of the pressure at BPF_2 on the first eight vanes of S_2.

fluctuations at the frequency $VPF_2/4$. This frequency corresponds to the third harmonic of the base frequency. The third harmonic is defined as a new fundamental frequency, the indexing frequency.

In summary, this section shows that, for the current test case, the spectral NRBC only need to include harmonics of BPF_2. At all other fundamental frequencies and their harmonics, the pressure fluctuations are negligible in the rows adjacent to the boundaries. The amplitudes of the pressure fluctuation at the frequencies VPF_1, VPF_2 and at the indexing frequency on the boundaries are plotted in Figure 4.23. These frequencies correspond to the ninth, the twelfth and the third harmonics of the base frequency, respectively. These results are only applicable to a stator-rotor-stator configuration.

The results can be generalized to define a general concept, which is applicable to other configurations. The most important insight gained through this analysis is that unsteady fluctuations are only relevant at a boundary, if the row, where the fluctuation originates from, has a different rotational speed than the boundary. So, for single shaft configurations, if a rotor is adjacent to the boundary, only vane passing frequencies of the stators must be included in the set of harmonics and vice versa.
The indexing frequency must be included in the set of harmonics, if the configuration comprises two rows with corresponding rotational speed and one of these rows is not positioned at a boundary. So, for single shaft configurations, at least four rows are needed for the indexing frequency to be relevant at the boundaries. In two row configurations, there cannot be any rotor-rotor or stator-stator interactions. When simulating three rows, an indexing effect can be observed. But, it only yields unsteady fluctuations in the center row. If a fourth row is added, the fluctuations induced by the indexing effect of the first row on the third row yields unsteady fluctuations in the fourth row. These can be reflected at the boundary. Similarly to the blade passing frequencies, unsteady fluctuations at the indexing frequency and its harmonics are only relevant at boundaries adjacent to stators, if they result from a rotor-rotor interaction and vice-versa.

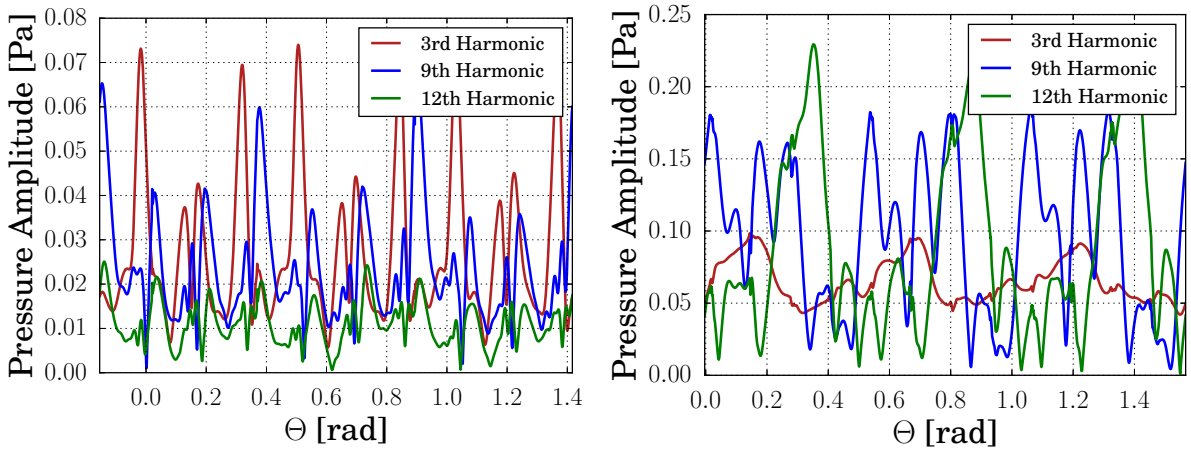

(a) Inlet boundary

(b) Outlet boundary

Figure 4.23: Amplitudes of the Fourier coefficients of the pressure at the ninth harmonic (VPF_1), at the twelfth harmonic (VPF_2) and at the third harmonic (indexing frequency) at the boundaries.

4.4.4 Application of the Concept

Using the concept developed in the last section, the set of harmonics used in "fund. frequencies x 10" is reduced further. The new set is presented in Table 4.4. It contains only ten harmonics of BPF_2 and the zeroth harmonic. A simulation using the setup "R_2 x 10" is performed.

Table 4.4: Set of harmonics included in the NRBC for the final setup of Rig250.

Setup	Harmonic set
R_2 x 10	$\{0, 7, 14, 21, 28, 35, 42, 49, 56, 63, 70\}$

Figure 4.24, Figure 4.25 and Figure 4.26 show the unsteady pressure distribution on the ninth vane of S_1, on the third blade of R_2 and on the second blade of S_2 at the start of a period. In S_1, the maximum difference between "R_2 x 10" and "All harmonics" remains unchanged at 3 Pa. In R_2, the differences in unsteady pressure peak at two locations on each blade, at the front section of the suction side and at the rear section of the pressure side. These locations are circled in blue in Figure 4.25. The peaks lead to an increase

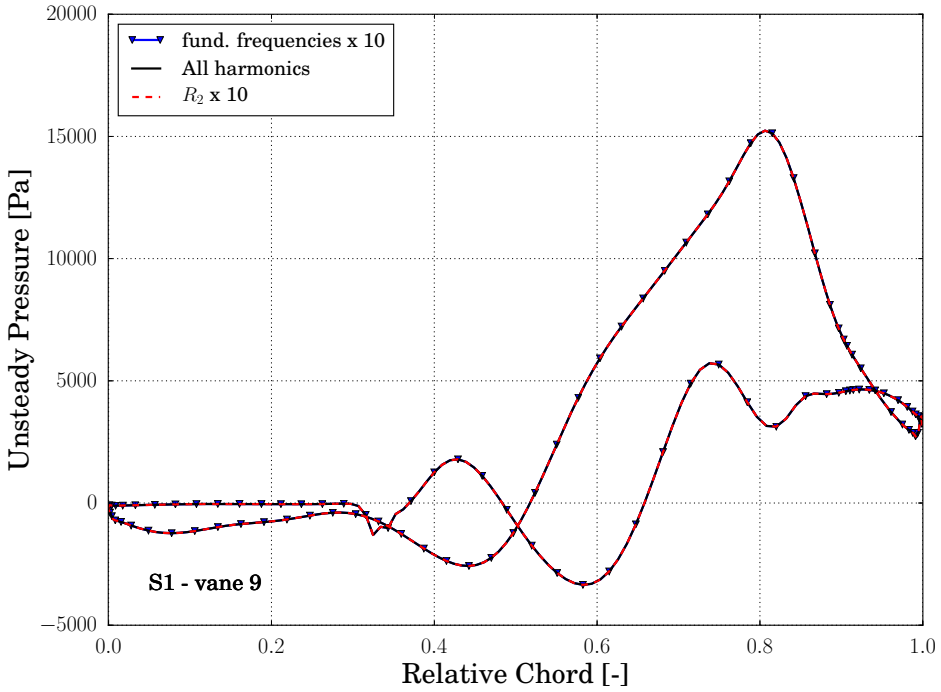

Figure 4.24: Comparison of the unsteady pressure distribution on the ninth vane in S_1 for the setups "All harmonics", "fund. frequencies x 10" and "R_2 x 10", at the start of a period.

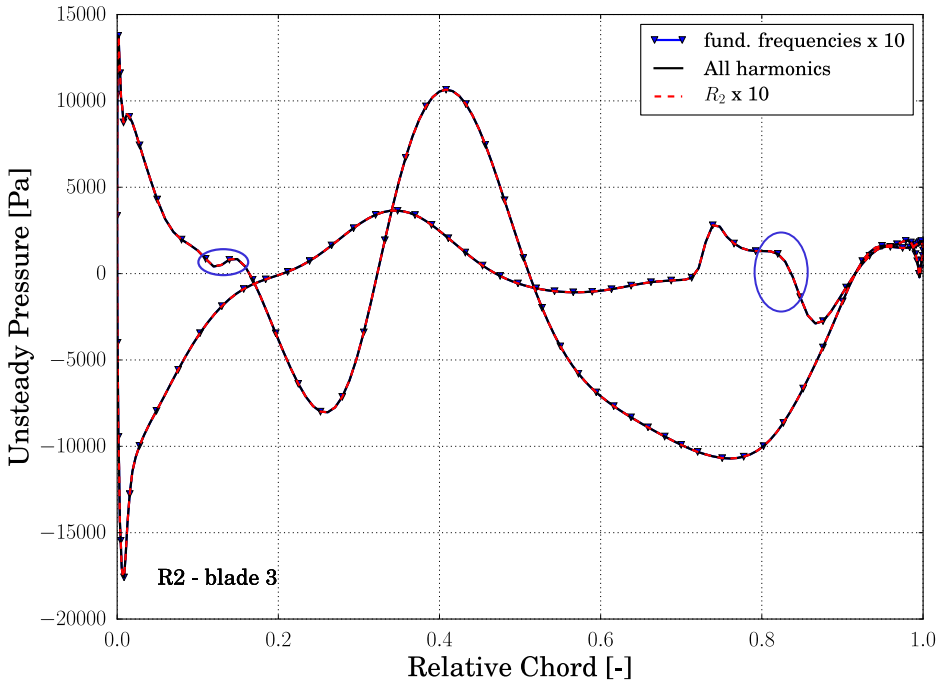

Figure 4.25: Comparison of the unsteady pressure distribution on the third blade in R_2 for the set ups "All harmonics", "fund. frequencies x 10" and "R_2 x 10", at the start of a period.

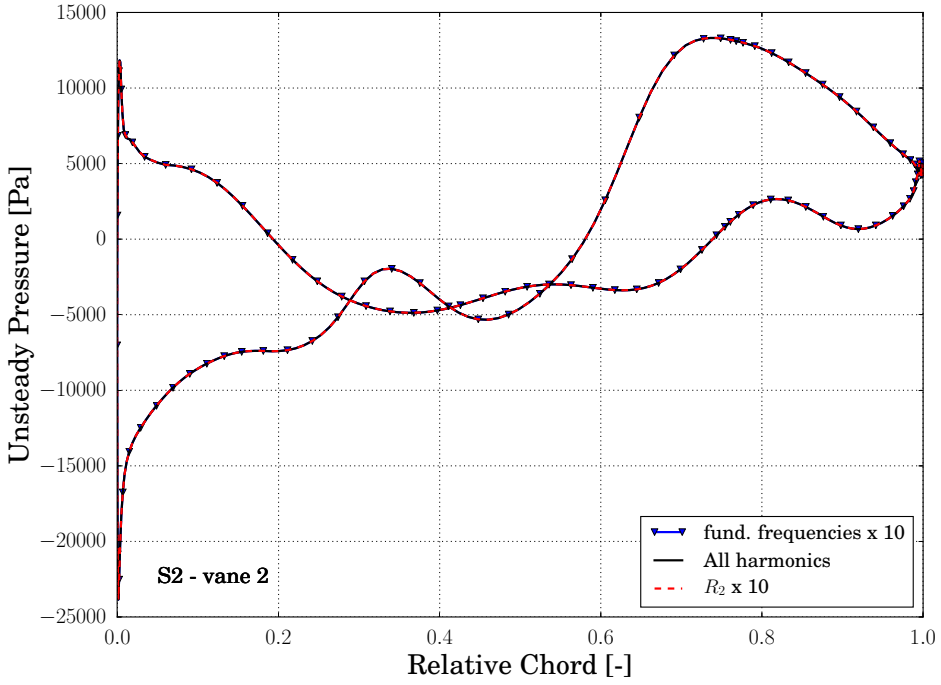

Figure 4.26: Comparison of the unsteady pressure distribution on the second vane in S_2 for the setups "All harmonics", "fund. frequencies x 10" and "R_2 x 10", at the start of a period.

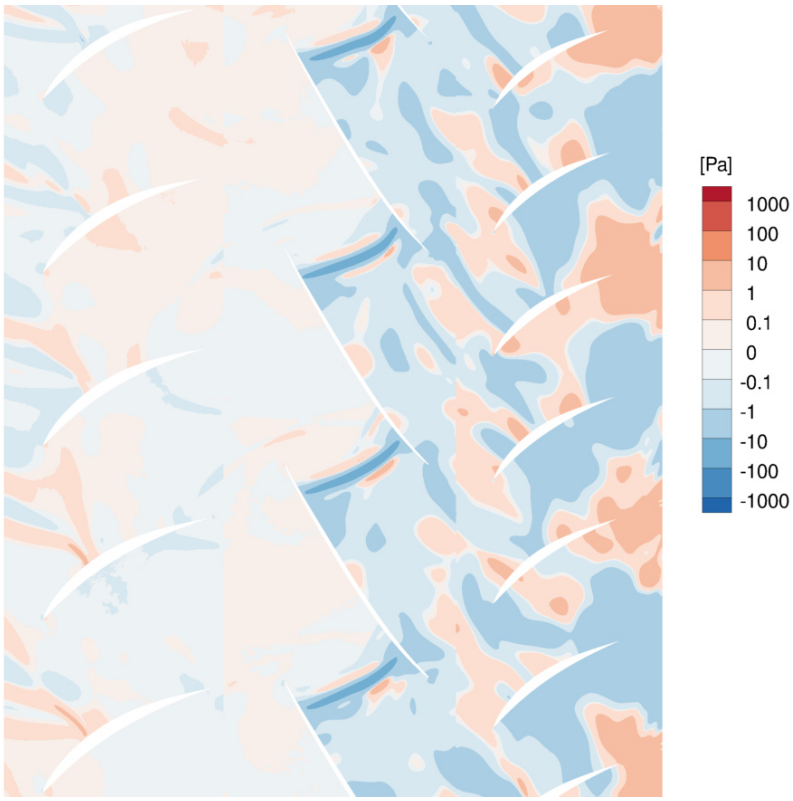

Figure 4.27: Difference in unsteady Pressure between "All harmonics" and "R_2 x 10", at the start of a period.

of the maximum difference in R_2, from 6 Pa to 15 Pa. In S_2, the maximum differences between "R_2 x 10" and "All harmonics" increases from 8.4 Pa to 14 Pa.

Figure 4.27 shows the difference in unsteady pressure between "R_2 x 10" and "All harmonics". Compared to "fund. frequencies x 10", the reflections increase slightly around the inlet boundary. They remain unable to propagate further into the domain. In R_2, the difference in unsteady pressure increases around the passage shock. At the center of the shock the difference increases up to 21 Pa. This interaction explains the two peaks observed on the blade of R_2. The overall reflected fluctuations originating from the outlet also increase slightly and reach a local maximum of 41 Pa.
Overall, the differences resulting from the reduction of the set of harmonics from "All harmonics" to "R_2 x 10" are small.

For Figure 4.28, the test case is simulated using the various NRBC presented in section 3.3 and the resulting operating points are plotted. It shows that reducing the set of harmonics from "All harmonics" to "R_2 x 10" does not change the operating point. Using 1D unsteady NRBC or approximate NRBC leads to a decrease of the mass flow by 0.4%. Using 2D Steady NRBC leads to a reduction of the isentropic efficiency by 0.4% and a reduction of the total pressure ratio by 0.196%. Since those differences are small, the same operating point is computed with all NRBC.
The impact of using different NRBC on the solution of the test cases becomes clearer, when looking at the at the unsteady pressure distribution on the blades. Figure 4.29, Figure 4.30 and Figure 4.31 show the unsteady pressure distribution in each row for dif-

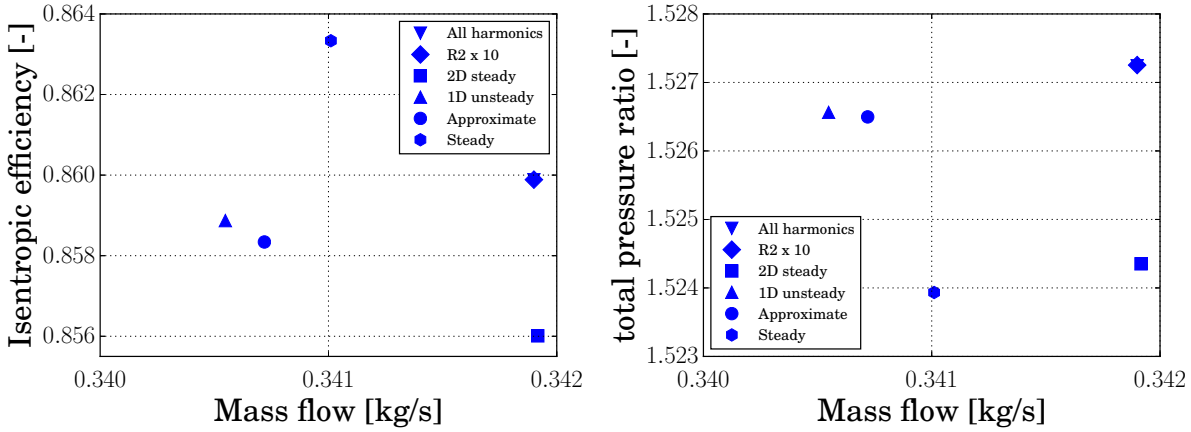

Figure 4.28: Total pressure ratio over the mass flow and isentropic efficiency over the mass flow for various NRBC.

ferent NRBC. It is shown in Figure 4.15 that the reflection induced unsteady fluctuations in S_1 are smaller than in S_2. Therefore, on the ninth vane of S_1, all solutions show similar unsteady pressure distributions. Solely, the distribution of 1D unsteady NRBC differs from the others. In R_2, the discrepancy between the different NRBC increases. Again, the result from the 1D unsteady NRBC show large differences to the other NRBC.

Reaching S_2, the reflected fluctuations are significantly stronger than at the front of the domain, leading to even larger differences between the various NRBC. Here, particularly the use of 2D steady NRBC results in stronger unsteady pressure fluctuations compared

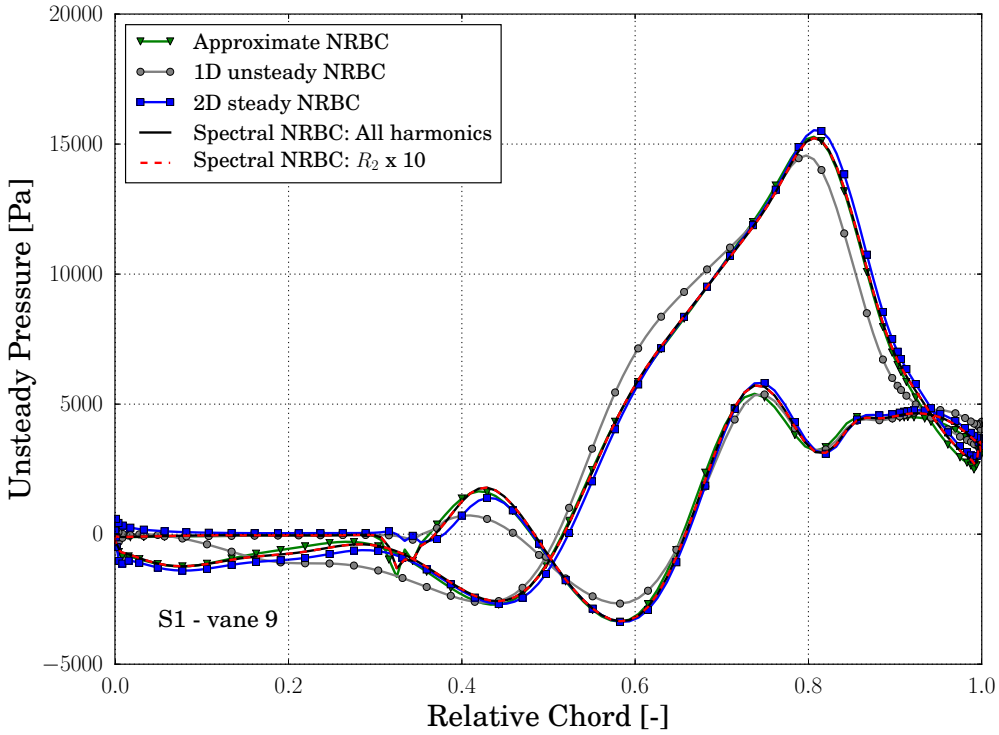

Figure 4.29: Comparison of the unsteady pressure distribution on the ninth vane in S_1 for different NRBC, at the start of a period.

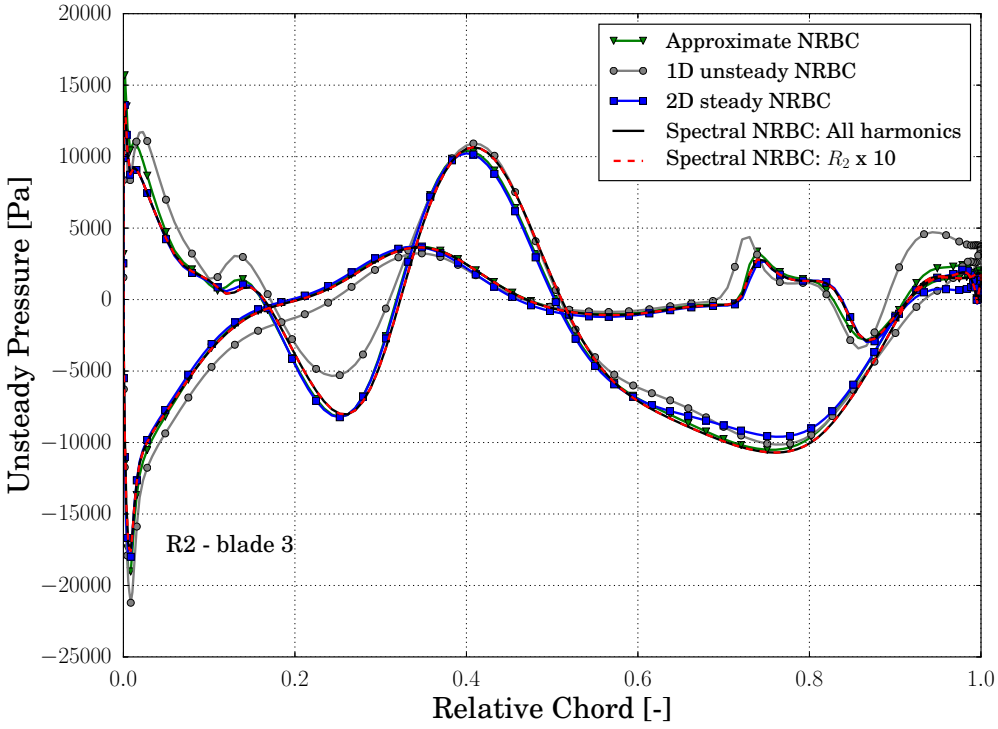

Figure 4.30: Comparison of the unsteady pressure distribution on the third blade in R_2 for different NRBC, at the start of a period.

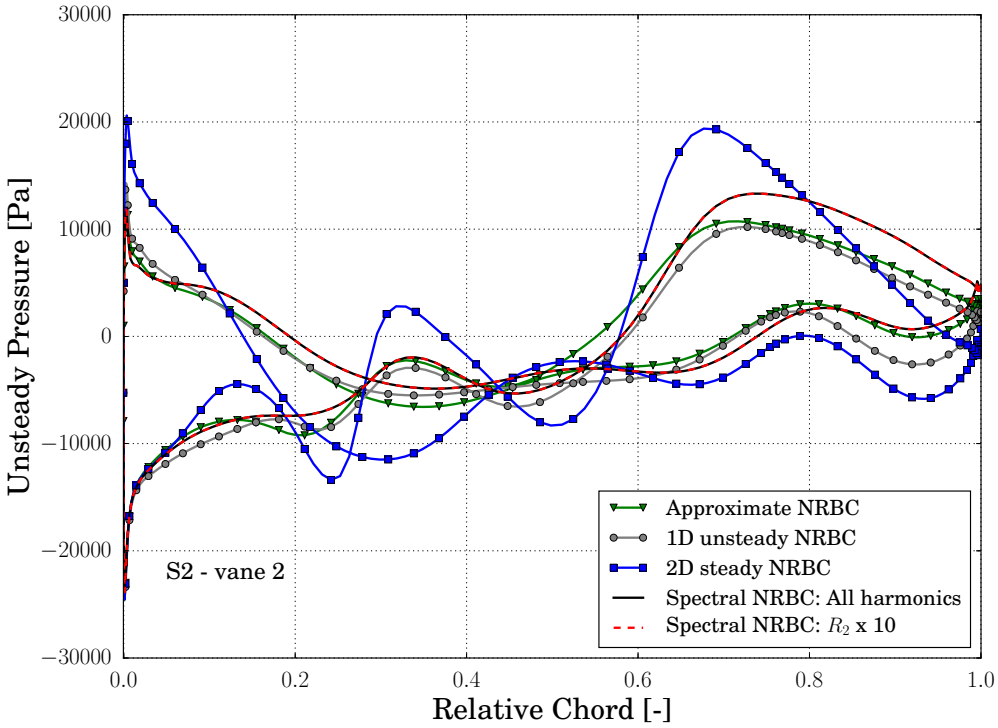

Figure 4.31: Comparison of the unsteady pressure distribution on the second vane in S_2 for different NRBC, at the start of a period.

with spectral NRBC.
Over the entire domain, using approximate NRBC yields the smallest differences compared to using spectral NRBC. Still, in S_2 the difference in unsteady pressure between the two NRBC reaches up to 7450 Pa. Compared to the results generated using other NRBC, the results of "R_2 x 10" are in a perfect agreement with the results of "All harmonics". This shows that reducing the set of harmonics of the spectral NRBC using the concept derived from section 4.4.3 does not impair the prediction accuracy of the spectral NRBC. From "fund. frequencies x 10" to "R_2 x 10" the number of harmonics is reduced from 41 to 11. The results of the performance analysis (section 4.2) show that the computational costs of the application of the spectral NRBC decrease linearly, when reducing the number of harmonics. Therefore, the computational costs for the application of the NRBC with 11 harmonics can be interpolated from the result of 20 and 5 harmonics. Compared to a full set of harmonics, the computational costs of the application of the boundary conditions decrease by 80.16%. For the average iteration loop, the costs decrease by 15.51%. Compared to the approximate boundary conditions, the spectral NRBC using the reduced set of harmonics are 1.24% slower during the iteration loop.

5 Durham Steam Turbine

In this chapter, the findings of chapter 4 are validated using a second test case. The chosen configuration is a three-dimensional low-pressure steam turbine stage. This test case is based on a generic blade design generated by Alstom Power in Rugby. The configuration was modified at the Durham University by Burton [4]. Qi et al. [22] present this turbine stage as an open test case for flutter analysis of steam turbines. All information about the test are obtainable on the website [6].
Qi et al. [22] define a long domain and a short domain for this turbine stage. While the long domain comprises a stator, a rotor and a diffuser, the short domain does not include the diffuser. In the current work, the short domain is chosen. In this domain, the outlet boundary of the rotor is only approximately 0.2 chord length away from the blades [22]. The proximity of the boundary to the rotor blades leads to oscillating trailing edge shocks impinging on the outlet boundary [27]. Therefore, the short domain represents a challenging test case for the NRBC.
The rotor blades are 0.92 m long, highly twisted, with a tip stagger angle of 67° at the tip. The rotational speed of the rotor is 3000 rpm [6]. The tip gap is 4.2 mm wide [27].
The blade counts of the stator and the rotor are 60 and 65 respectively. This allows to reduce the computational domain from a full wheel to a fifth wheel. This corresponds to 12 vanes in the stator and 13 blades in the rotor.
In section 5.1, the computational setup for the simulation of the turbine stage is described. In section 5.2, a reduced set of harmonics is defined for the spectral NRBC using the concept from chapter 4. The test case is simulated using spectral NRBC with the reduced set of harmonics as well as with a complete set of harmonics. Further, as a base for comparison, the turbine stage is computed using 1D unsteady NRBC, 2D steady NRBC and approximate NRBC. The analysis of the results starts with the description of the flow solution in the stage. Then, the operating points resulting from the different setups are compared. Finally, the impact of the reduced set of harmonics on the non-reflecting behavior at the boundaries is analyzed. In section 5.3, a fast method for the verification of the suitability of a set of harmonics is presented.

5.1 Computational Set-Up

For the current test case, the flow solver TRACE is used. A description of TRACE can be found in section 4.1.2. The spatial and temporal discretization methods used to compute the turbine stage correspond to those used for the Rig250.
The temporal resolution is 832 timesteps per period. This corresponds to 64 timesteps per rotor blade passage. At each timestep, 30 subiterations are performed. The CFL number is preset to 150. The computational mesh used to simulate the test case is generated at the DLR's institute for Propulsion Technology and has already been used by Schlüß and Frey [27] yielding good results. The mesh consists of 42,747,744 cells. This resolution is

finer than the initial mesh used by the KTH group [6, 27]. The configuration is split into 532 blocks and it is computed with 360 processes.
Petrie-Repar et al. [21] compared simulations of the turbine stage where the flow is modeled as wet-steam or as ideal gas. He showed that for a flutter analysis both models lead to equally good results. For the ideal gas model, the specific heat ratio of the gas is set to $\gamma = 1.12$, the ideal gas constant is set to $R = 461.52$ J/kgK and the dynamic viscosity is set to $\eta = 1.032 \times 10^{-5}$ Ns/m^2. These parameters remain constant in the entire stage. For the simulations performed in the current chapter, only the correct representation of the flow's characteristics is important. The correct prediction of the performance of the stage is only of secondary importance. Therefore, in the current work, the ideal gas model is employed.
The flow field in the turbine is assumed to be fully turbulent. The hub, the tip, the blades and the vanes, are computed as viscid walls. For the blades and vanes, a low Reynolds modeling approach is used for the turbulent boundary layer. For the hub and casing boundary layers, wall functions are used. At the circumferential limits of the domain, periodic boundaries are prescribed. At the inlet and outlet boundaries, NRBC are used. For the interface between the stator and the rotor, the same sliding grids are applied as for Rig250.
As inflow boundary values, radial distributions of the total pressure, of the total temperature and of the velocity angles are found on the website of the test case [6]. At the inlet, the average total pressure is 27000 Pa and the average total temperature is 340 K. For the definition of the outflow boundary, the boundary values of Schlüß and Frey [27] are used. They extracted a radial pressure profile at the rotor outlet from a steady simulation of the long domain. For this simulation, an average exit pressure of 8800 Pa with a radial equilibrium condition is imposed at midspan of the diffuser outlet. For unsteady computations, the solution is initialized using a precomputed steady solution.

5.2 Validation of the Concept

The rotor has a rotational speed of 3000 RPM. This yields a fifth wheel passing frequency of 250 Hz. A complete set of harmonics for the spectral NRBC is comprised of 332 harmonics. Following the concept derived from the analysis of Rig250, the set of harmonics is reduced. In this test case, the reduced sets are different at the inlet and at the outlet. At the stator inlet, the relevant harmonics are the harmonics of the blade passing frequency

Table 5.1: Sets of harmonics included in the spectral NRBC in the setups for the Durham Steam Turbine.

Setup	Set of harmonics
All harmonics	{0-331}
Reduced set	Inlet: {0, 13, 26, 39, 52, 65, 78, 91, 104, 117, 113}
	Outlet: {0, 12, 24, 36, 48, 60, 72, 84, 96, 108, 120}

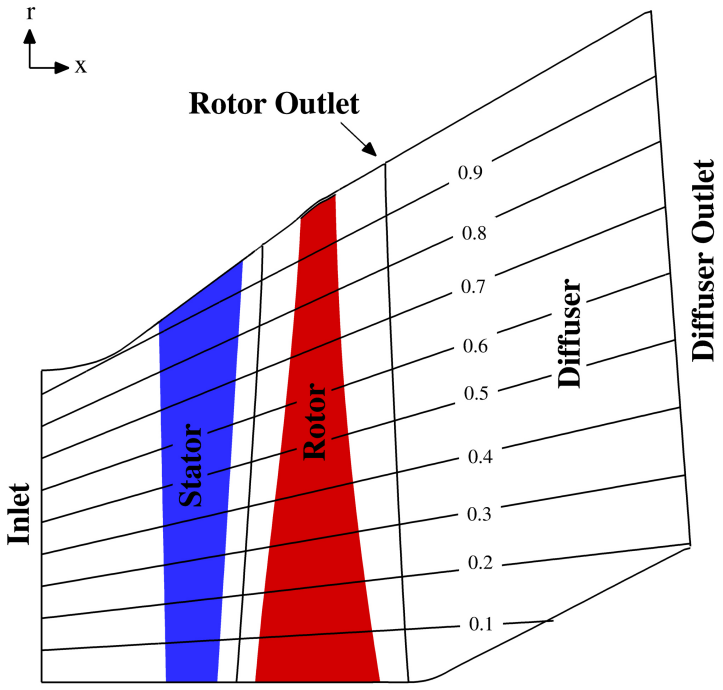

Figure 5.1: Schematic of the simplified definition of the relative span for the long domain of the Durham Steam Turbine stage [27].

of the rotor. At the rotor outlet, the relevant harmonics are the harmonics of the vane passing frequency of the stator. In this turbine stage, there is no indexing frequency since only two rows are simulated. The reduced sets of harmonics comprise ten harmonics of the relevant fundamental frequencies and the zeroth harmonic. This yields the sets of harmonics described in Table 5.1.
To simplify the comparison of results computed using different CFD solver, the KTH group presented a simplified definition for the relative span R_{rel} [6] given by

$$R_{rel} = \frac{r - 0.713}{0.576294\,(x + 1.102)}. \tag{5.1}$$

Figure 5.1 represents a schematic of the relative span distribution in the long domain. In the following sections, all plots of the turbine stage are plotted at constant relative span defined by equation (5.1). Instantaneous values are always plotted at the start of a period.

Figure 5.2 displays the density gradient magnitude and the unsteady pressure distribution in the flow for the setup "All harmonics" at 30%, 60% and 90% span. Here, the density gradient magnitude is dark for high values and bright if nearing zero. The transonic flow field in the stage leads to a complex system of shocks. In the vane passage of the stator, the flow is accelerated to $Ma > 1$. This leads to an expansion zone on the pressure side of the vane. The acceleration in the passage decreases with increasing relative span. Therefore, the intensity of the expansion also decreases with increasing span. At 30% and 60% relative span, the expansion zone ends with the trailing edge shock of the neighboring blade. At 90% relative span, the expansion zone is small and there is no pressure side

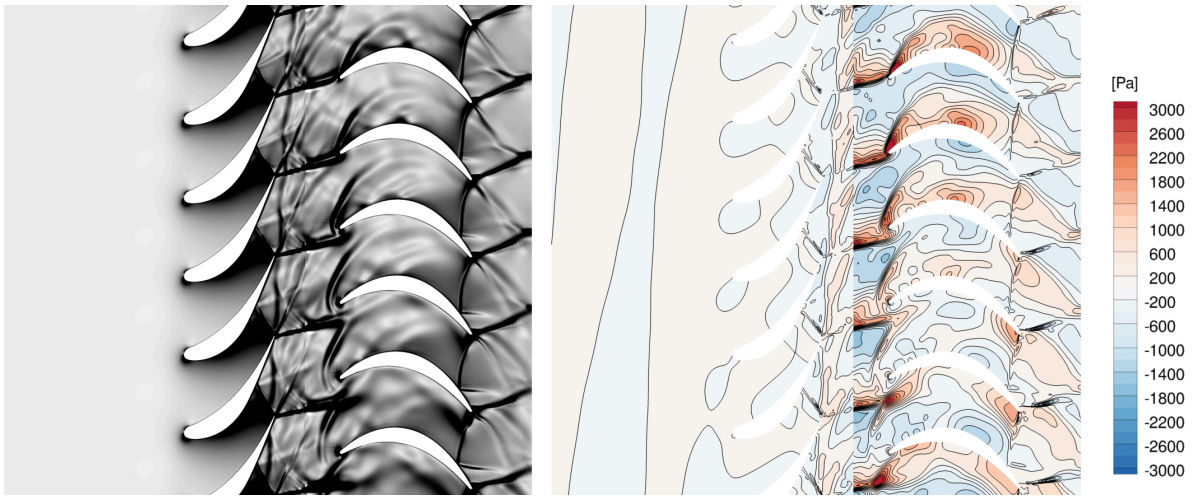

(a) Relative Span = 30%

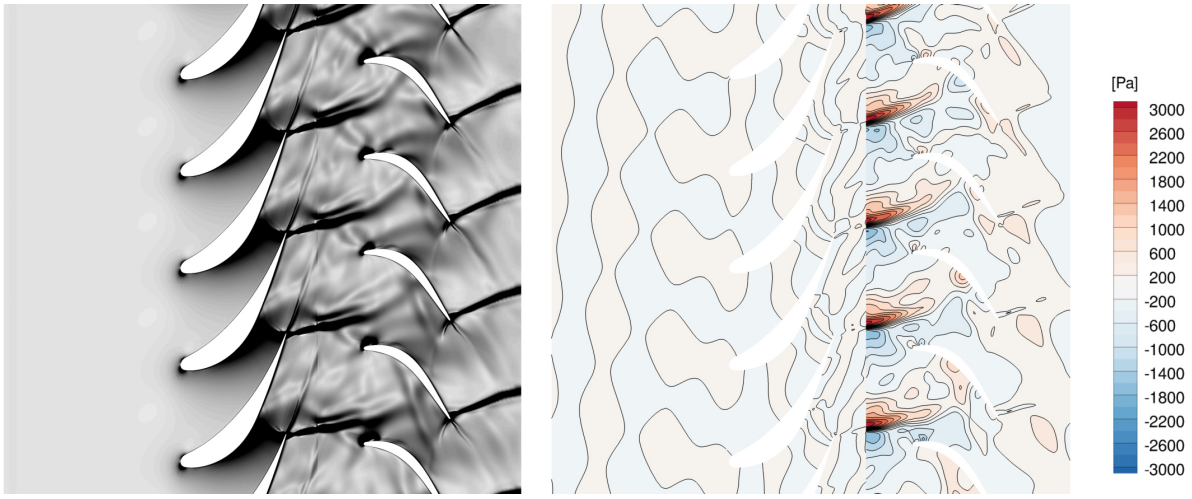

(b) Relative Span = 60%

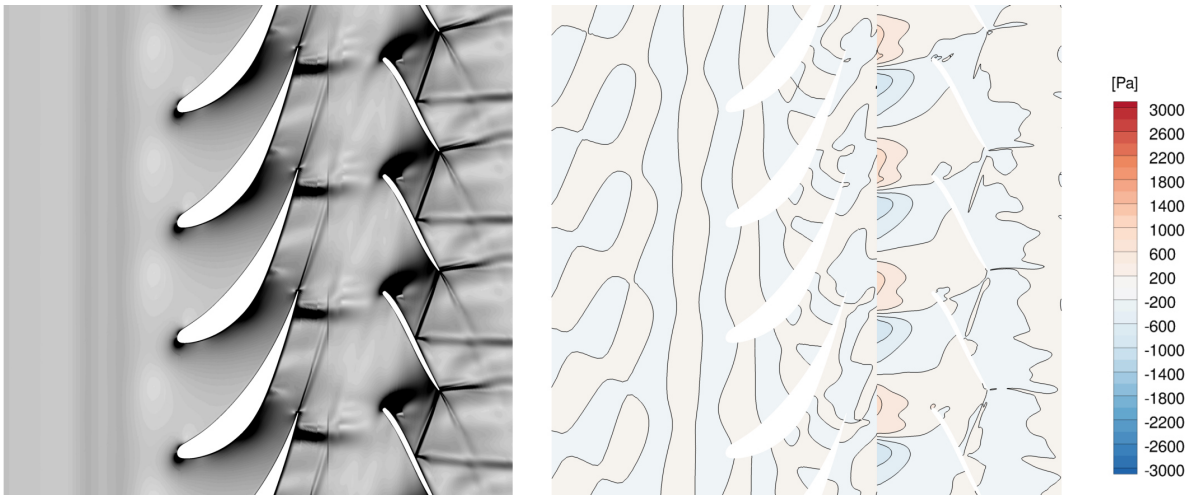

(c) Relative Span = 90%

Figure 5.2: Pseudo schlieren image and unsteady pressure distribution for the setup "All harmonics", at the start of a period.

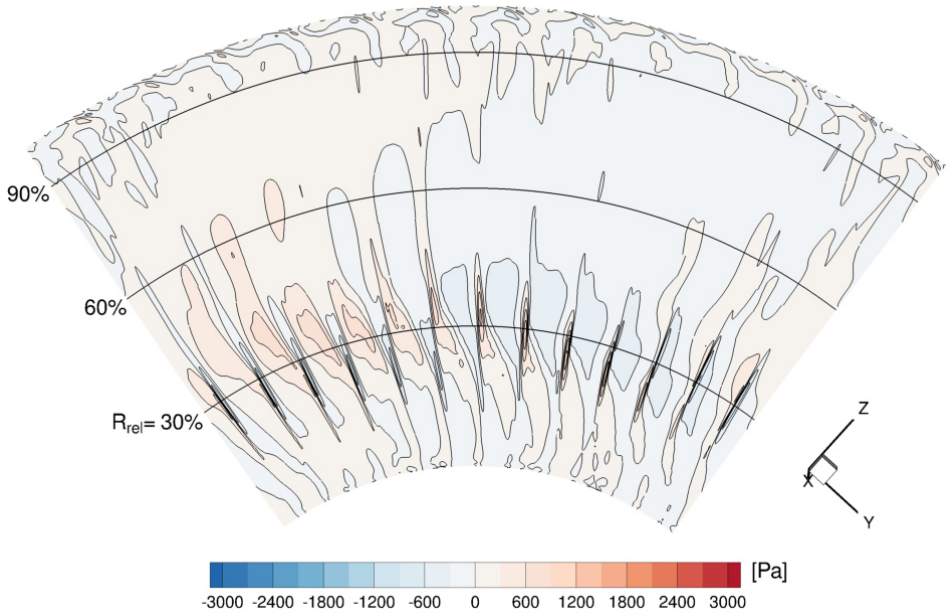

Figure 5.3: Unsteady pressure distribution at the outlet of the rotor, at the start of a period.

trailing edge shock. On the suction side of the trailing edge, a shock propagates towards the rotor, where it interacts with the rotor blades creating unsteady waves. This shock and its interaction with the rotor weakens with increasing span. At 90% relative span, the shock leaves the leading edge and moves onto the suction side of the vane. It does not reach the rotor blades anymore.
Entering the frame of reference of the rotor, the flow is subsonic. It is accelerated to $Ma > 1$ in the rotor passage. An expansion zone is located on the suction side of the leading edge. This zone becomes larger with increasing span. At the trailing edge of the blades there is a fish tail shock. The suction side branch of the shock impinges directly on the outlet boundary. The pressure side branch of the shock impinges on the neighboring blade first, before being reflected towards the outlet boundary. The pressure side branch of the shock is weak at 60% relative span.

The main source for unsteady pressure fluctuations in the flow is the trailing edge shock of the stator. In the frame of reference of the rotor, the shock is unsteady and interacts with the rotor blades. The strongest stator trailing edge shocks are located around 30% relative span. When hitting the rotor, strong upstream running unsteady waves are created. These unsteady waves decay fast. Therefore, the unsteady fluctuations are small at the inlet boundary. The stator rotor interaction also causes unsteady perturbations on the rotor blade, which propagate downstream to the outlet boundary. At 60% relative span, the interaction of the stator shock with the rotor is smaller than at 30% relative span. The stator-rotor interactions do not generate strong upstream running waves anymore. At 90% relative span, the stator shock has become too weak to reach the rotor. So, only weak unsteady fluctuations are present in the flow at this spanwise location.
Figure 5.3 shows the unsteady pressure distribution at the outlet of the stage. The strongest unsteady pressure waves reaching the boundary are located around 30% relative

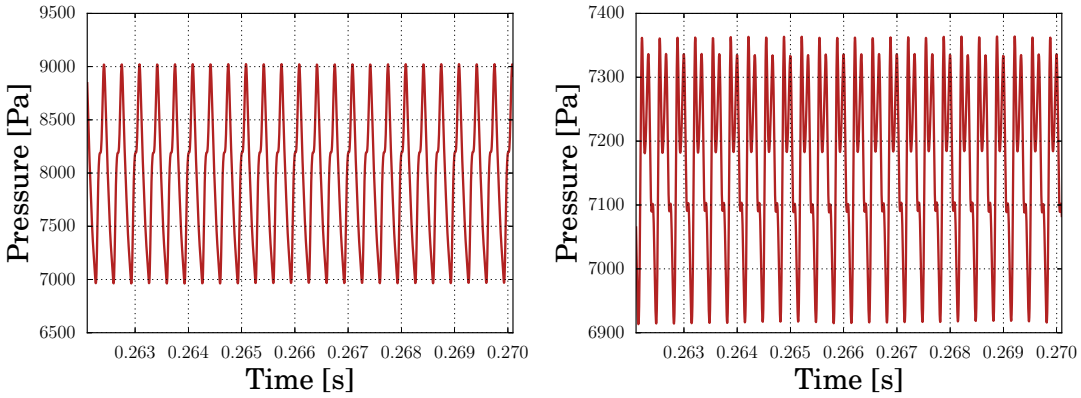

(a) Probe 7 **(b)** Probe 11

Figure 5.4: Probes of the instantaneous pressure at the outlet boundary of the turbine stage (see Figure 5.14).

span. The unsteady pressure at the entire inlet boundary is negligibly small.

Before analyzing the impact of the reduced set of harmonics on the prediction accuracy, the operating points of each setup are compared and the convergence of the simulations is checked. A single passage steady simulation is performed. This simulation is used as reference for the operating point. In the steady setup, a mixing plane is used as interface between the stator and the rotor. The setup using approximate NRBC is unstable and thus does not yield any usable results.
To check the convergence of the simulations, probes at the outlet of the domain are analyzed. The exact positions of the probes are presented later in Figure 5.14. Figure 5.4, displays the instantaneous pressure over time for the last period of "All harmonics". Here, the solution of the probes 7 and 11 at the outlet are represented. The plots display no variations of the periodicity of the pressure. Therefore, the solution is assumed to be fully converged. The runtime is identical for all setups simulated in the current chapter.
Figure 5.5 and Figure 5.6 display the temporal average of the pressure on the vane of the stator and on the blade of the rotor at 60% relative span. With $\bar{p} \approx p_{\omega=0}$, the temporal average of the pressure is given by the zeroth Fourier coefficient of the solution. Here, "Steady" corresponds to the steady setup.
On the stator vane, all setups yield corresponding pressure distribution until, at approximately 0.55 relative chord, the trailing edge shock of the neighboring vane impinges. Further downstream on the suction side, the pressure distribution is still identical for the unsteady setups. But, for the steady setup, the pressure distribution differs. This hints towards an unsteady rotor interaction, which is not resolved in the steady computation due to the mixing plane approach.
In the rotor, on the pressure side of the blade, the unsteady solutions are in a good agreement with the steady solution. On the suction side, there is a leading edge separation. In this area, the unsteady setups predict a higher pressure than the steady setup. Around 0.65 chord length, the trailing edge shock of the neighboring blade impinges on the suction side of the current vane. After that, the pressure stays approximately constant. In the area of constant pressure, the results from the setup using 1D unsteady NRBC differs from the other simulations.

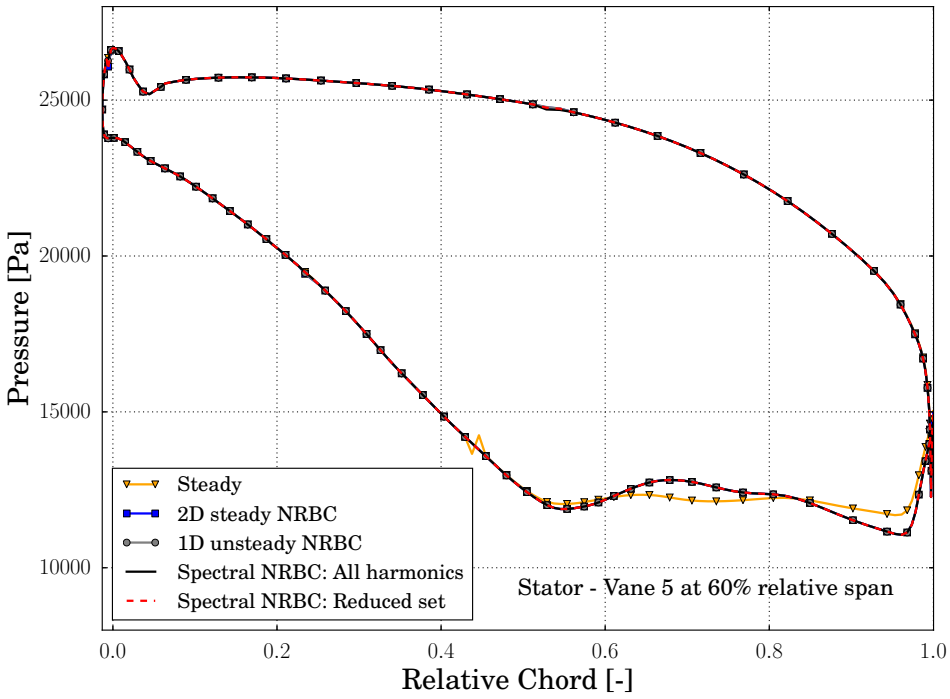

Figure 5.5: Comparison of the temporal average of the pressure $p_{\omega=0}$ for each unsteady setup with the pressure in the steady setup at 60% relative span on the fifth vane of the stator, at the start of a period.

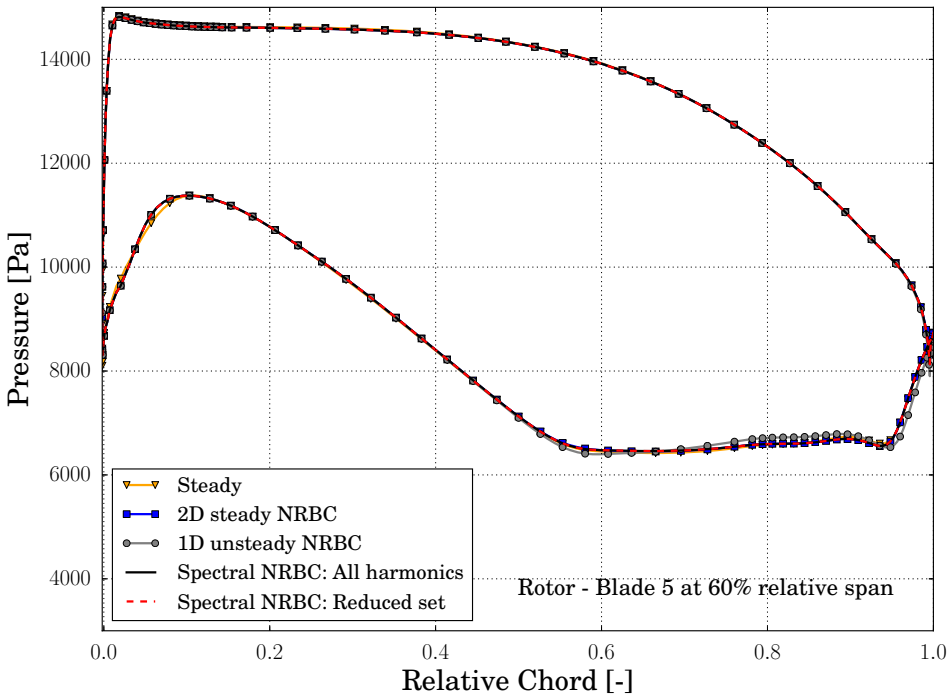

Figure 5.6: Comparison of the temporal average of the pressure $p_{\omega=0}$ for each unsteady setup with the pressure in the steady setup at 60% relative span on the fifth blade of the rotor, at the start of a period.

Table 5.2: Comparison of the mass flow and the total pressure ratio using different setups.

Setup	Mass flow [kg/s]	Total pressure ratio [-]
All harmonics	85.41	1.65138
Reduced set	85.41	1.65139
1D unsteady	85.41	1.65124
2D steady	85.41	1.65136
Steady	85.43	1.30253

Table 5.2 lists the mass flow and the total pressure ratio of the turbine stage for each setup. All setups predict the same mass flow. For the unsteady setups, the total pressure ratio only shows small variations. In comparison, the steady setup yields a significantly lower total pressure ratio. This is a result of using a mixing plane at the interface between the stator and the rotor. Mixing out the flow leads to additional mixing losses. These reduce the total pressure ratio of the stage.

Figure 5.7, Figure 5.8 and Figure 5.9 show the the unsteady pressure distribution on the second vane of the stator at 30%, 60% and 90% relative span. Here again, the unsteady fluctuations in the stator are very small and they decrease with increasing span. Therefore, no reflections occur at the inlet boundary. In the stator, all NRBC yield the exact same results.

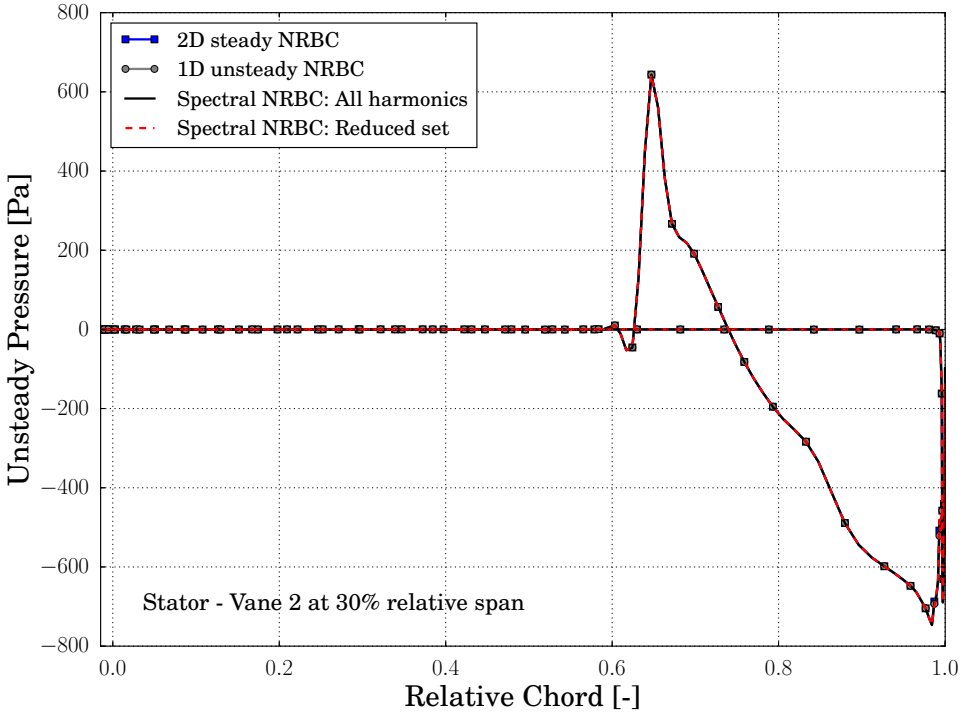

Figure 5.7: Comparison of the unsteady pressure distribution on the second vane of the stator at 30% relative span for different NRBC, at the start of a period.

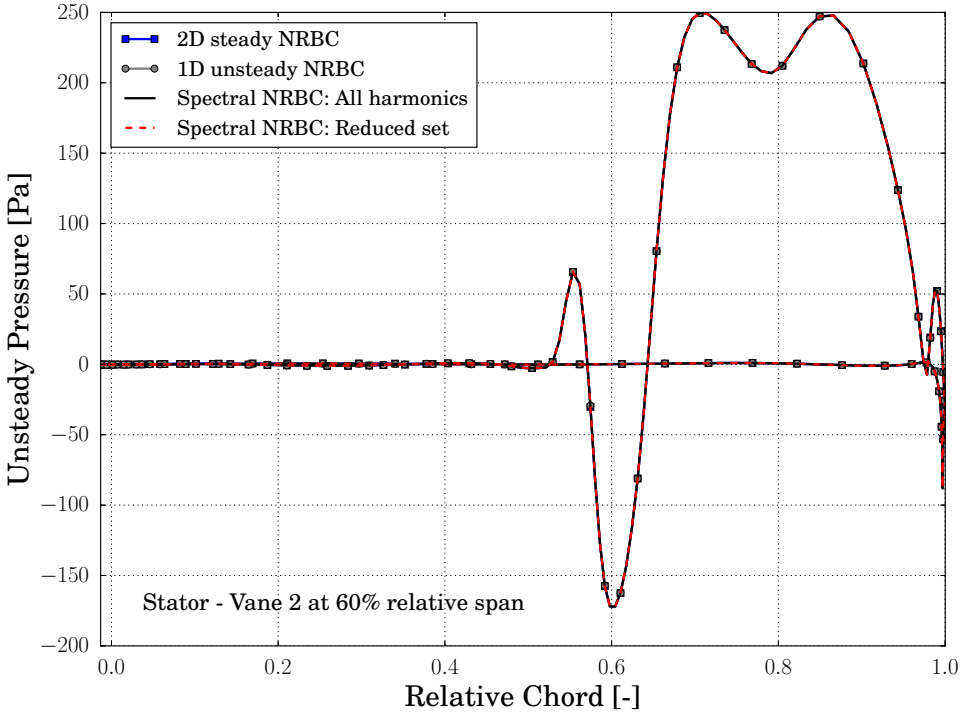

Figure 5.8: Comparison of the unsteady pressure distribution on the second vane of the stator at 60% relative span for different NRBC, at the start of a period.

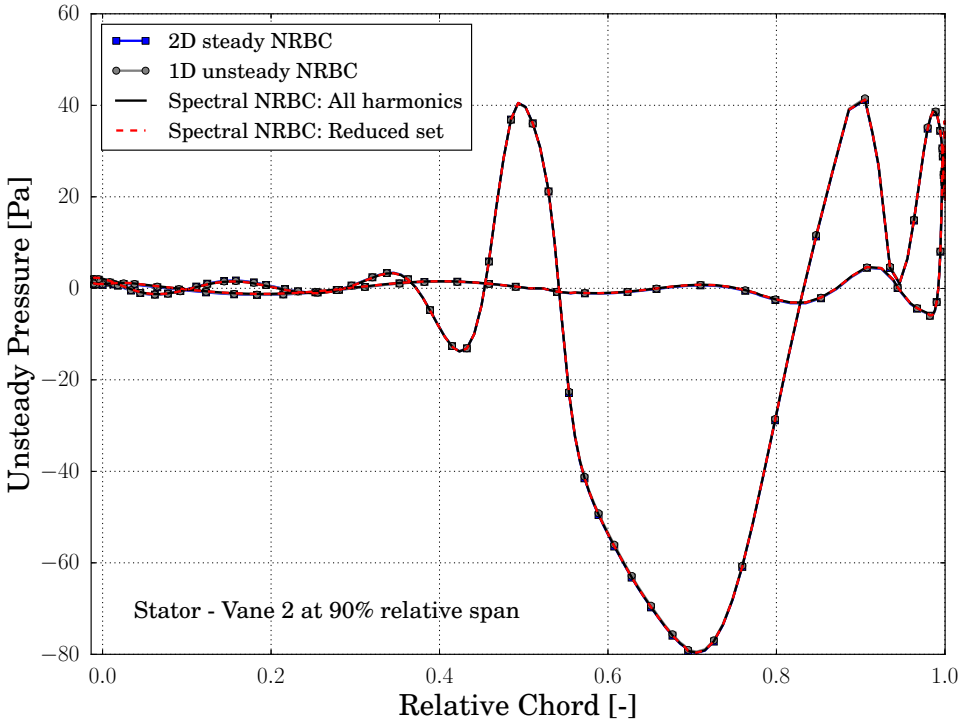

Figure 5.9: Comparison of the unsteady pressure distribution on the second vane of the stator at 90% relative span for different NRBC, at the start of a period.

Figure 5.10, Figure 5.11 and Figure 5.12 show the unsteady pressure on the tenth blade of the rotor at 30%, 60% and 90% relative span. On the pressure side of the blade, using different NRBC does not yield any differences in the solution. This is the case at all radial positions. On the suction side, all solutions yield corresponding results until the trailing edge shock of the neighboring blade impinges. At this point, the setups using 2D steady NRBC and 1D unsteady NRBC yield different unsteady pressure distributions than the spectral NRBC. This implies that unsteady reflections originating at the outlet cannot pass the pressure side branch of the trailing edge shock. At 90% relative span, the location where the shock of the neighboring blade impinges shifts toward the trailing edge of the blade when using 1D unsteady NRBC. At 30% relative span, the largest difference in unsteady pressure between the solutions generated with spectral NRBC and other NRBC is about 195 Pa. At 60% relative span, the difference decreases to 133 Pa and at 90% relative span, to 28 Pa, if the shift of the shock is ignored. In contrast, the largest difference in unsteady pressure caused by reducing the number of harmonics in the spectral NRBC is 3.45 Pa. This shows once more that, if the concept developed in chapter 4 is followed, reducing the number of harmonics, does not influence the flow solution.

In order to assess the increase in efficiency resulting from the reduction of the number of harmonics, GPTL is used on this test case. Figure 5.13 exhibits the percentage of the iteration loop represented by “Apply boundary conditions”, for 1D unsteady NRBC, for 2D steady NRBC and for spectral NRBC combined with the reduced and the complete set of harmonics. Here, GPTL is applied for 208 timesteps. The number under the pie

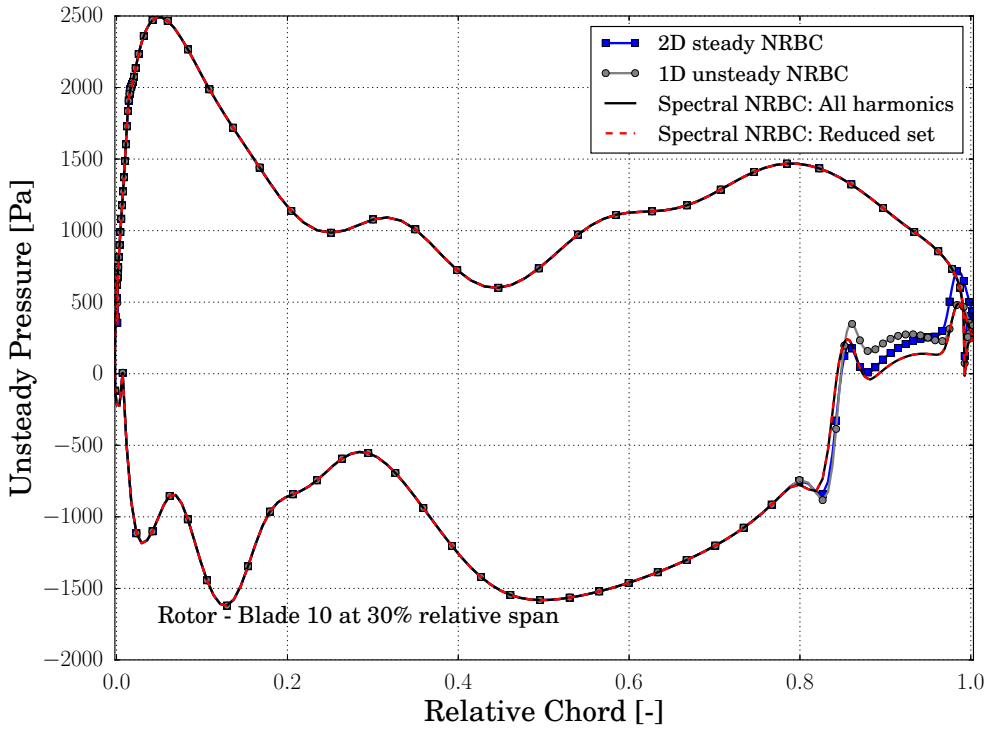

Figure 5.10: Comparison of the unsteady pressure distribution on the tenth blade of the rotor at 30% relative span for different NRBC, at the start of a period.

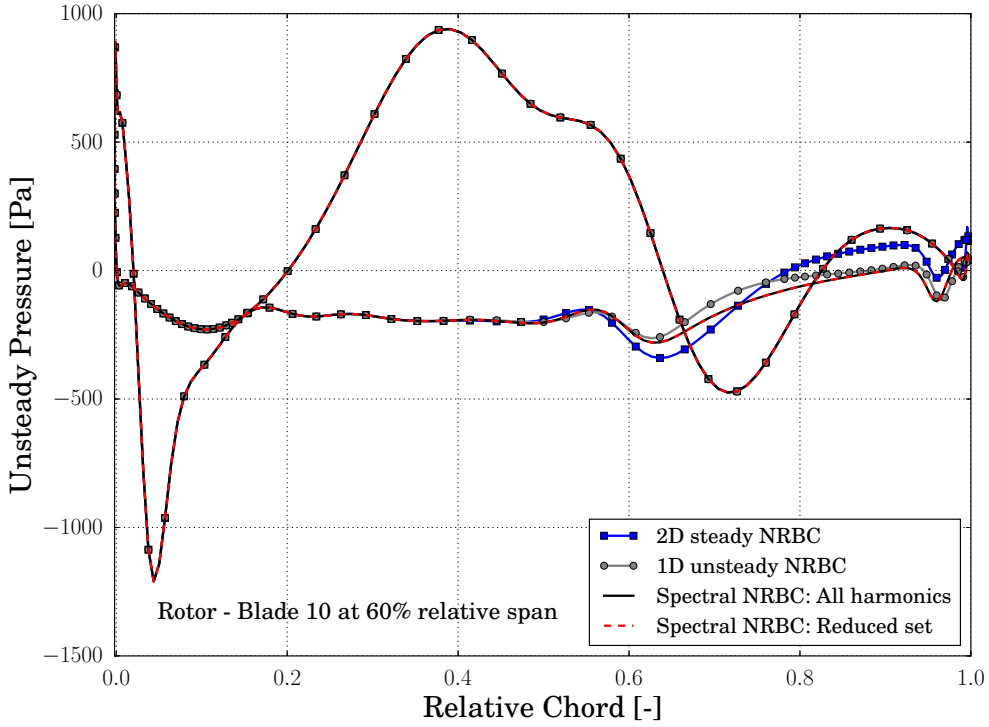

Figure 5.11: Comparison of the unsteady pressure distribution on the tenth blade of the rotor at 60% relative span for different NRBC, at the start of a period.

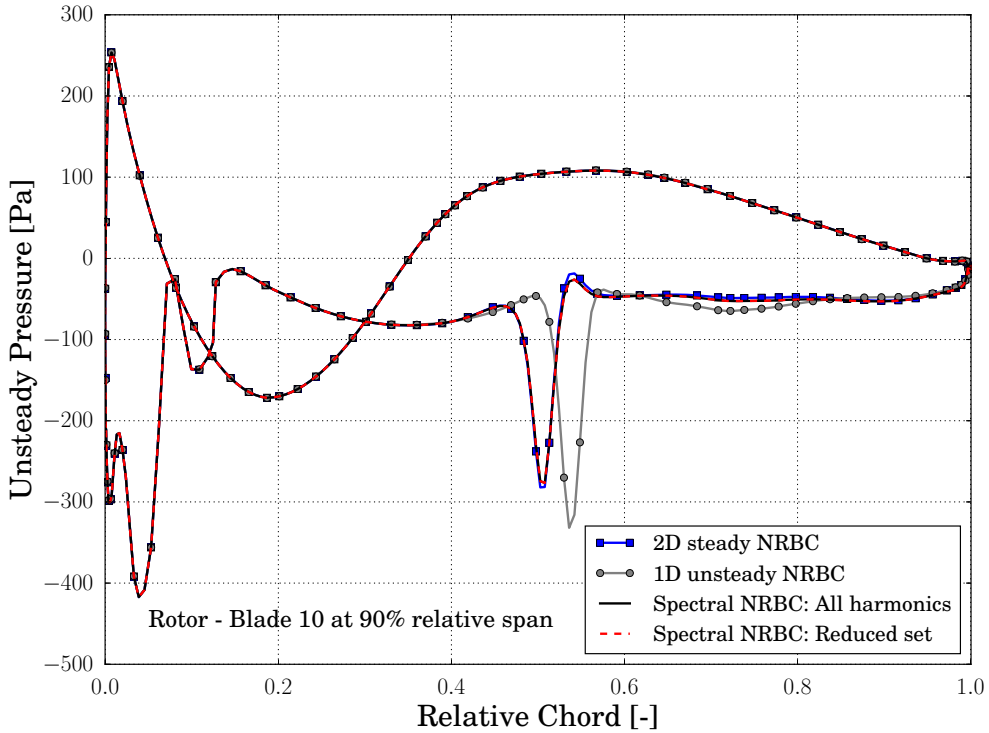

Figure 5.12: Comparison of the unsteady pressure distribution on the tenth blade of the rotor at 90% relative span for different NRBC, at the start of a period.

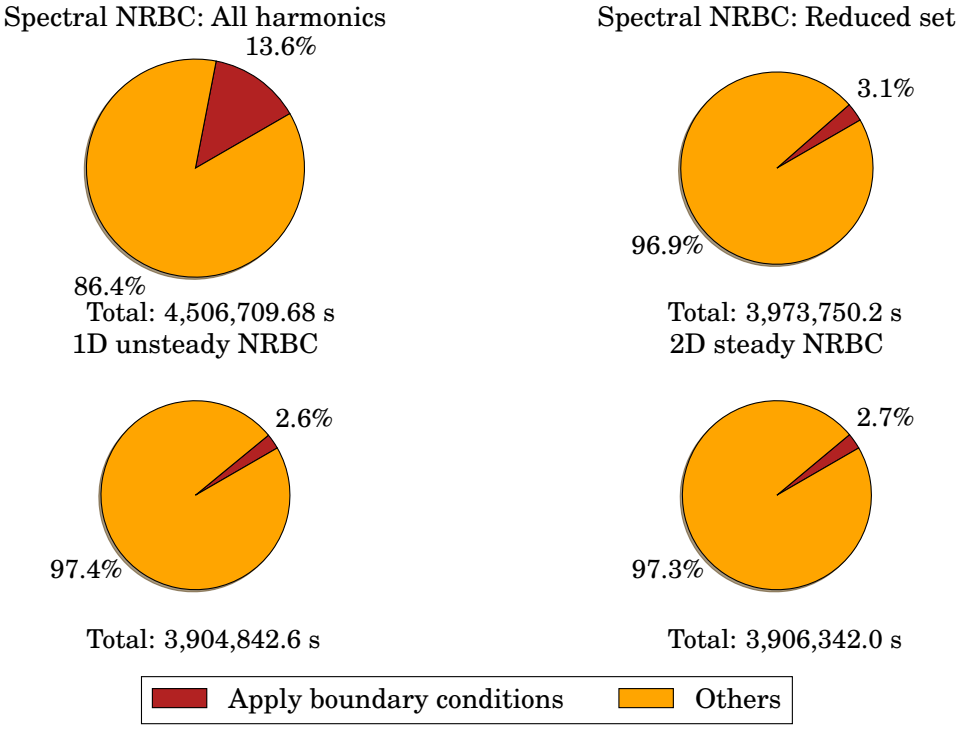

Figure 5.13: Comparison of the average percentage of the iteration loop represented by "Apply boundary conditions" in "All harmonics" and in "Reduced set".

charts, represent the time all processes spend in the iteration loop. The share of the application of the boundaries in an average iteration loop decreases from 13.6% to 3.1%. This corresponds to a decrease of 79.0% for the computational costs of the NRBC and 11.83% for the costs of the average iteration loop. Figure 5.13 shows that spectral NRBC using the reduced set of harmonics yield costs of the same order of magnitude as 1D unsteady NRBC and 2D steady NRBC. If the precision resulting from the reduced set is not satisfactory, the number of considered harmonics can be doubled or even tripled. The resulting computational costs would still be reasonable.

5.3 Verification Method for the Set of Harmonics

In chapter 4, relevant harmonics for the non-reflecting behavior of the two-dimensional NRBC are identified by analyzing the unsteady fluctuations at each harmonic individually. The problem with this method is that, for each harmonic, Fourier coefficients must be stored in each cell in the domain or at least at each boundary. This leads to high memory requirements, especially in three-dimensional cases.
A more efficient method is presented in this section. It utilizes analysis probes positioned at the boundaries. These probes record the unsteady history of one cell each. The latest period of the unsteady solution is Fourier decomposed.
For the turbine stage, 20 probes are defined at each boundary. The placement of the probes is shown in Figure 5.14. They are positioned at 5%, 25%, 50%, 75% and 95%

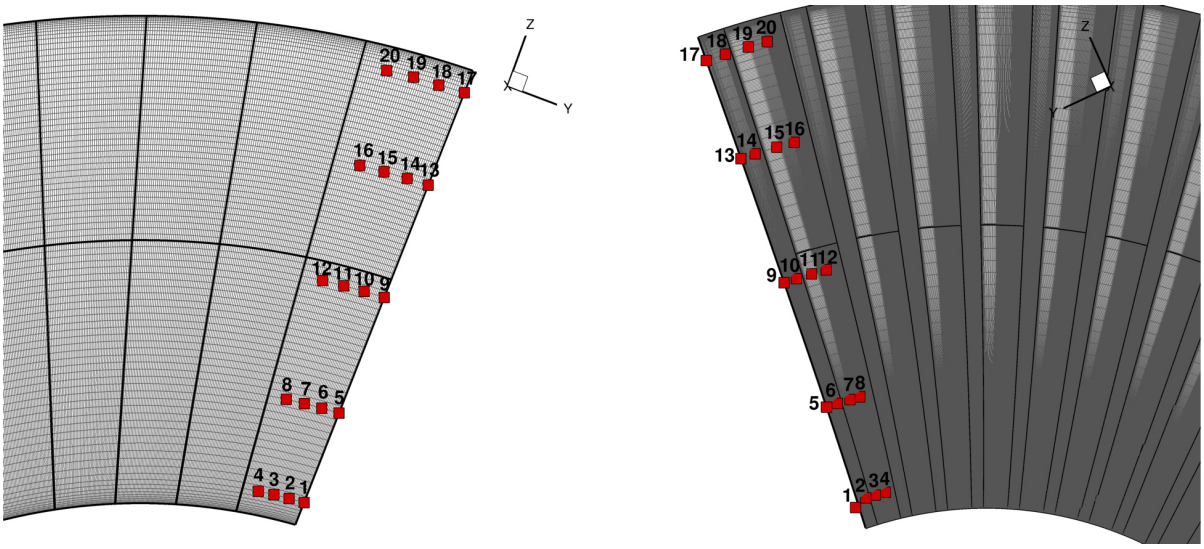

(a) Inlet boundary **(b)** Outlet boundary

Figure 5.14: Placement of the analysis probes in the steam turbine stage.

relative span. At each radial position, four probes are placed at 0%, 25%, 50% and 75% of the pitch of one blade passage. In this configuration, it is sufficient to place all probes in one blade passage. If indexing effects are present in the row adjacent to the boundary, the probes need to be placed in a way that covers the periodicity of the average flow. In the configuration simulated in chapter 4, the probes would need to be spread over four neighboring blade passages on the outlet boundary.

The flow recorded by the probe is Fourier transformed into the frequency domain. In the current section, only a few probes are analyzed with regard to the pressure as an example of the method.

In Figure 5.15, the amplitude of the temporal Fourier coefficients of the pressure in the probes 7, 10, 11 and 15 are plotted. The harmonics of the stator vane passing frequencies are colored in red and the harmonics of the rotor blade passing frequency are colored in green. As it is shown in Figure 5.2, there are no unsteady fluctuations at the inlet boundary. This is reflected in the Fourier decomposed solutions. Here, the first harmonics of the blade passing frequency of the rotor shows the largest amplitude, which is about 0.1 Pa. This is negligibly small. Therefore, NRBC are not necessary at the inlet boundary.

The amplitudes of the Fourier Coefficients of the pressure for the probes at the outlet are plotted in Figure 5.16. In contrast to the inlet boundary, the unsteady fluctuations at the outlet boundary are not negligible. The prediction that only the harmonics of the blade passing frequency of the rotor are relevant at the outlet is supported. Further, these plots display that with increasing relative span the amplitudes of the Fourier coefficients decrease. In probe 7, the amplitude of the ninth harmonic of the vane passing frequency is smaller than 1 Pa. The amplitudes decrease with increasing frequency. Therefore, using ten harmonics of the vane passing frequency of the stator is a good estimation to obtain a good non-reflecting behavior at the outlet.

This Method grants information about the relevance of each harmonic in the considered cell. This way, a comparison of the solution to a solution generated using a complete set of harmonics is not necessary to estimate the quality of the non-reflecting behavior at the

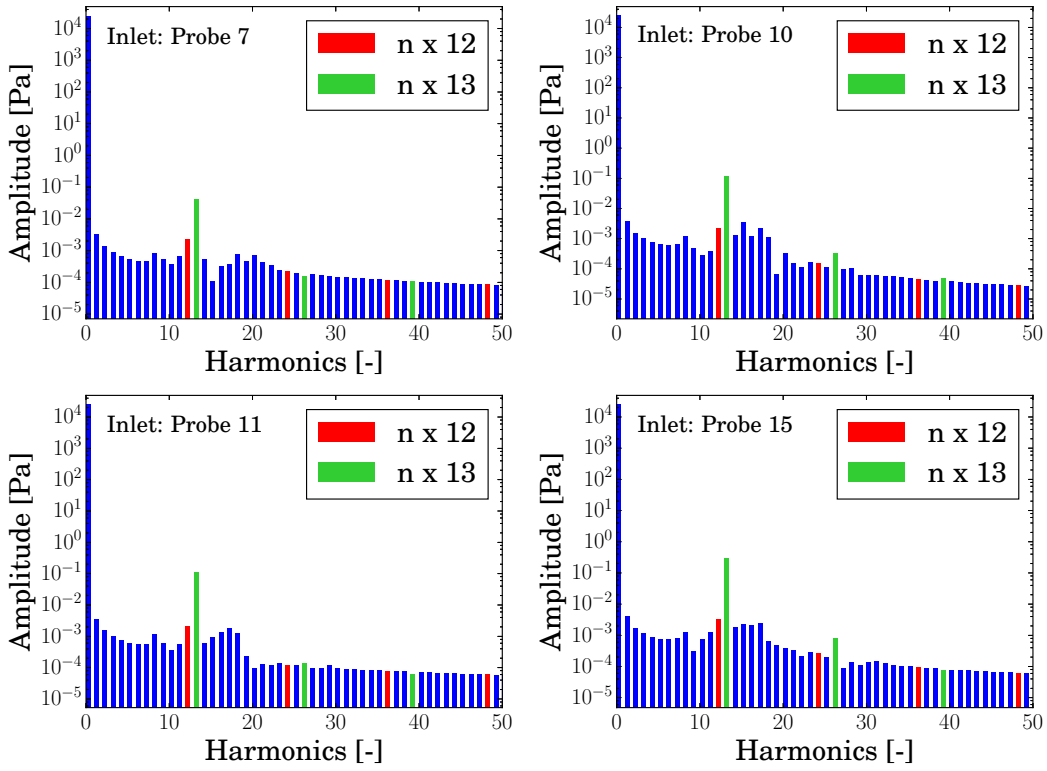

Figure 5.15: Fourier decomposed pressure for the probes a the inlet of the stator.

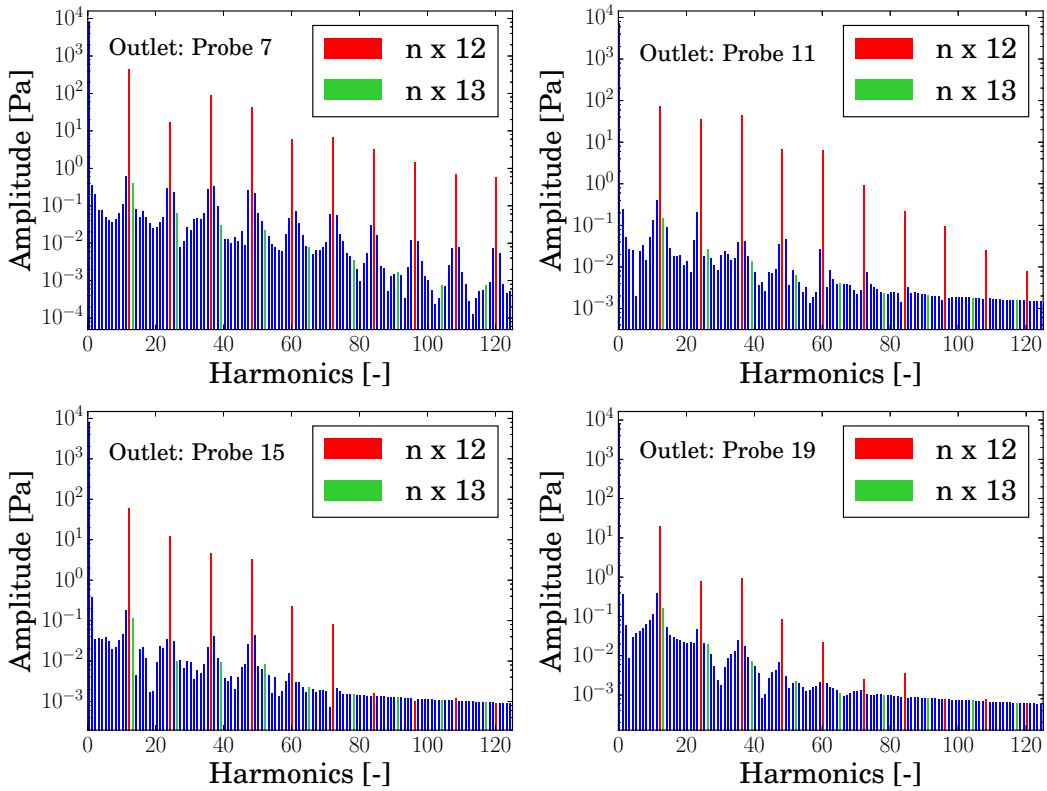

Figure 5.16: Fourier decomposed pressure for the probes a the outlet of the rotor.

boundary. If spurious reflections are observed in the solution, the Fourier decomposition indicates which harmonics are missing in the set of harmonics.
One drawback of this method is that it covers only a small portion of the solution at the boundary, therefore a good knowledge of the location of unsteady phenomena at the boundaries may be necessary, to not miss any spatially local unsteady effects. Here a fast steady simulation of the configuration, helps to identify where shocks and wakes impinge on the boundary. Such a steady simulation often needs to be performed anyways, to initialize the unsteady simulation. Another drawback of this method, is that it only provides information about already simulated configurations.

6 Conclusion

In this work, a concept to define reduced sets of harmonics for spectral NRBC was developed. In two test cases, reducing the number of considered harmonics following this concept lead to a significant decrease of computational costs, with no impact on the prediction quality of the solution.

For the development of the concept, 1.5 stages of the research compressor Rig250 were studied. A performance analysis on this test case was carried out. The results illustrated the need for a reduction of the costs of spectral NRBC. Also, the reduction of computational costs in relation to the number of harmonics included in the NRBC was quantified. Fundamental frequencies were defined for this configuration. These consisted of the base frequency, the vane and blade passing frequencies of the different rows, and the zeroth harmonic. Several simulations, demonstrated that ten harmonics of the fundamental frequencies suffice to achieve very good results. To further identify irrelevant harmonics, the unsteady pressure at each harmonic was analyzed individually. In general, the relevant harmonics for the NRBC were identified to be the harmonics of the vane and blade passing frequencies of rows with different rotation speed from that of the boundary. Furthermore, an indexing effect was observed in S_2. This induced a periodicity of the steady flow in S_2. This periodicity, manifested itself in R_2 as unsteady fluctuations at the third harmonic of the base frequency. This indexing frequency was identified to be irrelevant for the spectral NRBC, in the considered configuration. A set of harmonics composed of ten harmonics of BPF_2 and the zeroth harmonic was used for a final simulation of Rig250. The results of this setup matched perfectly with the results generated using a complete set of harmonics. The reduction from 308 harmonics to eleven harmonics lead to a reduction of 80% of the computational cost of the spectral NRBC. This setup was also simulated using 1D unsteady NRBC, 2D steady NRBC and approximate NRBC. The different NRBC yielded large differences in the unsteady pressure distribution on the blades, especially towards the outlet.
To verify the concept derived from the simulations of the Rig250, a steam turbine stage from the Durham University was chosen as second test case. This configuration is highly supersonic and comprises a complex system of shocks. Again, sets of eleven harmonics were defined at each boundary. At the inlet, the set comprised ten harmonics of the rotor blade passing frequency and the zeroth harmonic, at the outlet, it comprised ten harmonics of the stator vane passing frequency and the zeroth harmonic. Again, the results of this setup matched perfectly with results obtained using a complete set of harmonics. This test case was simulated using 1D unsteady NRBC, 2D steady NRBC and approximate NRBC. In this configuration, the approximate NRBC did not converge. The use of 1D unsteady NRBC resulted in difference in the steady and unsteady pressure distribution on the blades. The computational costs of spectral NRBC in combination with a reduced set of harmonics were in the same order of magnitude as the computational costs of 1D unsteady NRBC and 2D steady NRBC. Finally, a memory efficient method was presented, to assess the quality of a set of harmonics used in an unsteady simulation. This method is based on the temporal Fourier decomposition of probes at the boundaries.

To further decrease the costs of spectral NRBC, a similar concept can be developed for the reduction of circumferential wave numbers included in the spectral NRBC. This constitutes a more challenging task because the identification of relevant wave numbers is less straightforward. Additionally, the increase in efficiency is expected to be lower than for the concept presented in the current work.
The topic of slow convergence was addressed in this work. The empirical method presented to improve the convergence of the mean state has to be investigated in more detail. In order to exhaust its full potential, its stability needs to be tested for other cases.
An important step for spectral NRBC to become state of the art in industrial applications is to automatize the definition of an optimal set of harmonics. One possibility is to identify relevant harmonics using a circumferential flow decomposition of a steady solution, but this is very complicated for complex multistage configurations. However, it would yield optimal sets of harmonics adjusted to each case individually.

Bibliography

[1] Ashcroft, G. ; Frey, C. ; Kersken, H.-P. ; Kügeler, E. ; Wolfrum, N.: On the Simulation of Unsteady Turbulence and Transition Effects in a Multistage Low Pressure Turbine, Part I: Verification and Validation. In: *Proceedings of ASME Turbo Expo 2018*, 2018

[2] Ashcroft, G. ; Schulz, J.: Numerical Modelling of Wake-Jet Interaction with Application to Active Noise Control in Turbomachinery. In: *Americcan Institute of aeronautics and Astronautics* (2004)

[3] Becker, K. ; Heitkamp, K. ; Kügeler, E.: Recent Progress In A Hybrid-Grid CFD Solver For Turbomachinery Flows. In: *V European Conference on Computational Fluid Dynamics ECCOMAS CFD 2010*, 2010

[4] Burton, Z.: *Analysis of low pressure steam turbine diffuser and exhaust hood systems*, Durham University, Diss., 2014

[5] Chassaing, J. ; Gerolymos, G.: Time-domain implementation of nonreflecting boundary conditions for the nonlinear euler equaitons. In: *Applied mathematical modelling* Bd. 31, 2007, S. 2172–2188

[6] Energy Technology, Stockholm S. KTH Royal Institute of Technology o. KTH Royal Institute of Technology T. KTH Royal Institute of Technology: *3D Steam Turbine Flutter Test Case.* – https://www.kth.se/en/itm/inst/energiteknik/forskning/kraft-varme/ekv-researchgroups/turbomachinery-group/aeromech-test-cases/3d-steam-turbine-flutter-test-case-1.706654, accessed on 06-09-2018

[7] Engquist, B. ; Majda, A.: Absorbing Boundary Conditions for Numerical Simulation of Waves. In: *Proceedings of the National Academy of Sciences* 31 (1977), May, Nr. 5, S. 629–651

[8] Frey, C. ; Kersken, H.-P.: On The Regularisation of Non-Reflecting Boundary Conditions near Acoustic Resonance. In: *ECCOMAS Congress* (2016)

[9] Giles, M.: UNSFLO: A Numerical Method for Unsteady Inviscid Flow in Turbomachinery. In: *Gas Turbine Laboratory Report GTL 205*, Massachusetts Institute of Technology - dept. of Aero. and Astro., 1991 (GTL report)

[10] Giles, M. B.: Non-reflecting Boundary Conditions for the Euler Equation. In: *tech. rep.*, Massachusetts Institute of Technology - dept. of Aero. and Astro., 1988. – CFDL Report 88-1

[11] Giles, M. B.: Non-Reflecting Boundary Conditions For Euler Equation Calculation. In: *AIAA Journal* 28 (1990), Nr. 12, S. 2050–2058

[12] Hagstrom, T. ; Engquist, Bjorn (Hrsg.) ; Kriegsmann, Gregory A. (Hrsg.): *On High-Order Radiation Boundary Conditions*. New York, NY : Springer New York, 1997. – 1–21 S.

[13] He, L.: Fourier methods for Turbomachinery Applications. In: *Progress in Aerospace Sciences* 46 (2010), Nov, Nr. 8, S. 329–341

[14] Henninger, S. ; Jeschke, P. ; Ashcroft, G. ; Kügeler, E.: Time-Domain Implementation of Higher-Order Non-Reflecting Boundary Conditions for Turbomachinery Applications. In: *Proceedings of the ASME Turbo Expo 2015* Bd. 2. New York, NY, Jun 2015, S. V02BT39A016

[15] Higdon, Robert L.: Initial-Boundary Value Problems for Linear Hyperbolic Systems. In: *SIAM Review* 28 (1986), Nr. 2, 177–217. http://www.jstor.org/stable/2030466. – ISSN 00361445

[16] Hirsch, C.: Chapter 9 - Time Integration Methods for Space-discretized Equations. In: *Numerical Computation of Internal and External Flows (Second Edition)*. Second Edition. Oxford : Butterworth-Heinemann, 2007. – ISBN 978–0–7506–6594–0, S. 413 – 489

[17] Junge, L.: *Verallgemeinerung des Harmonic Balance Verfarhens im Strömungslöser TRACE auf Basis fastperiodischer Fouriertransformationen*, RWTH Aachen University, Diplomarbeit, 2016

[18] Keiner, J. ; Kunis, S. ; Potts, D.: Using NFFT 3—A Software Library for Various Nonequispaced Fast Fourier Transforms. In: *ACM Trans. Math. Softw.* 36 (2009), Aug, Nr. 4, S. 19:1–19:30. – ISSN 0098–3500

[19] Kersken, H.-P. ; Frey, C. ; Ashcroft, G. ; Wolfrum, N. ; Korte, D.: Nonreflecting Boundary Conditions For Aeroelastic Analysis In Time and Frequency Domain 3D RANS Solvers. In: *ASME Turbo Expo 2014*, 2014, S. GT2014–25499

[20] Kreiss, Heinz-Otto: Initial Boundary Value Problems for Hyperbolic Systems. In: *Communications on Pure and Applied Mathematics* 23 (1970), S. 277–298

[21] Petrie-Repar, P. ; Makhnov, V. ; Shabrov, N. ; Smirnov, E. ; Galaev, S. ; K.Eliseev: Advanced flutter analysis of long shrouded steam turbine blade. In: *Proccedings of the ASME Turbo Expo 2014*, 2014

[22] Qi, D. ; Petrie-Repar, P. ; Gezork, T. ; Sun, T.: Establishment of an Open 3D Steam Turbine Flutter Test Case. In: *Proceedings of 12th European Conference on Turbomachinery Fluid Dynamics & Thermodynamics*, 2017

[23] Robens, S. ; Frey, C. ; Jeschke, P. ; Kügeler, E. ; Bosco, A. ; Breuer, T.: Adaptation of Giles Non-Local Non-Reflecting Boundary Conditions for a Cell-Centered Solver for Turbomachinery Applications. In: *ASME Turbo Expo 2013*, 2013

[24] Roe, P. L.: Approximate Riemann Solvers, Parameter Vectors, and Difference Schemes. In: *J. COMP. PHYS* 43 (1981), S. 357–372

[25] Rosinski, J.: *GPTL - General Purpose Timing Library.* https://jmrosinski.github.io/GPTL/ (16.07.2018),

[26] Saxer, A. P. ; Giles, M. B.: Quasi-Three-Dimensional Nonreflecting Boundary Conditions for Euler Equation Calculation. In: *Journal of Propulsion and Power* 9 (1993), Nr. 2, S. 263–271

[27] Schlüss, D. ; Frey, C.: Time Domain Flutter Simulations of a Steam Turbine Stage Using Spectral 2D Non-Reflecting Boundary Conditions. In: *Proceedings of the 15th International Symposium on Unsteady Aerodynamics, Aeroacoustics & Aeroelasticity of Turbomachines, ISUAAT15*, 2018

[28] Schlüss, D. ; Frey, C. ; Ashcroft, G.: Consistent non-refleflecting boundary conditions for both steady and unsteady flow simulations in turbomachinery applictations. In: *VII European Congress on Computational Methods in Applied Sciences and Engineering (ECCOMAS Congress 2016)*, 2016

[29] Schönweitz, D. ; Goinis, G. ; Voges, M. ; Enders, G. ; Johann, E.: Experimental and Numerical Examinations of a Transonic Compressor-Stage With Casing Treatment. In: *ASME Turbo Expo 2013*, 2013

[30] Sutherland, W.: The viscosity of gases and molecular force. In: *Philosophical Magazine* 5 (1983), Nr. 36, S. 507–531

[31] Tu, J. ; Yeoh, G.H. ; Liu, C.: *Computational Fluid Dynamics: A Practical Approach.* Elsevier Science, 2018 https://books.google.de/books?id=cScsDwAAQBAJ. – ISBN 9780081012444

[32] van Albada, G. D. ; van Leer, B. ; Roberts, W. W. Jr.: A comparative study of computational methods in cosmic gas dynamics. In: *Astronomy and Astrophysics* 108 (1982), Nr. 1, S. 76–84

[33] van Leer, B.: Towards the ultimate conservative difference scheme. V. A second-order sequel to Godunov's method. In: *Journal of Computational Physics* 32 (1979), Nr. 1, S. 101 – 136. – ISSN 0021–9991

[34] Weber, A. ; Sauer, M.: PyMesh - template documentation / German Aerospace Center (DLR), Institute for Propulsion Technology, Linder Hoehe, Cologne. 2016 (DLR-IB-AT-KP-2016-34). – Technical report

[35] Wilcox, D.: Reassessment of the scale-determining equation for advanced turbulence models. In: *AIAA Journal* 26 (1988), Nov, Nr. 11, S. 1299–1310

[36] Yang, H. ; Nürnberger, D. ; Weber, A.: A Conservative Zonal Approach with Application to Unsteady Turbomachinery Flows. In: *DGLR Jahrestagung*, 2002